
Development of a 61-Pixel Camera for the IceAct Imaging Air Cherenkov Telescope

von

Jan Paul Koschinsky

Masterarbeit in Physik

vorgelegt der
Fakultät für Mathematik, Informatik und Naturwissenschaften
der
Rheinisch-Westfälischen Technischen Hochschule Aachen

im September 2017

angefertigt am

III. Physikalischen Institut B

Erstgutachter

Prof. Dr. Christopher Wiebusch
III. Physikalisches Institut B
RWTH Aachen

Zweitgutachter

Prof. Dr. Thomas Bretz
III. Physikalisches Institut A
RWTH Aachen

Betreuer

Dr. Jan Auffenberg
III. Physikalisches Institut B
RWTH Aachen

Contents

1	Introduction	1
2	The IceCube Neutrino Observatory	3
2.1	Cosmic Rays	3
2.2	Neutrinos and Neutrino Astronomy	5
2.3	The IceCube Array	7
2.4	The Surface Detector IceTop	9
2.5	The IceCube Extension Gen2	9
3	The IceAct Telescope	13
3.1	Cherenkov Light	13
3.1.1	Imaging Air Cherenkov Telescopes	14
3.2	Why IceAct?	16
3.3	Design of the IceAct Telescope	18
3.3.1	The Camera	20
3.3.1.1	Silicon Photomultipliers	22
4	First Night Sky Measurements with the new TARGET 7 DAQ	29
4.1	TARGET 7 ASIC and TARGET 7 Module	29
4.1.1	Software for Operation of the TARGET 7 Module	33
4.2	Erlangen Setup and Measurement Procedure	34
4.3	Event View and First Analysis	36
5	Development of Light-Collecting Cones for the IceAct Camera	41
5.1	Requirements on the Light-Collecting Cones	41
5.2	Theory on Winston Cones	43
5.3	Design of Investigated Cone Models	45

5.3.1	The Final Hex-to-Square Cone	50
5.4	Zemax Simulations for the Cone Development	52
5.4.1	Simulation of Efficiency of Cone and SiPM in IceAct	54
5.4.1.1	Simulation Setup and Procedure	54
5.4.1.2	Analysis of Cone Efficiencies	57
5.4.2	Simulation of the SiPM Illumination	63
5.4.3	Simulation of the Angular Acceptance	65
5.4.4	Simulation for Comparison with Measurement	67
5.5	Cone Measurement for Verification of Simulation and Manufacturing Optimization	70
5.5.1	Measurement Setup and Procedure	70
5.5.1.1	Adjustment of Laser Beam Diameter	73
5.5.2	Analysis of Different Cone Models	75
5.6	Measurement of PMMA Absorption	80
5.7	Low Temperature Test of Cone-Coupling Glue	83
6	Summary and Outlook	85
7	Appendix	87
	Bibliography	99
8	Acknowledgements Danksagungen	101

1. Introduction

The IceCube Neutrino Observatory located at the South Pole investigates high energetic astrophysical neutrinos. One main objective is the measurement of the flux of these neutrinos and the identification of their sources, which is of immense astrophysical importance, as these sources are also believed to be the sources of the high energy cosmic rays. With IceTop, a surface air shower detector above the IceCube in-ice array, properties like the composition of high energy cosmic rays can also be investigated. Hereby IceTop detects air showers generated by cosmic rays penetrating the atmosphere. Furthermore these atmospheric events can be vetoed, as they are the main and by far dominating background for the measurement of astrophysical neutrinos.

Part of the Gen2 extension of IceCube is a larger surface air shower detector. One possible veto technology are compact imaging air Cherenkov telescopes, IceAct, featuring a lower energy threshold compared to surface particle detectors like used in IceTop. The IceAct telescope design is adapted from the FAMOUS fluorescence telescope which achieves a large field of view. The light-collecting system of IceAct comprises a Fresnel lens allowing for an enclosed optical system protecting the camera from the harsh environment. The camera is based on light-collecting cones and SiPMs allowing for a high duty cycle.

In this thesis the development of a new 61-pixel camera is presented that is intended to replace the 7-pixel camera, currently operating with an IceAct demonstrator at the South Pole. First measurements with the TARGET 7 based data acquisition and the 61-pixel camera are presented. The focus of this thesis is the development of new light-collecting cones lowering the energy threshold of IceAct due to an improved photon detection efficiency.

2. The IceCube Neutrino Observatory

Astroparticle physics evolved into a large and promising field of research, connecting particle physics with astrophysics and cosmology. As a result large observatories are built to open new windows to the universe. In the beginning of this thesis an introduction to the fields of research of the IceCube Neutrino Observatory (IceCube) and the observatory design will be given. First, cosmic rays and neutrino astronomy will be described, as IceCube focusses on the study of high energetic astrophysical neutrinos. Thereafter, an overview of the observatory design and its investigated future extensions will be given. The IceAct telescope is part of the currently discussed future extensions and will be introduced in chapter 3.

2.1 Cosmic Rays

In 1912 Victor Franz Hess performed balloon flights, equipped with electroscopes, and discovered a rise of the ionization rate with growing altitude. Therefore he assumed the existence of high energetic ionizing particles that originate from outer space; so-called cosmic rays [1]. More than one century later the chemical composition, the search for the sources as well as the acceleration and propagation mechanisms of these cosmic rays are still unresolved. To detect these very high energetic atomic nuclei increasingly large experimental challenges are met.

Figure 2.1 depicts the differential energy spectrum of cosmic rays on a double-logarithmic scale multiplied by $E^{2.6}$ to highlight the three denoted features in the spectrum. On the y-axis the flux is given in units of particles per energy [GeV], area [m^2], time [s] and solid angle [sr]. The data from various experiments is combined [2]. Direct measurements with satellites are feasible up to an energy of about 1 PeV, as there the flux decreased to about one particle per square meter and year. Above this energy ground based indirect measurements are carried out measuring properties of secondary particles which are produced by the high energetic primary particle in extensive air showers within the Earth's atmosphere [3].

Extensive air showers develop from interactions of the primaries with nuclei in the atmosphere and the following interactions or decays of secondary particles. During the first interactions mostly pions are generated, which decay into photons if they are uncharged or muons and neutrinos if they are charged. Photons then induce an electromagnetic component of the shower, whereas muons contribute to the muonic component. In the center of the shower a hadronic component develops from other

nuclear interactions [4]. Though challenging, the separation of the electromagnetic and the muonic component on the ground is important for today's experiments to draw inferences about the primary cosmic ray. The composition of the primary can be determined by the number and the lateral distribution of the muons in the shower while the muon density on the ground is an estimator for the primary energy independent of the primary mass [3]. Especially the produced neutrinos are of interest for IceCube, as these *atmospheric neutrinos* are a major background in the search for *astrophysical neutrinos*.

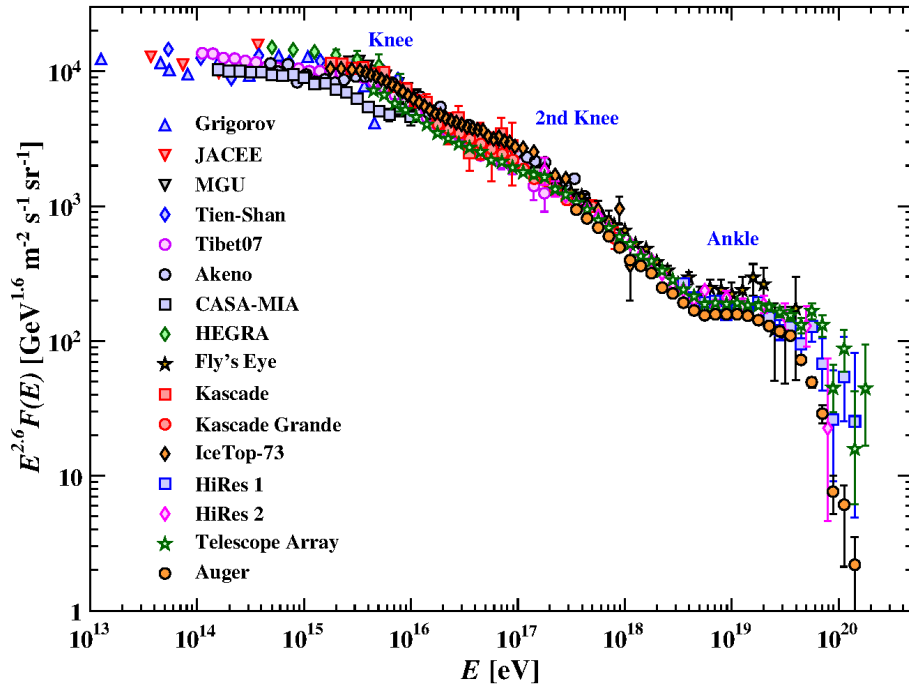


Figure 2.1: Differential energy spectrum of cosmic rays. Plotted are combined measurements from air shower detectors. For a better visibility of the three denoted features, the spectrum is multiplied by $E^{2.6}$. Taken from [2].

The cosmic ray spectrum ranges from energies of a few MeV up to 10^{20} eV and follows a broken power law, suggesting non-thermal acceleration processes [3]:

$$\frac{dN}{dE} \propto E^\gamma . \quad (2.1)$$

The so-called *knee* marks a softening of the spectrum in the PeV regime where the spectral index γ changes from $\gamma \approx -2.7$ to $\gamma \approx -3.1$ for higher energies. A further softening around $10^{17.5}$ eV called the *second knee* is followed by the *ankle*, a hardening back to $\gamma \approx -2.7$ at $10^{18.5}$ eV. The spectrum finally cuts off at $10^{19.5}$ eV [3]. These features in the detected spectrum of cosmic rays are explained in different models, but none of them is verified yet. For instance the spectrum is modelled by three different populations superimposing each other. Common explanations are often based on the magnetic rigidity [5]:

$$R = \frac{Pc}{Ze} , \quad (2.2)$$

where P denotes the total momentum of the cosmic ray nuclei and Z its atomic number, i.e. its electrical charge in units of the elementary charge e . Particles of the same magnetic rigidity move along the same trajectories when interacting with a magnetic field. At high energies only the electrical charge and correspondingly the mass of the nuclei have a significant influence on the trajectory. Therewith the *knee* is explained as the extinction of a light galactic population, because the acceleration mechanisms of galactic sources, which are believed to be supernova remnants, might not be able to transmit more energy into the cosmic rays or the cosmic rays are not contained in the galactic magnetic field anymore. As ultra-heavy elements are contained in the galactic magnetic field for even higher energies because of their smaller rigidity, their extinction possibly causes the *second knee*. Furthermore the *ankle* is believed to be the onset of an extragalactic population, which has a less intense but harder spectrum. Finally the cutoff at highest energies might be the consequence of the sources maximum acceleration capability or energy losses during the propagation, namely the GZK-cutoff, which describes the interaction of cosmic rays with photons from the cosmic microwave background [3].

The GZK-cutoff is driven by the delta resonance, $p + \gamma \rightarrow \Delta^+ \rightarrow p + \pi^0$ or $n + \pi^+$, which creates high energetic neutrinos from charged pion decays. Astrophysical neutrinos might also originate from interactions at cosmic ray sources like in gamma ray bursts, active galactic nuclei or stellar objects [6]. As the investigation of these neutrinos is a primary goal of IceCube, the next section deals with them.

2.2 Neutrinos and Neutrino Astronomy

In 1930 Wolfgang Ernst Pauli postulated the existence of the neutrino, since the continuous β -decay energy spectrum produced by electrons indicated a three-body decay [7]. Neutrinos are extremely lightweight and electrically uncharged leptonic particles. As they only interact via the weak force, neutrinos can travel large distances without interacting or being deflected. At the same time it is challenging to detect them such that large detectors like IceCube are needed. Nevertheless free neutrinos were first detected in 1953 by Cowan and Reines via delayed coincidences from inverse β -decays of electron antineutrinos generated in a nuclear power plant [8]. They confirmed their measurement in 1956 with an improved experiment [9] and were awarded the Nobel Price for physics in 1995.

With the growing interest in astroparticle physics also the importance of astrophysical neutrinos increased, as they are an unique messenger of the highest energy processes in the universe. Neutrinos might be generated in hadronic interactions when accelerated cosmic rays hit nuclei, gasses or background photons from radiation fields inside of or very close to the cosmic ray sources [10]. Hence they provide information on cosmic ray sources. Figure 2.2 shows a sketched comparison of the propagation of cosmic rays, gamma rays and neutrinos through the universe. As cosmic rays are charged nuclei, they are deflected by magnetic fields, such that the reconstruction of their arrival direction does not directly point back to their source. Whereas gamma rays do point back to their sources, while they can be absorbed during propagation. In contrast neutrinos have both advantages of neither being deflected nor absorbed. Moreover neutrinos have an advantage over gamma rays,

because high energetic neutrinos can only be created during the acceleration of hadrons, thus in cosmic ray sources [11].

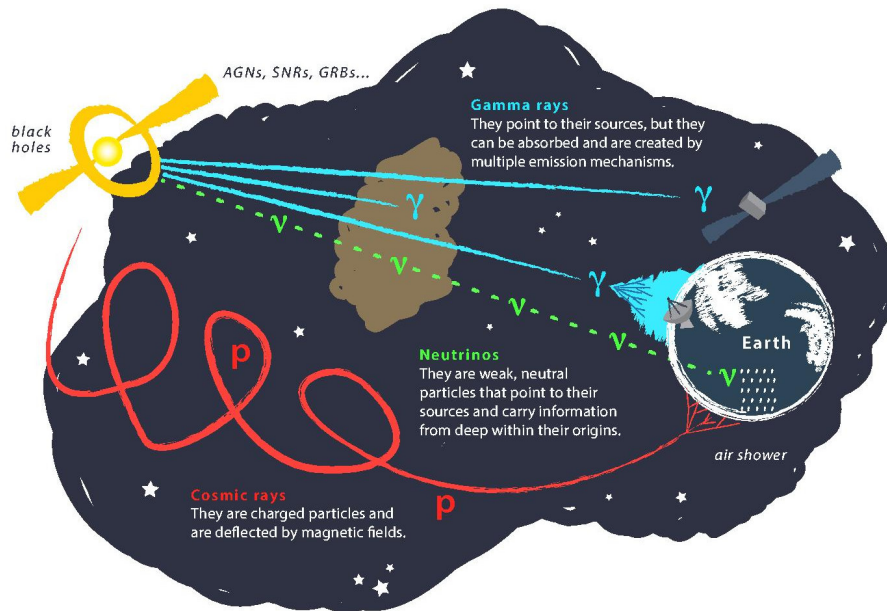


Figure 2.2: Sketched view of cosmological particle propagation. The comparison of cosmic rays, gamma rays and neutrinos reveals that only the latter are neither deflected nor absorbed on their way from astrophysical sources to the Earth. Taken from [12].

The flux contributions of different sources to the differential energy spectrum of neutrinos on Earth is plotted in figure 2.3. The fluxes are either known from measurements as e.g. the reactor antineutrinos, which were first detected by Cowan and Reines, or predicted from theories as e.g. the so-called cosmogenic neutrinos, which originate from the GZK-cutoff as described in the previous section [11]. IceCube has the capability of detecting neutrinos with energies above about 0.1 TeV [13] and thereby cosmogenic neutrinos and neutrinos from extragalactic sources like supernova remnants, gamma ray bursts and active galactic nuclei (named " ν from AGN" in figure 2.3). As the flux of atmospheric neutrinos dominates for low energies, only above 100 TeV one can suppose that the neutrino had an extraterrestrial origin [13]. Furthermore neutrinos are not detected directly but via secondary particles produced in interactions. Commonly detectors make use of Cherenkov light (see section 3.1) from charged secondary particles like muons to deduce the arrival direction and energy of the primary neutrino. This is also the detection technique of IceCube and of the IceAct telescope. Since air showers induced by cosmic rays produce muons, too, it is challenging to distinguish rare astrophysical neutrino events from this dominating background. Muons cannot traverse through the entire Earth, so selecting events coming from inside the Earth reduces the atmospheric muon background, but more sophisticated event selection strategies are used to be able to perform full-sky observations. When multiple detectors are operated in hybrid mode, one can veto against background events, which is one objective of IceCube's surface detector IceTop and of the IceAct telescope.

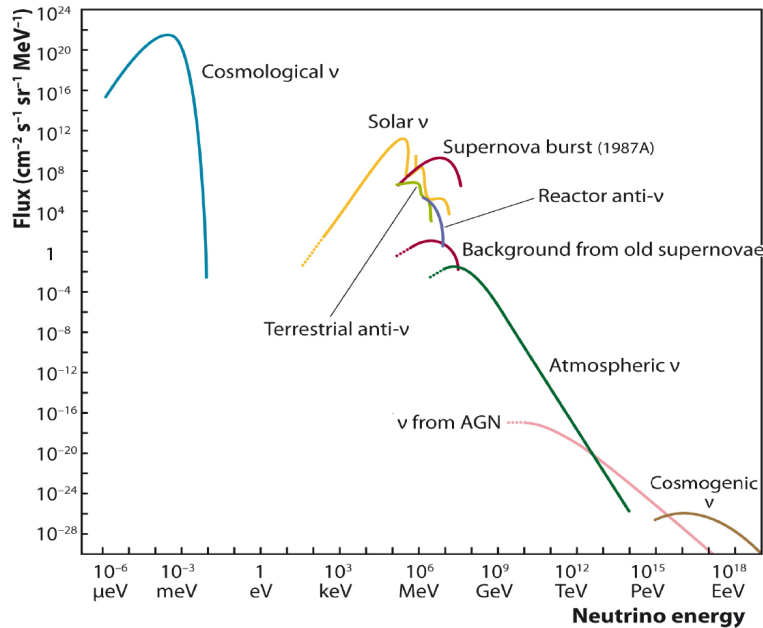


Figure 2.3: Differential energy spectrum of neutrinos on Earth. Plotted are expected and measured neutrino fluxes of different origins. Taken from [11].

In 2013 a breakthrough in neutrino astronomy was achieved by the IceCube collaboration by publishing the first evidence for the existence of high energetic extraterrestrial neutrinos [10]. This first full-sky search comprising two years of data resulted in 28 neutrino candidates with energies between 30 TeV and 1.2 PeV. Though a terrestrial origin of these neutrinos could be excluded with a $4\text{-}\sigma$ significance, the low statistics did not allow for finding clustering in time nor space [10]. As of today no neutrino point sources were spotted. So the main objective of IceCube is to identify and characterize astrophysical neutrino sources, and accordingly cosmic ray sources, by advancing statistics and detector extensions [14].

2.3 The IceCube Array

IceCube is located near the Amundsen-Scott South Pole Station about 3000 m above sea-level. Currently it is the largest neutrino detector built on Earth. Due to its vast abundance amount and excellent optical properties, the glacial ice in Antarctica is particularly suited as a medium for Cherenkov light transmission of secondary particles, produced by neutrinos. The deep in-ice detector of IceCube, the IceCube Array, instruments 1 km^3 of ice in order to gain reasonable statistics despite the low interaction cross section and low flux of high energetic neutrinos. Within this ice cube a 3D image of the deposited energy is recorded in the manner of a tracking calorimeter [14]. A complete view of the IceCube facilities is shown in Figure 2.4 (a).

Since the completion in 2011, the IceCube Array consists of 86 vertical strings, which were melted 2450 m deep into the glacial ice, reaching almost the bedrock. The strings are arranged on a triangular grid with a hexagonal footprint and a horizontal spacing of 125 m. In total 5160 Digital Optical Modules (DOMs) are coupled to

the strings to detect Cherenkov light emitted by charged particles traversing the ice in the detector volume. 60 DOMs are deployed along each string with a vertical spacing of 17 m in depths between 1450 m and 2450 m [14]. The upper ice region of about 1.5 km extent is not deployed, as there the scattering length is small due to poor optical properties [15]. A beneficial side effect is the reduced background of extensive air showers in these depths. In the center of the IceCube Array, there is an infill array called DeepCore, which offers a lower energy threshold of 10 GeV compared to the 100 GeV threshold of the IceCube Array. That is due to a reduced string and DOM spacing and more efficient PMTs included [14].

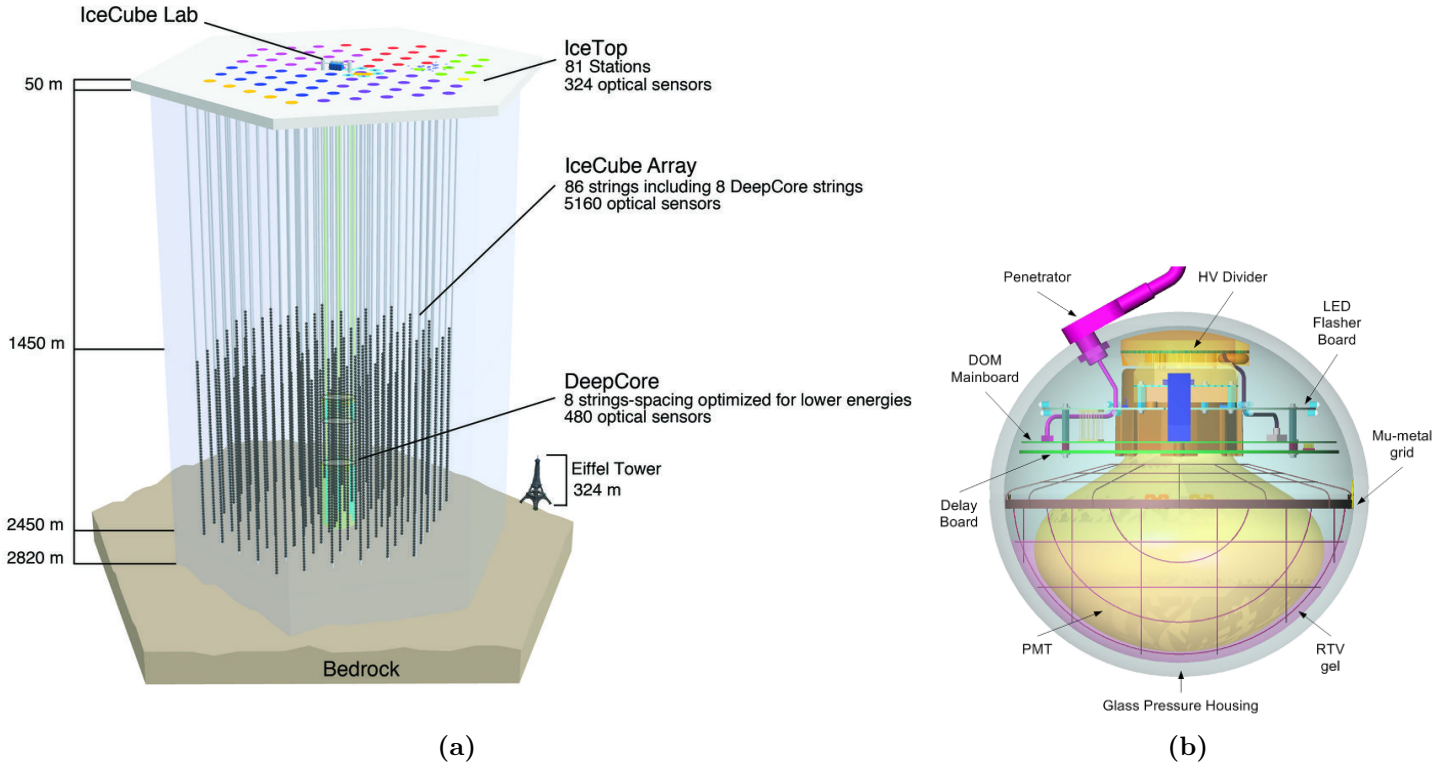


Figure 2.4: Sketches of IceCube and a Digital Optical Module. (a) The left side shows a sketch of the IceCube facilities including the 1 km^3 large IceCube Array and the Eiffel Tower for size comparison. Taken from [16]. (b) The right is a cross section of a Digital Optical Module. 5160 DOMs are operated in the IceCube Array to detect Cherenkov light. Taken from [17].

A cross section of a DOM is given in figure 2.4 (b). Each DOM consists of a downward-facing 10" photomultiplier tube (PMT) coupled to a glass pressure sphere via an optical gel. Moreover electronic boards are installed, which supply the PMT with the required high voltage and trigger on the raw waveforms, before sending digitized and timestamped waveforms via the strings to the central control facility, namely the IceCube Lab in figure 2.4 (a). Furthermore a LED flasher board allows for the calibration of the PMTs and the surrounding ice [14].

An event in the IceCube Array provides the timing information of the PMTs, which enables for reconstructing the arrival direction of the primary particle, and the depos-

ited charge in the PMTs, which is related to the intensity of the Cherenkov radiation and is an estimator for the energy of the primary particle. Beyond the primary objective of IceCube, finding and characterizing astrophysical neutrino point sources, other goals are new physics beyond the Standard Model like neutrino oscillations, the detection of galactic supernova explosions, the search for dark matter and the detection of cosmic rays. Where the latter utilizes a hybrid operation of the IceCube Array as a muon detector and IceTop as an air shower detector [18]. The hybrid mode enables for composition measurements, as lighter cosmic rays produce less muons in an air shower than heavy ones, such that the IceCube Array detects less muons in such events [5].

2.4 The Surface Detector IceTop

Figure 2.4 (a) in section 2.3 includes a schematic view of the 1 km² large IceTop surface detector, which detects the footprint of extensive air showers. IceTop, located in about 2835 m above sea level, consists of 81 stations covering the surface above the deep in-ice IceCube Array. Each station consists of two frozen water Cherenkov tanks of 182 cm inner diameter and 90 cm water level. Each tank is situated under the snow surface and operates two standard IceCube Array DOMs [19].

The energy resolution of IceTop amounts to about 25% for 2 PeV primary energy, improving for higher primary particle energies [14]. IceTop is sensitive to air showers from energies of about 300 TeV up to a few EeV, whereas the infill array in the center of IceTop, equal to DeepCore in the IceAct Array, has a lower energy threshold of 100 TeV. Consequently IceTop covers the energy region of the knee and the expected transition region from galactic to extragalactic sources of cosmic rays, introduced in section 2.1. The latter is considered to be accompanied by a change in the chemical composition, which can be deduced from the muonic fraction via the hybrid detection with the IceCube Array and IceTop, as IceTop mainly measures the electromagnetic component of the shower, while the IceCube Array detects muons with energies above about 500 GeV. Other objectives of IceTop are the detection of PeV gamma rays and short-lived events like radiation from solar flares. Equal to IceAct (see chapter 3) IceTop can be used as timing and direction calibration tool for the IceCube Array and provide a partial veto for downward-going neutrinos [19]. The pros and cons of IceAct over IceTop are discussed in section 3.2.

2.5 The IceCube Extension Gen2

IceCube Gen2 is the planned extension and next generation of the IceCube Neutrino Observatory, which is designed to extend the capabilities of IceCube in various fields of research. Figure 2.5 shows the baseline design of IceCube Gen2 comprising several new in-ice and surface detectors. The current IceCube Array (denoted IceCube-86 in figure 2.5) and IceTop are the orange regions in the center.

Beginning with the in-ice detectors, the Main Array is a planned detector of IceCube Gen2 that enlarges the current IceCube Array, in order to increase the performance and statistics in the detection and characterization of PeV astrophysical neutrino sources [14]. As the absorption length of Cherenkov-light in the ice at South Pole

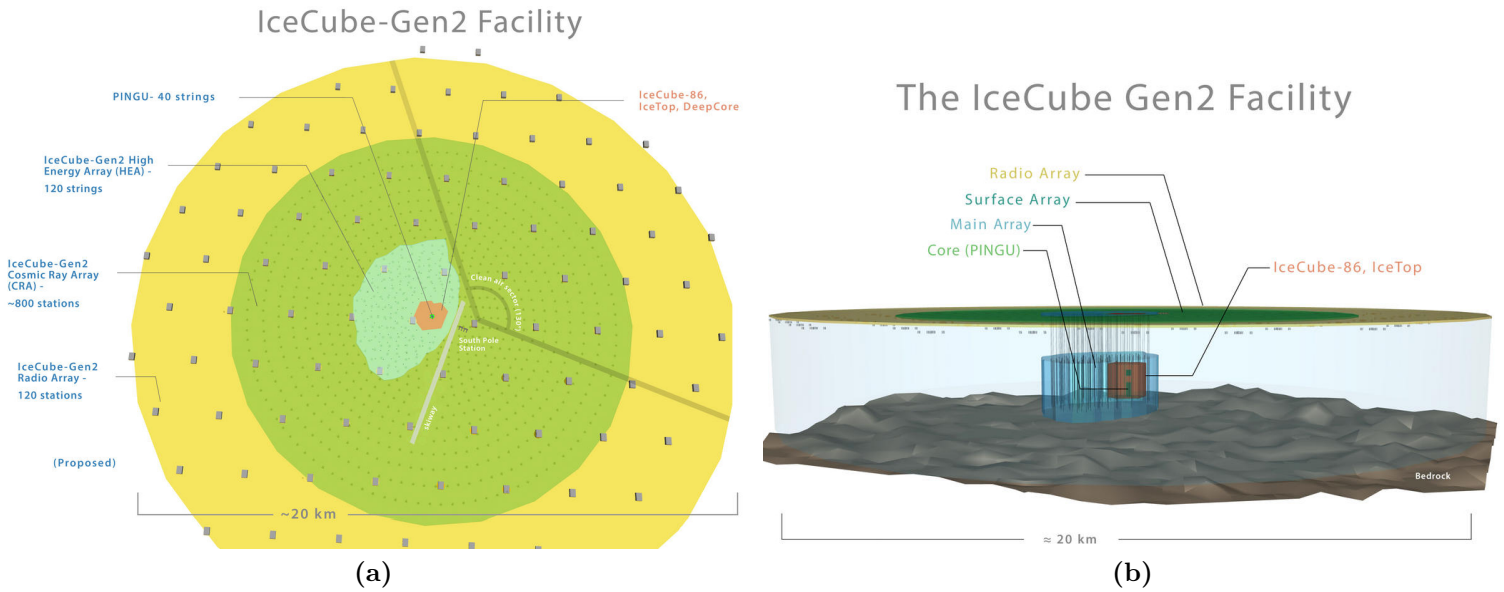


Figure 2.5: Sketches of IceCube Gen2. (a) The left is a top view with the current detectors in the small orange part in the center. Taken from [20]. (b) The right is a side view with the current detectors in the small orange part in the center. Taken from [21].

is in the order of 100 m, the spacing of the strings in the new Main Array can be enlarged to above 250 m [13]. Hence a ten times larger effective target volume, compared to the 1 km^3 IceCube Array, is planned to be deployed with approximately the same amount of strings. Another in-ice extension is the PINGU core in the center of DeepCore, whose dense string and DOM spacing is designed to detect low energy neutrinos in more detail. PINGU is planned to provide precision measurements of neutrino oscillations as well as indirect searches for dark matter particles down to GeV energies. It would also be able to determine the neutrino mass ordering. The baseline design for the Cherenkov-light sensors of both new in-ice arrays is a modernized IceCube DOM. Besides modernizing the electronics, it is investigated to incorporate several PMTs per DOM, since this would improve the directional resolution. On the other hand the calibration devices for the new in-ice detectors shall improve the event reconstruction by determining the optical properties of the ice in more detail [14].

Beyond the in-ice extensions IceCube Gen2 will comprise the Surface Array, which is the extension of IceTop, and the Radio Array. As sketched in figure 2.5, both surface arrays are planned to be much larger in area than IceTop. As the Surface Array protrudes beyond the in-ice Main Array, the former enables for a veto of downward-going atmospheric muons and neutrinos even for large zenith angles, which is not achieved by the current IceTop detector. Whether the new stations will also consist of frozen water Cherenkov tanks or scintillator panels, is not certain yet, as the deployment efforts have to be balanced against the costs per station. The Radio Array will be even larger than the Surface Array and will have a diameter of 20 km. As the effective target volume of the Radio Array is at 10^{18} eV about 100

times larger than the current one of IceCube, it is expected to be able to detect neutrinos from the GZK-cutoff, where ultra high energetic cosmic rays interact with the cosmic microwave background, explained in section 2.1. Concluding IceCube Gen2 has the objective to resolve current issues in astrophysics and particle physics by taking the promising path of multi-messenger and multi-wavelength astrophysics [14].

One interesting perspective of IceCube and IceCube Gen2 is the incorporation of imaging air Cherenkov telescopes, IceActs, as the hybrid detection of extensive air showers with this technique could further improve the veto for downward-going IceCube Array events as well as the measurement of the cosmic ray flux and composition.

3. The IceAct Telescope

This chapter tells the story of a recycled dustbin [22] that became FAMOUS [23] [24] [25] [26] and spun off into IceAct [27] [28] [29]. The IceAct Imaging Air Cherenkov Telescope is based on the FAMOUS fluorescence telescope, which is developed by the Pierre Auger Observatory group of the III. Physikalisches Institut A, RWTH Aachen. This chapter will first give an introduction to Cherenkov light emission and the principle of Imaging Air Cherenkov Telescopes (IACTs). Then an argument on pros and cons of integrating IceActs into IceCube is carried out. Subsequently the design of the IceAct telescope is presented, focussing on the camera, which is the subject of this thesis.

3.1 Cherenkov Light

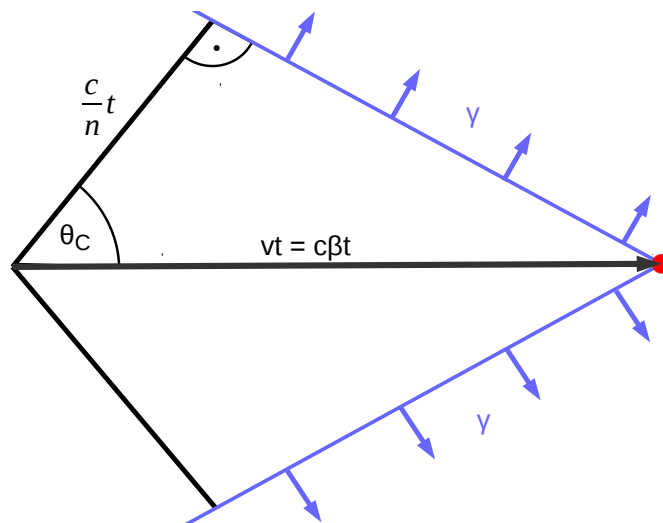


Figure 3.1: Cherenkov light cone. A particle (red dot) traversing a non-dispersive medium with refractive index n at a velocity $v = \beta c$ faster than the speed of light in this medium $\frac{c}{n}$ emits Cherenkov photons (blue) under an angle Θ_C within the time t . Adapted from [30].

Cherenkov light was first discovered by Pavel Alekseyevich Cherenkov in 1937, who observed asymmetric light pulses in liquids, which were penetrated by fast electrons [31]. When charged particles traverse a non-dispersive medium with refractive index n at a velocity $v = \beta c$ faster than the speed of light in this medium $\frac{c}{n}$, Cherenkov

light is emitted by the polarized medium into a cone under an angle Θ_C following [31]:

$$\cos(\Theta_C) = \frac{1}{\beta n} . \quad (3.1)$$

This so-called Cherenkov-effect, whose acoustic analogue is the Mach cone, is shown in figure 3.1, which depicts a particle emitting blue photons into a cone within the time t and the speed of light in vacuum c . The spectrum of Cherenkov light, so the amount of photons N emitted per travelled distance dx and per frequency interval $d\omega$ is given by the Frank-Tamm-formula [32]:

$$\frac{d^2 N}{dx d\omega} = \frac{Z^2 \alpha}{c} \sin^2(\Theta_C) , \quad (3.2)$$

where Z is the particle's charge in units of the elementary charge e and α is the fine structure constant. Consequently the number of Cherenkov photons increases with their frequency and with the energy of the charged particle. Frank and Tamm as well as Cherenkov were awarded the Nobel Price for physics in 1958 for the discovery and interpretation of the Cherenkov-effect. Cherenkov light detectors are for example used in the LHCb experiment at CERN to identify charged particles [33] or in imaging air Cherenkov telescopes, which are the topic of section 3.1.1.

In the case of IceAct, where the atmosphere is the medium, mostly deep blue and UV photons reach the telescope, which is important for the selection of materials and light detectors that have to be transparent and efficient in this frequency region. The peak wavelength for atmospheric Cherenkov photons is about 340 nm, because the atmosphere absorbs smaller wavelengths [34].

As the IceCube Array uses the Cherenkov light cone of secondary charged particles, to reconstruct the direction of the primary neutrino, it is important to note that the direction of motion of charged particle and neutrino only differs by less than 1° at 1 TeV neutrino energy improving for even larger relativistic boosts [35].

3.1.1 Imaging Air Cherenkov Telescopes

The objective of Imaging Air Cherenkov Telescopes (IACTs) is the detection of extensive air showers in order to determine energy and type of the primary particle as well as the arrival direction. Typically Cherenkov photons of an air shower reach the ground within a short pulse of a few nanoseconds length. Though the time averaged photon yield generated by air showers is ten thousand times smaller than the night-sky background yield, the intensity within these short pulses is comparable with the brightest astronomical sources. The baseline design of IACTs comprises a mirror focussing the Cherenkov light onto a pixelated fast single photon detector read out by electronics with GHz sampling and processed via sophisticated trigger circuits. Supplementary instruments include fast light sources for the calibration of the IACT as well as local weather stations, cameras and lasers monitoring the atmosphere [34]. The discovery of air Cherenkov light was achieved by Galbraith and Jelley detecting sub-microsecond light pulses in coincidence with a cosmic ray array using the telescope shown in figure 3.2 (a). This first air Cherenkov telescope was built from a dustbin, a recycled searchlight mirror of 25 cm diameter and a PMT of 5 cm diameter

[22]. Today's IACTs commonly utilize Winston cones (see section 5.2) rejecting background light coming from beyond the field of view and focussing the Cherenkov light on smaller PMTs; prominent examples are:

- H.E.S.S.: located in Namibia comprising four telescopes of 12 m diameter and a central telescope of 28 m diameter [36].
- MAGIC: located on the Canary island of La Palma comprising two telescopes of 17 m diameter [37].
- VERITAS: located in Arizona comprising four telescopes of 12 m diameter [38].

These IACTs have a typical field of view between 3° and 5° as well as a large aperture and camera size, as the former ensures that the whole shower is imaged while the latter lowers the energy threshold [34]. IACTs with common PMT sensors usually detect ten Cherenkov photons per TeV shower energy and per m^2 mirror area, while 50-100 photons have to be detected for a stable trigger and image reconstruction. This requirement and especially shower fluctuations limit the single pixel field of view to a minimum of about 0.1° [39]. The sketch in figure 3.2 (b) depicts the operating principle of IACTs. Secondary particles of an air shower cause the emission of Cherenkov light, which is most intense in about 10 km height above sea-level for gamma ray initiated showers, as this is the location of the shower maximum X_{max} where the most secondary particles are present. For a typical Cherenkov angle of less than 1° in air the Cherenkov light reaches the ground on a washed out circle of (100-150) m radius [39]. The image taken by three IACTs can be seen in the upper right of figure 3.2 (b). Each IACT produces an elliptically shaped image, which allows for the reconstruction of the primary particle direction and energy, since the primary energy is proportional to the amount of particles in the shower and the Cherenkov light intensity. The energy of an 1 TeV gamma ray can be reconstructed with an error of about 15% [34]. As indicated in figure 3.2 (b), it is advantageous to operate multiple IACTs in stereoscopic mode imaging the shower from different perspectives. This improves the energy and directional reconstruction as well as the determination of the primary particle [34].

Most IACTs focus on the detection of gamma-ray initiated showers, which are more collimated than cosmic ray showers and only comprise an electromagnetic component. In contrast, cosmic rays produce a larger hadronic component and thereby a larger muonic component. So the distinction can be performed via the shower shape and the muon content [39]. Since the depth of X_{max} is linked to the chemical composition of the primary particle [5], it is worthwhile to place the IACTs in high altitudes to improve energy threshold and composition resolution, which is given for IceAct, as IceCube is located in about 3 km height above sea-level.

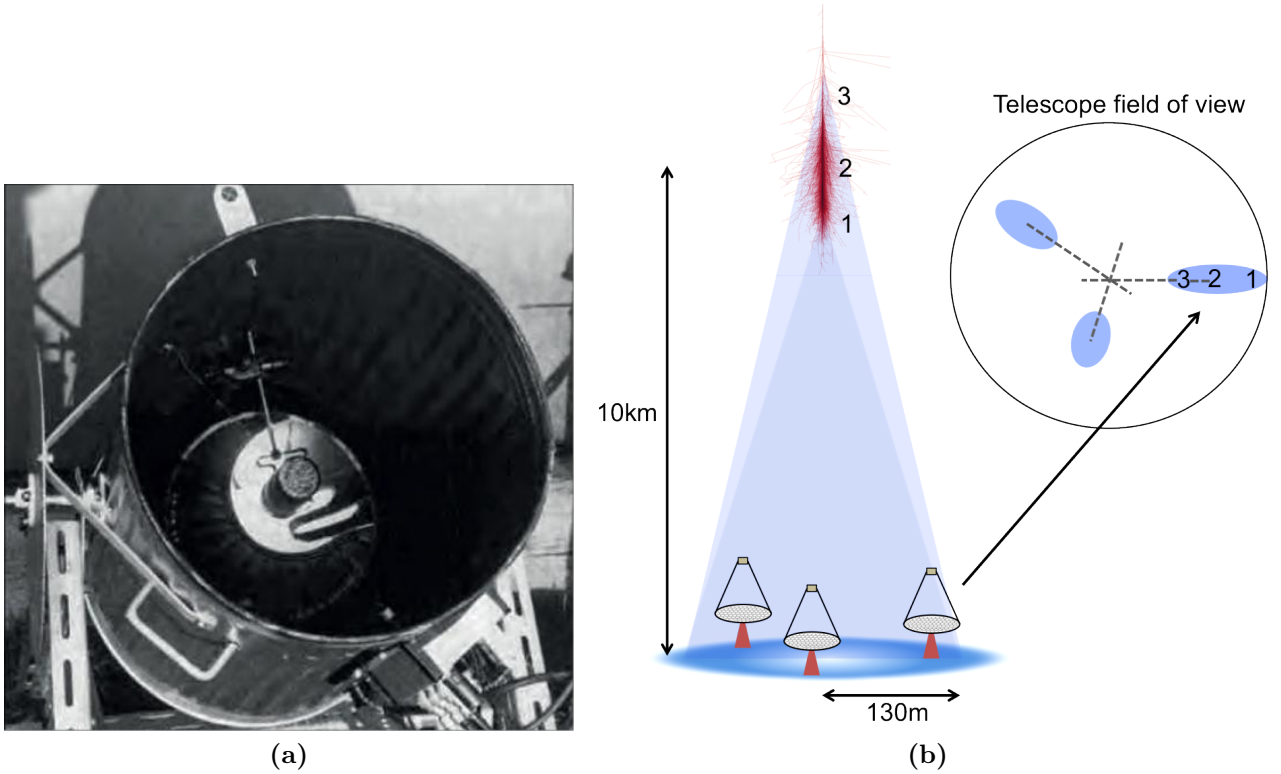


Figure 3.2: First air Cherenkov telescope and principle of IACTs. (a) The left is an image of the first air Cherenkov telescope consisting of a dustbin, a mirror taken from a searchlight and a PMT [22]. Taken from [40]. (b) The right is a sketch depicting the principle of IACTs. Taken from [34].

The first IACT using silicon photomultipliers (SiPMs, see section 3.3.1.1) as light detectors is the FACT telescope located on the Canary island of La Palma equipped with a 9.5 m^2 mirror and a camera with 1440 pixels [41]. Simulations of the light-collecting cones designed for the FACT camera were part of this thesis and resulting plots are presented in the figures 7.1 and 7.2 of the appendix. The CTA Observatory is a planned future array of differently sized IACTs [42]. The IceAct data acquisition (DAQ) is based on a TARGET application-specific integrated circuit, which is developed by and for the CTA collaboration [43].

3.2 Why IceAct?

It is planned to deploy an array of IceAct telescopes at the IceCube Neutrino Observatory for the detection of Cherenkov photons from extensive air showers. A first IceAct demonstrator with seven pixels and 4° field of view was brought to South Pole in the beginning of 2016 and took almost one month of stable data in physics mode in the winter season of 2016 [29]. Here and in the following the field of view describes the angle within which the telescope is sensitive to light. So 4° field of view equal $\pm 2^\circ$ maximum angle of incidence. Figure 3.3 shows the IceAct demonstrator in 2017 on the roof of the IceCube Lab centrally above the IceCube Array.

First analyses of the SiPM waveforms [44] and the synchronisation of IceAct and IceCube Array events [45] [46] were carried out at the III. Physikalisches Institut B, RWTH Aachen. Though sophisticated analyses of the IceAct data are still ongoing, first events were found that are coincident with the IceCube Array and IceTop [29], which is promising for the veto application of a future IceAct telescope array.



Figure 3.3: IceAct demonstrator at South Pole. IceAct in the foreground of the figure is placed on the roof of the IceCube Lab centrally above the IceCube Array. The red light is turned off when there is no person on the roof. In the background there is an aurora australis. Provided by [47].

The advantage of a ground based air shower array like IceTop is the duty cycle of practically 100% and the wide field of view in the order of one steradian. However the high energy threshold can not compete with an IACT, particularly for increasing zenith angles [39]. IceAct has an energy threshold of about 50 TeV, which is much smaller than the 300 TeV threshold of IceTop [29]. Furthermore an IceAct array would have a larger zenith coverage, such that also the background for neutrinos with large zenith angles can be vetoed. As these neutrinos traverse more ice before entering the IceCube Array than neutrinos from the zenith, their interaction and detection probability for the IceCube Array is higher. While IceTop has a small active area, which suffers from the spacing between the stations, which would even have to be enlarged for an array extension, IceAct has the advantage of using the whole atmosphere in its field of view as active volume. Therewith the detection efficiency of IceAct is superior [27]. Nevertheless the duty cycle of IceAct is smaller, as IACTs can not operate in the daytime and in regions with light pollution. Moreover the cloud coverage has to be reasonably small [34]. Taking daytime per year and cloud

coverage into account, 25% of a year provide darkness and good weather conditions for IceAct [29]. This fraction lacks further investigations, as also moon and auroras austrais as seen in figure 3.3 have to be considered. Therefore a new sky camera was recently installed, taking pictures of the whole sky for more sophisticated analyses. The effect of snow drift and micro ice crystals that might make the lens of IceAct opaque is no issue up to now, but will be investigated more precisely in the next Pole season using for example a dummy placed on the snow at a distance of the IceCube Lab [47].

Other objectives of IceAct are the determination of the chemical composition of cosmic rays around the knee and the constraint of uncertainties in hadronic interaction models used for the simulation of air showers. In addition IceAct might calibrate the cosmic ray flux detected by IceCube [28]. Since there are many applications for IceAct at IceCube and because single telescopes and even whole telescope arrays are comparably cheap and easy to deploy and operate [27], IceAct is suited for IceCube Gen2 and for other experiments in astroparticle physics.

An example for the application of IceAct and FAMOUS, respectively, together with air shower arrays is the collaboration of the FAMOUS group with the HAWC gamma ray observatory in Mexico [25]. Recently a FAMOUS prototype with 61 pixels and a 12° field of view was placed in the center of HAWC and successfully took coincident data [48].

3.3 Design of the IceAct Telescope

In order to achieve the goals discussed above, the design of the IceAct telescope is optimized for a large field of view and a high duty cycle adapting to the harsh environment at South Pole, which offers temperatures as low as -82°C , a very low humidity and frequently wind speeds in the range of $25 \frac{\text{m}}{\text{s}}$ that are accompanied by micro crystalline snow [27]. Considering this a sealed housing as shown in figure 3.4 is realized.

Starting at the top of the telescope and following the path of the photons, the first part of the telescope is a glass plate of 3.8 mm thickness. The glass is placed in front of the Fresnel lens to shield the lens from dust, the low temperatures and the small micro crystalline snow that might get stuck in the grooves of the lens, melting due to the thermal energy deposited during the impact and refreezing, which degrades the performance and lifetime of the lens. The utilized BOROFLOAT 33 glass was chosen because of its durability and its especially high UV-transparency [49].

The lens is an ORAFOL SC 943 positive Fresnel lens with an aperture of 549.7 mm and a focal length of 502.1 mm at 546 nm wavelength yielding an f-number of $\frac{f}{D} \approx 0.9$ [50]. A Fresnel lens is obtained from a spherical lens by the division into concentric annular sections, called "grooves". The height of each groove is minimized to the height of the groove with the maximum gradient resulting in a discontinuous surface comparable to a saw tooth shape. The Fresnel lens of IceAct has 10 grooves per millimetre and is only 2.5 mm thick [50]. Therewith the Fresnel lens has the advantage of being thin and light-weight compared to spherical lenses at the cost of a decreased imaging quality, which is still sufficient for the application in IceAct. On top of this, a Fresnel lens is advantageous compared to a mirror design, as the

former ensures an enclosed design and simplifies the design of the focal plane in the prototyping phase, since the focal plane is not crossed by the path of light. Details and measurements of the Fresnel lens mounted on IceAct are given in [26].

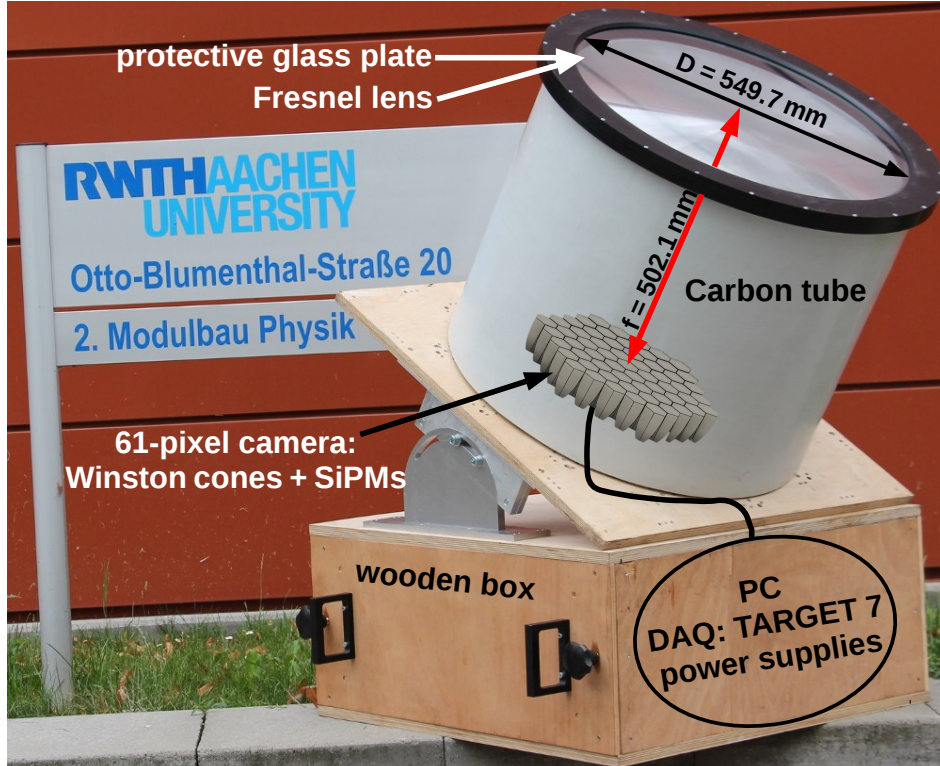


Figure 3.4: IceAct telescope design. The crucial parts of the telescope are labelled. The entrance aperture of the Fresnel lens is $D = 549.7\text{ mm}$ and the focal length $f = 502.1\text{ mm}$ at 546 nm wavelength. A carbon tube and a wooden box protect the 61-pixel camera and the electronics, respectively. Picture provided by [47].

The lens is attached to a carbon tube which sets the distance to the focal plane and shields the camera from background light as well as snow and wind. A black textile at the inner wall of the tube absorbs stray light. The usage of carbon is preferred to aluminium, which was used in previous prototypes, as carbon is both light-weight and robust. Moreover non-painted metals pose a danger in Antarctica, as human skin promptly freezes to the surface.

The 61-pixel camera, consisting of light-collecting cones, SiPMs and a DAQ system, is located in the focal plane of the Fresnel lens and will be described in detail in section 3.3.1. The DAQ is based on a TARGET 7 module described in section 4.1 and connected to the IceCube Lab via a standard DOM mainboard. Details on the synchronization and trigger path of IceAct and IceCube can be found in [45] and [46].

The DAQ system as well as a PC and power supplies are located in a protective wooden box under the telescope body, which can be tilted in zenith between $\pm 45^\circ$ via a mount. The usage of wood for the box is based on the experience that wood is very durable in the Antarctic environment, while being cheap and light-weight. In order to protect the electronics from the cold the box is additionally insulated and

light bulbs are placed inside of the wooden box for heating on demand, e.g. before the electronics are turned back on after a longer shut down.

3.3.1 The Camera

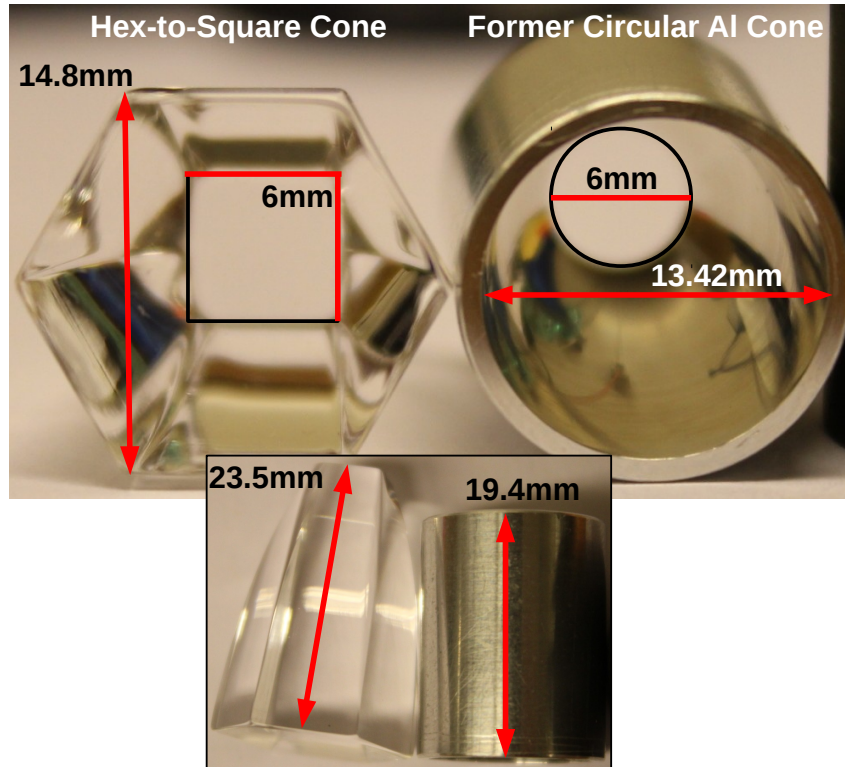


Figure 3.5: Comparison of former and new light-collecting cone. On the left, the final Hex-to-Square cone made from solid PMMA and developed in this thesis has a hexagonal entrance window of 14.8 mm minimum diameter and a $6 \times 6 \text{ mm}^2$ exit window. On the right, the former Circular Al cone has circular windows of 13.42 mm and 6 mm diameter, respectively. The final Hex-to-Square cone is, with 23.5 mm, longer than the former Circular Al cone of 19.4 mm length. The cone development is the topic of chapter 5.

The uppermost part of the camera are light-collecting cones, whose entrance windows are situated in the focal plane of the Fresnel lens, as shown on the right of figure 3.6. Figure 3.5 presents a comparison of the former Circular aluminum (Al) cone and the final Hex-to-Square cone developed in this thesis. Both cones are based on the Winston cone design, described in section 5.2. Though the cone development is topic of chapter 5, a short introduction to the design of these two cone types is given here for the sake of completeness. As shown on the left of figure 3.5, the final Hex-to-Square cone made from solid PMMA has a hexagonal entrance window of 14.8 mm minimum diameter and a square exit window of $6 \times 6 \text{ mm}^2$. The hollow former Circular Al cone on the right has circular windows of 13.42 mm and 6 mm diameter, respectively. The final Hex-to-Square cone is, with 23.5 mm, longer than the former Circular Al cone of 19.4 mm length. The latter is installed in the telescope

prototype used for the first measurements with the TARGET 7 DAQ in Erlangen presented in chapter 4, while the final Hex-to-Square cone is planned to be installed in the IceAct prototype that will be sent to South Pole at the end of 2017.

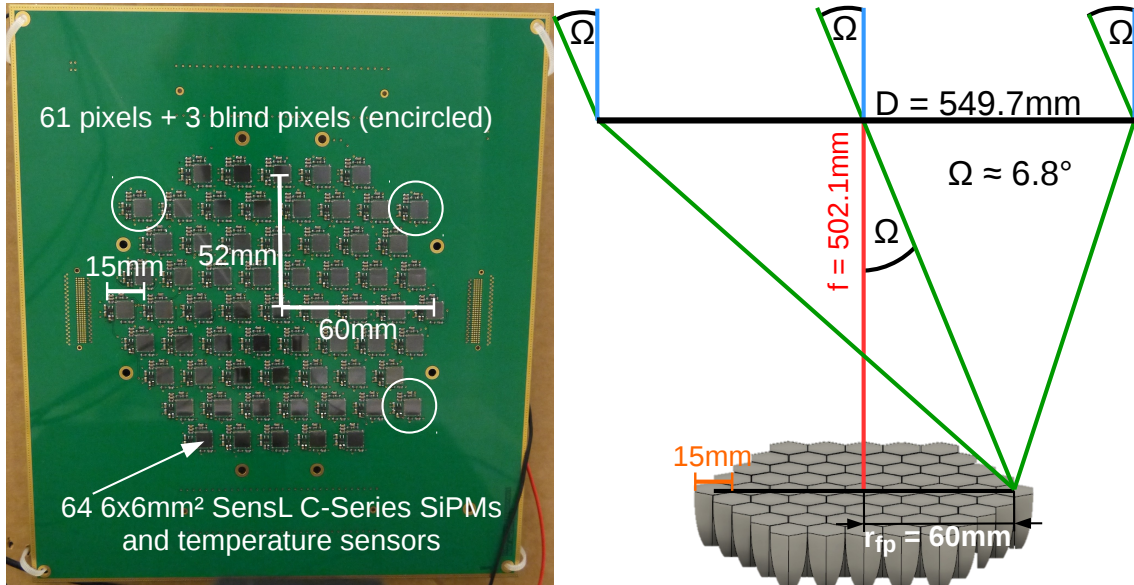


Figure 3.6: Design of the camera. The left shows the SiPM PCB developed by the III. Physikalisches Institut, RWTH Aachen. 64 $6 \times 6 \text{ mm}^2$ SensL C-Series SiPMs and temperature sensors are arranged on a hexagonal grid with 15 mm horizontal spacing. 61 SiPMs will be coupled to light-collecting cones and form a hexagon with a 60 mm circumscribed radius and a 52 mm inscribed radius. The remaining 3 SiPMs are blind. On the right the camera geometry is sketched with the Fresnel lens of aperture $D = 549.7 \text{ mm}$ and 61 light-collecting cones in the focal plane ($f = 502.1 \text{ mm}$). The angle of view of the camera for cones in the edges of the hexagon equals $\Omega \approx 6.8^\circ$.

The light-collecting cones are coupled to SiPMs, which detect the light coming from the Fresnel lens and are read out by the TARGET 7 DAQ. The principle of SiPMs as well as the specific SiPMs used or investigated for IceAct are topic of section 3.3.1.1. The left part of figure 3.6 presents the printed circuit board (PCB) of the SiPMs developed by the III. Physikalisches Institut, RWTH Aachen. 64 $6 \times 6 \text{ mm}^2$ SensL C-Series SiPMs and temperature sensors are arranged on a hexagonal grid with 15 mm horizontal spacing. This spacing on the hexagonal grid limits the size of the entrance window of the light-collecting cones, while the exit window has to fit to the SiPM, motivating the development of the final Hex-to-Square cone carried out in this thesis. The temperature sensors are deployed to be able to adjust the bias voltage of the SiPMs for temperature compensation. Though 3 SiPMs are blind for symmetry reasons, these SiPMs are beneficial for cross-checks of e.g. the dark noise. 61 SiPMs are coupled to light-collecting cones and form a hexagon with a 60 mm circumscribed radius, where the radius is measured from the center of the hexagon to the center of the SiPMs that are located in the edges of the hexagon. From the

focal length f and the radius of the focal plane $r_{fp}(\phi)$ which is dependent on the azimuth angle ϕ due to the hexagonal shape, the field of view $fov(\phi)$ of the IceAct telescope is calculated via:

$$fov(\phi) = 2\Omega(\phi) = 2 \arctan \left(\frac{r_{fp}(\phi)}{f} \right), \quad (3.3)$$

where $\Omega(\phi)$ is the angle of view sketched in figure 3.6. Inserting the circumscribed radius of the hexagon $r_{fp} = 60$ mm results in the maximum field of view of $fov_{max} = 13.6^\circ$, while inserting the inscribed radius of the hexagon $r_{fp} = 52$ mm results in the minimum field of view of $fov_{min} = 12^\circ$ which is equal to about 0.034 sr. Compared to the field of view of the IACTs presented in section 3.1.1 this is a very wide field of view, since this is beneficial for the veto application of IceAct. In addition the wide field of view per pixel of about 1.6° is chosen, because the Fresnel lens limits the attainable resolution and not least because a smaller field of view per pixel is not necessary for the chief objectives of IceAct.

3.3.1.1 Silicon Photomultipliers

Silicon photomultipliers (SiPMs) are a rather new semiconductor device for single photon detection competing with PMTs in various applications in physics and medical imaging. SiPMs are used both for the IceAct telescope and for a measurement setup in this thesis.

Doping and p-n junctions

The working principle of SiPMs is based on a p-n junction sketched in figure 3.7. Semiconductors are materials with a band gap between the valence band, which is filled with electrons, and the empty conduction band in the order of $E_G \approx 1$ eV. The probability that a free electron occupies an eigenstate of energy E at a temperature T is given by the Fermi-Dirac statistics [51]:

$$n_F(E) = \frac{1}{1 + e^{\frac{E-\mu}{k_B T}}}, \quad (3.4)$$

where k_B is the Boltzmann constant and μ the chemical potential, which equals the Fermi energy E_F at the absolute zero temperature $T = 0$ K. This distribution is a step function for $T = 0$ K and becomes smeared out for higher temperatures. In a continuous case E_F equals the energy of the highest energetic eigenstate that is occupied, or, if there is a gap between this eigenstate and the lowest energetic unoccupied eigenstate, E_F equals the energy in the middle of the band gap. As electrons with a thermal energy of about 25 meV at room temperature are not able to cross the band gap $E_G \approx 1$ eV between valence and conduction band, there are no free electrons in the conduction band. Moreover only photons with an energy larger $E_\gamma = hf \geq E_G$ can possibly excite electrons to the conduction band, where h is Planck's constant and f the frequency of the photon. By doping the semiconductor with impurity atoms in the lattice, a new band structure forms as sketched in the schematic on the top of figure 3.7 (a), which also enables photons with smaller energies to excite electrons. If the impurity atom has one more valence electron than

the semiconductor, the Fermi energy is shifted upwards and an additional donor level E_D emerges just below the conduction band, such that electrons can be excited into the conduction band even at room temperature. The counterpart to this so-called n-doping is p-doping, where impurity atoms with one less valence electron shift the Fermi level down and create an acceptor level just above the valence band, such that the missing electrons, so-called holes, can move freely inside of the lattice of the doped semiconductor equivalent to the excess electrons in the n-doped case [51].

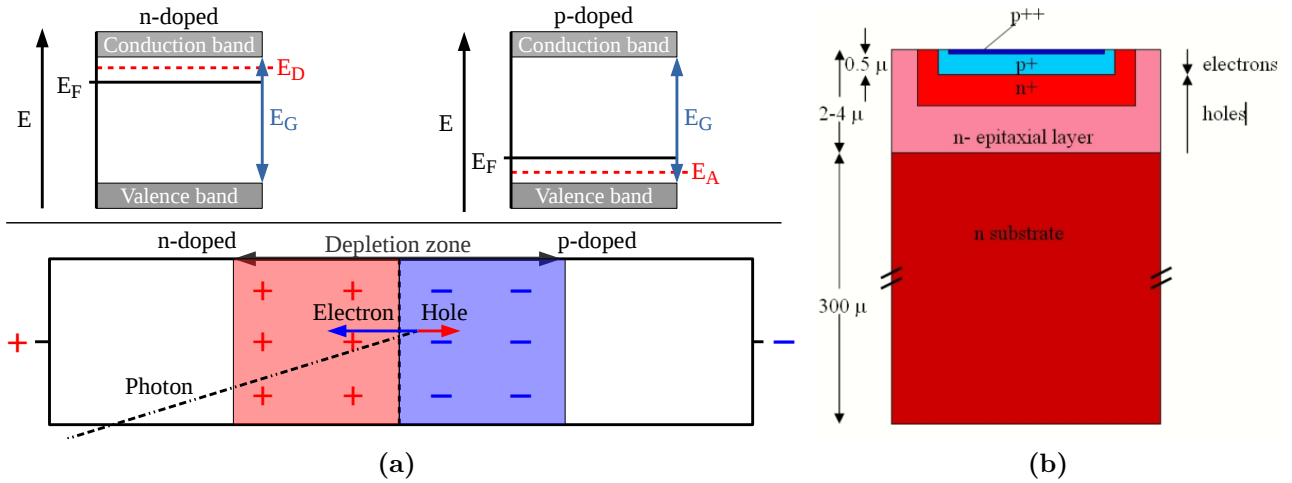


Figure 3.7: p-n junction and G-APD cell structure of an SiPM. (a) The left depicts the principle of a p-n junction. The top shows the energy bands of n- and p-doped semiconductors with the Fermi energy E_F , the gap energy E_G and the donor and acceptor levels E_D and E_A , respectively. The bottom presents a schematic of a p-n junction with a reverse bias voltage that enlarges the depletion region located at the contact area of p- and n-doped semiconductors. Impinging Photons may produce electrons and holes in the depletion region inducing a current via generated avalanches. Adapted from [52]. (b) The right depicts the structure of a p-on-n type SiPM cell with a thin but strongly charged p-doped layer at the surface and a thick n-doped layer at the bottom. This type is used to detect photons in the blue and UV region, as they interact close to the surface where electrons most probably induce an avalanche. Taken from [53].

A p-n junction shown at the bottom of figure 3.7 (a) consists of an n-doped and a p-doped semiconductor brought into contact. Since there are free electrons and holes, respectively, they annihilate around the interface leaving a depletion region, where there are no free charge carriers but on the other hand the charged nuclei of the doped semiconductors. Similar to a capacitor an electromagnetic field builds up limiting the expansion of the depletion region to a distance to the interface at which the gap energy equals the energy of the generated electromagnetic field. A photon interacting in the depletion region, as well as thermal excitations, generate electron hole pairs, which are separated by the electromagnetic field, such that a current flows. Since this current only flows in one direction, the p-n junction can be

operated as a diode [51].

From photodiode to SiPM

Though the p-n junction already is capable of detecting photons, the thermal noise superimposes the small signal current induced by photons. Therefore in case of a photodiode a reverse bias voltage is applied with the anode at the n-doped side and the cathode at the p-doped side as shown at the bottom of figure 3.7 (a). This additional electromagnetic field enlarges the width of the depletion zone proportional to the square root of the applied electromagnetic potential. The minimum number of photons that can be detected with these photodiodes is in the range of 200 – 300 [53]. A further improvement of the photon sensitivity is achieved by increasing the reverse bias voltage until the electrons gain enough energy in the electromagnetic field of the depletion region to generate electron hole pairs themselves such that an avalanche evolves in the n-doped region. These so-called avalanche photodiodes have a gain smaller than 10^4 enabling them to detect down to 10-20 photons [53]. Geiger-mode avalanche photodiodes (G-APDs) use a reverse bias voltage above the breakdown voltage of the diode V_{Bd} , such that also the holes generate an avalanche in the p-doped region, so in the breakthrough direction. This results in a self-sustaining breakdown of the diode that has to be quenched by the voltage drop over a high-ohmic resistor connected in series to the G-APD. With a gain in the range of $10^5 - 10^7$ G-APDs are able to detect single photons like PMTs, but since the G-APD breaks down, there is no information on the number photons that created the signal. Therefore an SiPM is composed of several G-APD cells [53].

SiPMs

The structure of a p-on-n type G-APD cell of an SiPM is shown in figure 3.7 (b). Several differently doped layers are combined beginning with a thin but strongly charged p-doped layer at the surface and a thick n-doped layer at the bottom. This type is used to detect photons in the blue and UV region, as these short wavelength photons interact just after entering the silicon close to the surface where electrons most probably induce an avalanche, due to the large electromagnetic field between the strongly doped p and n layers. An SiPM typically consists of thousands of these G-APDs. An equivalent circuit diagram of an SiPM is given in figure 3.8 (a). The SiPM cells, consisting of a G-APD cell and a serial quenching resistor, are connected in parallel, such that the SiPM signal equals the sum over each cell signal. The amplitude of a cell breakdown A_i is dependent on its capacitance C and the overvoltage $V_{Ov} = V_{Bias} - V_{Bd}$, where V_{Bias} is the bias voltage of the SiPM [53]:

$$A_i = \frac{C}{e} \cdot V_{Ov} , \quad (3.5)$$

where e is the elementary charge. Figure 3.8 (b) contains an oscilloscope screenshot showing the amplified noise signal produced by an SensL C-Series MicroFC-SMTPA-30035 SiPM of $3 \times 3 \text{ mm}^2$ size. Since the signals of the cells directly sum up to the SiPM signal, the waveforms have discrete amplitudes corresponding to the number of cell breakdowns marked as multiples of a photo equivalent (p.e.). The typical waveform of an SiPM consists of a fast exponential voltage drop and a slower ex-

ponential recovery tail. Here the recovery time of the SiPM cells τ depends on the quenching resistance R_q and the cell capacitance C via $\tau \sim R_q C$. A single photo equivalent arises either from an impinging photon or from noise phenomena. The dark noise of an SiPM is primarily generated by thermal noise degrading the single photon detection performance. Another noise phenomenon is optical crosstalk of photons generated in a cell avalanche and triggering additional cell breakdowns in neighbouring cells. Optical crosstalk increases with the overvoltage. Moreover afterpulsing generates noise in SiPMs by delayed releases of charge carriers that were trapped in impurities of the silicon during an avalanche [53].

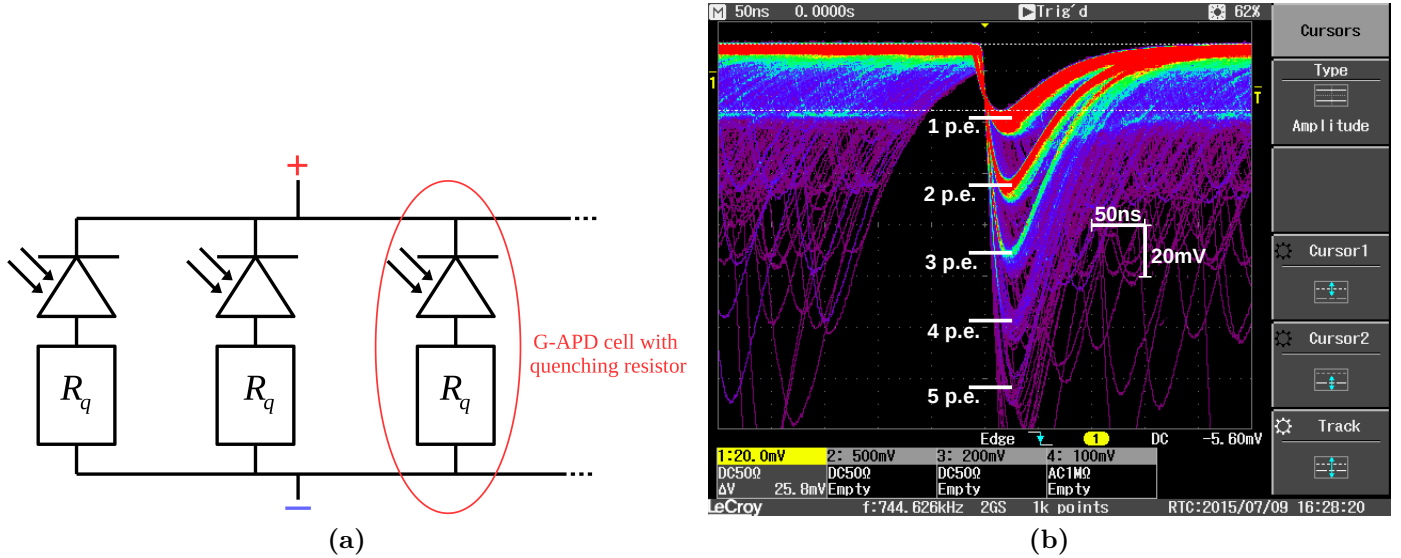


Figure 3.8: Equivalent circuit diagram and typical waveforms of SiPMs. (a) The left shows an equivalent circuit diagram of an SiPM with the cells consisting of a G-APD and a quenching resistor connected in series. Taken from [52]. (b) The right depicts an oscilloscope screenshot of the amplified noise signal produced by an SensL C-Series MicroFC-SMTPA-30035 SiPM of $3 \times 3 \text{ mm}^2$ size. The waveforms have discrete amplitudes corresponding to the number of cell breakdowns marked as multiples of a photo equivalent (p.e.). The event rate is color-coded and the load equals 50Ω . Voltage ($div = 20 \text{ mV}$) is plotted against time ($div = 50 \text{ ns}$). Adapted from [52].

Compared to PMTs SiPMs have a smaller dynamic range, which is dependent on the size of the SiPM cells, the cell recovery time and the inherent SiPM noise [54]. The photon detection efficiency (PDE) of an SiPM neglecting the recovery time is given by [53]:

$$PDE = QE \cdot \varepsilon \cdot P_{trigger} , \quad (3.6)$$

with the quantum efficiency of the active area QE , the fill factor ε , which is limited by the desire of a low crosstalk and the size of the quenching resistors, and the probability that an impinging photon triggers a cell breakdown $P_{trigger}$. Though the PDE of an SiPM is comparable to a PMT, SiPMs have the disadvantage of a strong dependence of the PDE on the overvoltage. In addition the overvoltage is

dependent on temperature, which also affects gain and PDE [53]. However this effect can be eliminated by power supplies that adjust the bias voltage of the SiPMs with temperature, as for instance the power supply developed by the III. Physikalisches Institut, RWTH Aachen, for the FAMOUS telescope, which is also deployed in the IceAct prototype tested in Erlangen [24]. Moreover a comparably high noise rate degrades the performance of SiPMs. Furthermore the comparably small active area of SiPMs is disadvantageous for large-scale applications. Nevertheless SiPMs have several advantages over PMTs like an insensitivity to magnetic fields as well as a lower bias voltage (< 100 V) and reduced power consumption of $< 50 \mu\text{W}/\text{mm}^2$ [53].

	Hamamatsu S12573-100X	SensL C-Series MicroFC-60035-SMT	SensL J-Series MicroFJ-60035-TSV
Temp. and V_{Ov}	25°C, 1.4 V	21°C, 2.5 V (5 V)	21°C, 2.5 V (5 V)
Breakdown voltage	≈ 64 V	24.45 V \pm 0.25 V	24.5 V \pm 0.25 V
Sensor size	6 x 6 mm ²	6 x 6 mm ²	6.07 x 6.07 mm ²
Cell / Pitch size	100 μm (pitch)	35 μm	35 μm
Number of cells	3600	18980	22292
Fill factor	78.5 %	64%	75 %
Coating refractive index	1.41	1.59 at 420 nm	1.53 at 436 nm
PDE at λ_p	35 % at 450 nm	31 % at 420 nm (41 %)	38 % at 420 nm
Spectral response range	270 nm - 900 nm	300 nm - 950 nm	200 nm - 900 nm
β	60 $\frac{\text{mV}}{\text{K}}$	21.5 $\frac{\text{mV}}{\text{K}}$	21.5 $\frac{\text{mV}}{\text{K}}$
Gain	$2.8 \cdot 10^6$	$3 \cdot 10^6$	$2.8 \cdot 10^6$ ($5.3 \cdot 10^6$)
0.5 p.e. dark noise	2 MHz	1.2 MHz	1.7 MHz (2.9 MHz)
Optical Crosstalk	35 %	7 %	7 % (22 %)
Afterpulsing	< 1 %	0.2 %	0.1 % (1 %)
Recovery time	≈ 23 ns	95 ns	48 ns

Table 3.1: Characteristics of the SiPMs used for IceAct. β represents the temperature dependence of the breakdown voltage ($V_{Bd}(T) = V_{Bd}(T_0) + \beta \cdot (T - T_0)$). The Hamamatsu SiPM is used in the FAMOUS / IceAct prototype tested in Erlangen. The SensL C-Series SiPM is part of the current camera, while the J-Series SiPM is the planned future device for IceAct, as the J-Series provides a better PDE in the UV-range. The values in brackets correspond to the bracketed overvoltages V_{Ov} in the first row. All the values are taken from the datasheets (left to right): [55], [56] and [57], respectively.

SiPMs in IceAct

The most important advantages of SiPMs for the IceAct telescope are the compactness and ruggedness as well as the low costs per piece because of mass production. Especially the robustness of SiPMs against accidental illumination and the resulting larger duty cycle prompts the deployment of SiPMs instead of PMTs in IceAct, since

PMTs might be damaged by moonlight.

Table 3.1 gives an overview on the characteristics of the SiPMs that are used in or investigated for the IceAct telescope. The Hamamatsu S12573-100X 6x6 mm² SiPM is installed in the IceAct prototype tested in Erlangen. This SiPM is already outdated and correspondingly consists of 2x2 channels that can be read out separately, because 6x6 mm² large SiPMs could not be manufactured from a single silicon wafer decreasing the performance due to V_{Bd} and accordingly gain fluctuations between the four wafers. The SensL C-Series MicroFC-60035-SMT SiPM is part of the current camera. Finally the SensL J-Series MicroFJ-60035-TSV SiPM is the planned future device for IceAct. The Hamamatsu SiPM is typically operated at an overvoltage of 1.4 V while the SensL SiPMs are operated at 5 V, though the SensL datasheet values are often given for 2.5 V overvoltage. β in table 3.1 represents the temperature dependence coefficient of the breakdown voltage, which is given by

$$V_{Bd}(T) = V_{Bd}(T_0) + \beta \cdot (T - T_0) , \quad (3.7)$$

where T_0 equals 25° for the Hamamatsu SiPM and 21° for the SensL SiPMs. An important parameter of the SiPM installed in IceAct is the PDE in the deep blue and UV range, which is the highest in case of the SensL J-series SiPM.

4. First Night Sky Measurements with the new TARGET 7 DAQ

In November of 2016 an IceAct prototype was brought to the Erlangen Centre for Astroparticle Physics by a part of the IceAct group from the RWTH Aachen to take first night sky measurements with the complete 61-pixel camera and the new TARGET 7 DAQ. Since the TARGET 7 module was developed by the CTA group in Erlangen, the know-how of the scientists in Erlangen was precious for the first deployment of TARGET 7 in the IceAct telescope and vice versa the scientists from Aachen shared their experience in compact imaging air Cherenkov telescopes. In the following sections an overview on the TARGET 7 module is given and subsequently the first night sky measurement is presented. First measurements, temperature dependence tests and calibrations of the TARGET 7 module were carried out by several Bachelor students at the III. Physikalisches Institut, RWTH Aachen [58] [59] [60] [61].

4.1 TARGET 7 ASIC and TARGET 7 Module

The TeV Array Readout Electronics with GSa/s sampling and Event Trigger (TARGET) is an application-specific integrated circuit (ASIC) designed to digitize and trigger on the analog signal of 16 channels with a sampling frequency of 1 GS/s and an storage array of 16384 cells corresponding to waveforms of about $16\ \mu\text{s}$ length. The Gigahertz sampling and buffer length already indicate that the TARGET 7 ASIC is designed for IACTs detecting air Cherenkov flashes of $\gtrsim 5\ \text{ns}$ length with a large latency due to stereoscopic measurements [62]. The development of the TARGET ASICs and the TARGET modules consisting of multiple ASICs is carried out by the CTA collaboration. TARGET 7 combines sampling, triggering and digitization in a single ASIC [62].

TARGET 7 ASIC

Figure 4.1 shows a functional block diagram of the TARGET 7 ASIC with 16 channels and 4 trigger groups each triggering on the analog sum of 4 channels. The sampling circuit utilizes a timebase generator to control 16 switched capacitor arrays each with 64 cells divided into two blocks operated in a continuous ping-pong sampling mode, where one block samples while the other is read out. During this readout the blocks of 32 cells are written into storage arrays with 512 blocks, since this separation of sampling and storage enlarges the bandwidth by reducing the input impedance while providing continuous sampling due to the ping-pong mode as

well as a deep buffer of 16384 capacitor cells. A 12-bit analog-to-digital converter (ADC) can randomly access the blocks of the storage array when triggered such that 32 cells of each of the 16 channels are digitized simultaneously and sent to a field-programmable gate array (FPGA). A Serial-parallel interface allows for configurations, triggering and readout of a single or multiple TARGET 7 ASICs via the FPGA [62].

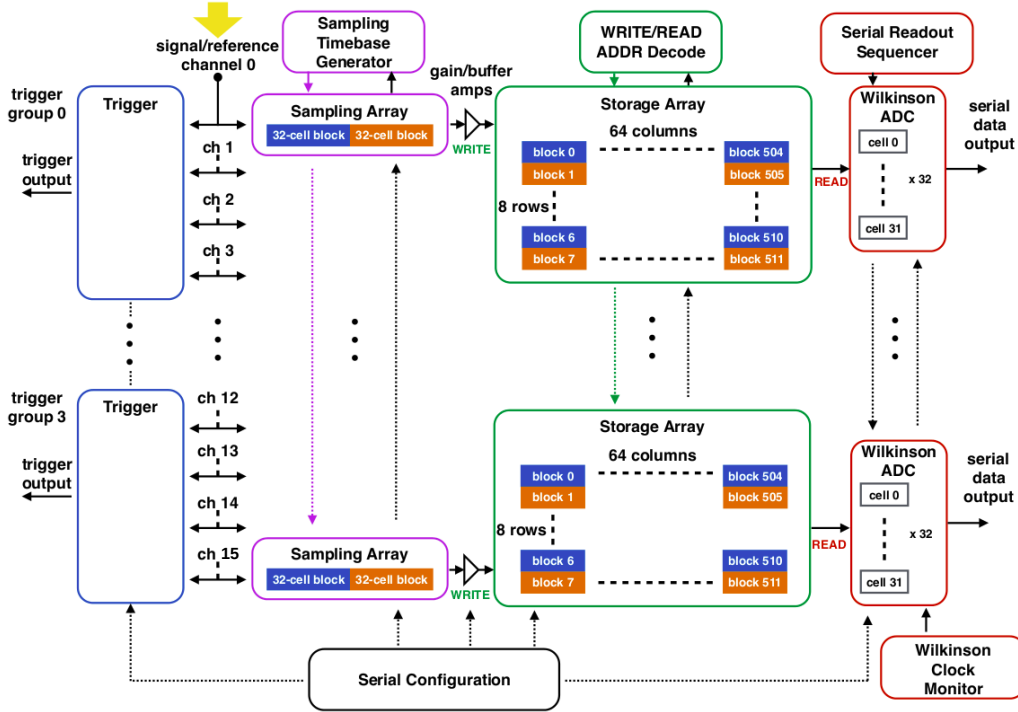


Figure 4.1: Functional block diagram of the TARGET 7 ASIC. The ASIC comprises 16 channels. The trigger circuit consists of 4 groups each triggering on the analog sum of 4 channels. The sampling circuit consists of a timebase generator controlling switched capacitor arrays with 64 cells divided into 2 blocks for continuous ping-pong sampling into storage arrays with 512 blocks consisting of 32 cells. An ADC can randomly access the blocks of the storage array when triggered. A Serial-parallel interface allows for configurations. Taken from [63].

Table 4.1 gives an overview on the specifications of the three consecutive versions of the TARGET ASIC, namely TARGET 5, TARGET 7 and the latest version consisting of a sampling and digitization ASIC TARGET C and a triggering ASIC T5TEA. From TARGET 5 to TARGET 7 the dynamic range is improved to 1.9 V and the charge resolution at 10 p.e. is halved to 4 % for 4 mV/p.e. photon equivalent heights. Since TARGET 5 has issues with the crosstalk of trigger and sampling circuit, additional amplification stages are implemented along the trigger path in TARGET 7 to enforce the signal against pickup noise. Moreover the trigger output is changed to a low-voltage differential signal and the isolation is improved. Nonetheless the minimum trigger threshold redoubled to 50 mV with a trigger noise of 15 mV for TARGET 7. Therefore the latest version splits trigger and sampling circuit into two separate ASICs resulting in a better minimum trigger threshold [63]. Since these

TARGET C and T5TEA ASICs as well as the modules equipped with them are still tested by the CTA collaboration, TARGET 7 is the default device for the next IceAct prototype.

	TARGET 5	TARGET 7	TARGET C + T5TEA
Characteristics			
Number of Channels	16	16	16
Sampling frequency (Gsa/s)	0.4 - 1	0.5 - 1	0.5 - 1
Size of storage array	16384	16384	16384
Digitization clock speed (MHz)	~ 700	208	500
Samples digitized simultaneously	32 × 16	32 × 16	32 × 16
Trigger (sum of 4 channels)	integrated	integrated	companion
Performance			
Dynamic Range (V)	1.1	1.9	≥ 1.9
Integrated non linearity (mV)	75	40	≤ 70
Charge linearity range (pe*)	4 - 300	1 - ≥ 300	1 - ≥ 300
Charge resolution at 10 pe*	8%	4%	≤ 4%
Charge resolution at > 100 pe*	2%	≤ 0.8%	≤ 0.8%
Minimum trigger threshold (mV)	20	50	≤ 8
Trigger noise (mV)	5	15	≤ 1

* assuming 4 mV/pe

Table 4.1: Characteristics of consecutive TARGET versions. TARGET 7 features a dynamic range of 1.9 V, a charge resolution at 10 p.e. of 4%, assuming 4 mV/p.e., and a minimum trigger threshold of 50 mV. Taken from [43].

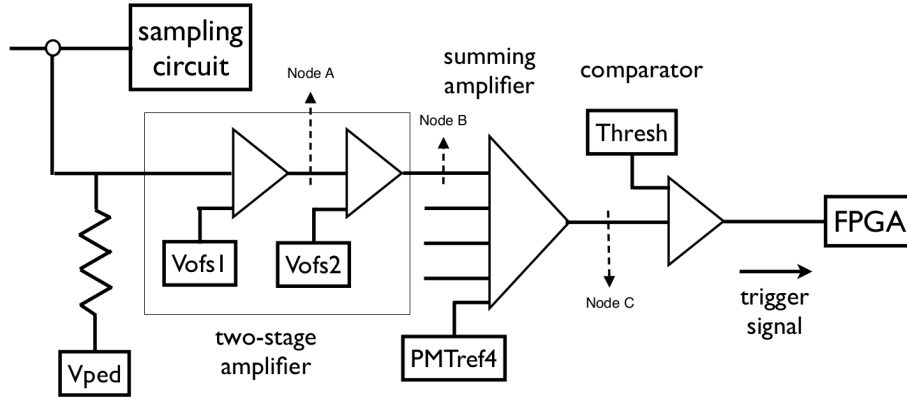


Figure 4.2: Trigger circuit of the TARGET 7 ASIC. The adjustable bias voltages and nodes for voltage measurements are drawn in. V_{ped} is a DC pedestal voltage applied to all channels, while V_{ofs1} and V_{ofs2} are channel specific. PMT_{ref4} and $Thresh$ are set for each trigger group so for 4 channels at once. While V_{ped} , V_{ofs1} , V_{ofs2} and PMT_{ref4} are already determined and fixed for signals with positive pulses, $Thresh$ has to be determined for each measurement individually. Taken from [64].

In order to obtain reasonable waveforms and triggers of signals injected into TARGET 7, different DC voltages labelled in the trigger circuit in figure 4.2 can be adjusted by 12-bit digital-to-analog converters (DACs) ranging from 0 V to 2.5 V. A

pedestal voltage V_{ped} is applied to all channels to shift the signal into the positive linear operating range of the ADC, since the ADC can not process negative voltages. Furthermore there are two offset voltages V_{ofs1} and V_{ofs2} at first and second stage of a two-stage amplifier, respectively. These voltages are channel specific such that all channels can be matched to provide for equal trigger probabilities. Hereafter the signals of 4 consecutive channels each are fed into an analog summing amplifier whose offset voltage PMT_{ref4} consequently is trigger group specific. V_{ped} , V_{ofs1} , V_{ofs2} and PMT_{ref4} are already optimized and fixed for signals with positive pulses by CTA members in Erlangen taking care of the dynamic range of TARGET 7. The threshold voltage of the final comparator $Thresh$ has to be determined for each trigger group and each measurement individually. Here it has to be stressed that a smaller $Thresh$ DAC count results in a higher threshold voltage [64].

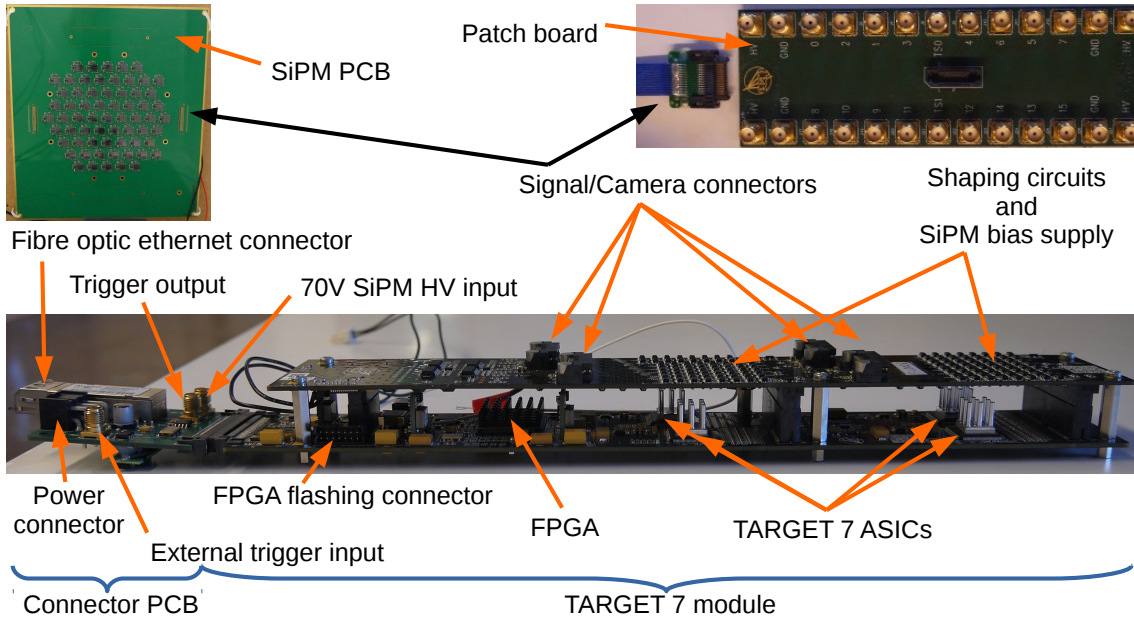


Figure 4.3: The TARGET 7 module.

TARGET 7 module

Since the IceAct telescope deploys 64 SiPMs, a TARGET 7 module as shown in figure 4.3 utilizing 4 TARGET 7 ASICs with 16 channels each is used. As described in the previous paragraph, V_{ped} , V_{ofs1} , V_{ofs2} and PMT_{ref4} are already optimized for this module with version number *EU0006*. To communicate with the TARGET 7 module, a connector PCB has to be connected to the TARGET 7 module as shown on the bottom of figure 4.3. The communication is carried out via a fibre optic Ethernet connector connected to a network switch and subsequently a PC with installed TARGET software. A power connector supplies the module with 12V for the main components, 3.3V for digital components and another 12V for Peltier elements, where the latter should not be connected due to an issue of the module that is currently used in Aachen. The connector PCB moreover comprises three SMA connectors for a trigger output, a 70V high voltage input for the SiPMs and an external trigger input that requires a positive pulse of at least 2V amplitude and

8 ns length to trigger the readout of the 4 ASICs.

In total the TARGET 7 module provides three different trigger modes including a hardsync trigger that triggers continuously with a rate of 120 Hz, the just mentioned external trigger and the internal trigger of the 4 ASICs that triggers on groups of 4 signal channels. The TARGET 7 module consists of two PCBs stacked one above the other, where the bottom PCB houses the FPGA, a connector for the flashing of the FPGA and the 4 TARGET 7 ASICs. The top PCB of the module is assembled with circuits that shape the input signal and provide the bias supply of the SiPMs. The shaping is differential and the gain is dependent on the signal shape, as the amplifiers have a low bandwidth. An SiPM like signal with a 5 ns rising edge and a 30 ns falling edge of 1 mV amplitude entering the 1 k Ω terminated input will be amplified to 16 mV corresponding to a gain of about 16. The signal has to be positive and a minimum height of 50 mV after the shaping is required for stable triggering, as discussed for the TARGET 7 ASIC. Though a flyback diode only protects the module from input voltages above 3.3 V, the shapers already saturate at 1.8 V limiting the attainable input signal height [65]. On the top PCB of the TARGET 7 module there are also 4 signal connectors which provide the input for in total 64 channels. Moreover the patch board with SMA connectors depicted on the top right of figure 4.3 can be connected via a signal connector to investigate the 16 channels of a single ASIC. In addition the patch board enables for injecting a signal from a pulse generator for test measurements, trigger scans or calibrations. In case of the IceAct prototype, the signal connectors are connected to the SiPM PCB. The possibility of using the TARGET 7 module as temperature compensating power supply for the SiPMs of IceAct is not yet made use of. Nevertheless the power supply option was tested with an input high voltage of 30 V instead of the default 70 V, since the IceAct prototype deploys SensL SiPMs with a breakdown voltage in the range of 25 V and not in the range of 63 V as in case of Hamamatsu SiPMs, which are the default device considered during the development of the TARGET 7 module by the CTA collaboration. During the operation the voltage can be adjusted individually for each trigger group, thus for 4 SiPMs each, by regulating the low-side voltage between 0 V and about 4 V with a 12-bit ADC such that bias voltages between 26 V and 30 V can be set.

4.1.1 Software for Operation of the TARGET 7 Module

The TARGET software is installed on the Lenovo ThinkPad T440p laptop with the inventory number 1175893-0 and an Ubuntu 16.04 LTS operating system. Copies of the most recent programs are available on an IceAct external hard disk drive. The files TM7_FPGA_Firmware0xA0000104.def and TM7_ASIC.def in the Target/TargetDriver/config directory are register maps of the FPGA and the ASIC, respectively. The most important programs are testerT7.cc in the Target/TargetDriver/src_exe directory, takedata.py in the Target_IceAct/Erlangen directory and ScanEvents_current.py in the Target_IceAct directory. With testerT7.cc the TARGET 7 module can be initialized and reconnected. Moreover the adjustable voltages of the trigger circuit are set here, where the *Thresh* value always has to be determined by a trigger scan that is already implemented in this program but highly

manual. On top of that the code from the test of the power supply application of the module for the SiPMs can be found in this program. With the takedata.py program waveforms of all 64 channels can be taken and saved into binary *FITS* files. Currently the length of the waveforms is limited to 448 ns and 448 samples, respectively, which is not an issue, because SiPM signals of short-lived air Cherenkov pulses are studied. The generated *FITS* files are read and waveforms as well as telescope camera event views are plotted by the ScanEvents_current.py program.

4.2 Erlangen Setup and Measurement Procedure

Figure 4.4 shows the setup of the night sky measurements carried out on top of the roof of the Erlangen Centre for Astroparticle Physics. The telescope faces eastwards under a zenith angle of about 45° . In this direction there are some luminous lanterns well below the roof edge and fortunately a dark forest in the distance. The weather conditions presenting a cloudless sky and faint fog were comparably good for Germany's autumn. Nevertheless a ventilator in the background of figure 4.4 is used to prevent condensation of the cold and wet air on the glass plate in front of the Fresnel lens. The design of the Ice-Act prototype is described in section 3.3. Specific to this prototype are the aluminum tube, the 64 channel power supply with temperature compensation for the SiPMs ([24]) and the 61-pixel camera consisting of the former Circular Al cones presented in section 3.3.1 and the Hamamatsu S12573-100X 6x6 mm² SiPMs. An Aim-TTi PL303QMT-P power supply [66] provides 12 V and 3.3 V to the TARGET 7 module, which is connected to the SiPMs and, via a network switch, to a Laptop with the TARGET software. The power supply for the SiPMs is controlled by a Windows program on another laptop and adjusts the bias voltage automatically for temperature variations. Figure 4.5 (a) presents the allocation of the color-coded four ASICs of the TARGET 7 module to the camera pixels. The three pixels outside of the hexagon are the blind pixels. Figure 4.5 (b) shows the allocation of the color-coded trigger groups to the camera pixels. During

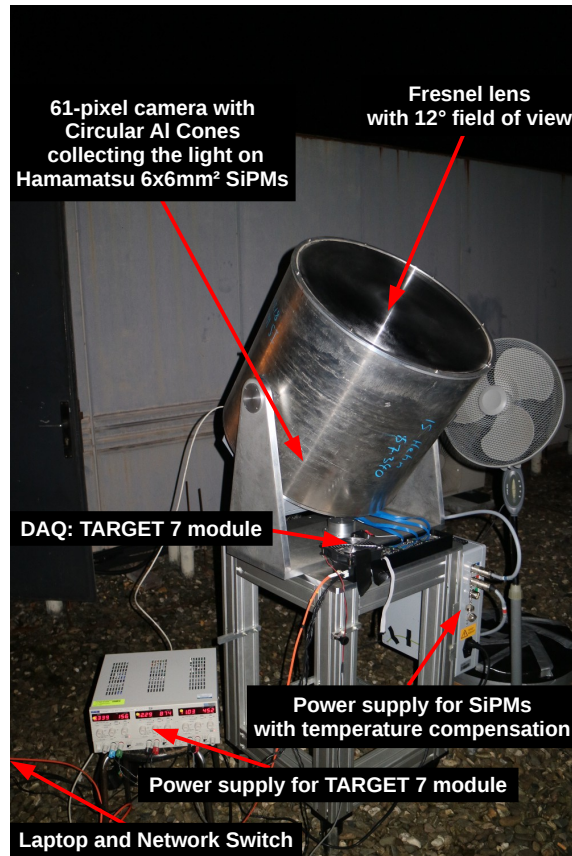


Figure 4.4: Setup in Erlangen. The Ice-Act prototype with 61-pixel camera, consisting of former Circular Al cones and 6x6 mm² Hamamatsu SiPMs, is read out by a TARGET 7 module.

the measurements, the SiPMs are powered with 1.4 V overvoltage as suggested by the specifications of the Hamamatsu SiPM given in table 3.1.

At the beginning of the night sky measurements, the SiPMs are exposed to the night sky background light and trigger scans are carried out to tune the trigger threshold of each of the 16 trigger groups such that trigger rates of a few Hertz are observed. In figure 4.6 the threshold values of each trigger group are plotted in DAC counts for the pixel layout given in figure 4.5. The zeroth trigger group is flagged white in the center of the camera, as it has a much higher threshold value of 3100 DAC counts compared to all the other groups. It has to be stated that a lower DAC count corresponds to a higher threshold voltage. Therefore the zeroth trigger group has the by far lowest threshold, since this trigger group featured a very low trigger rate. On the other hand, the trigger groups of the third ASIC are set to a very high threshold corresponding to 30-50 DAC counts, as this ASIC is known to be buggy. This also reasons that all blind pixels are connected to the buggy third ASIC as shown in figure 4.5 (a), because therewith the trigger performance on physics events from the night sky is least affected. The majority of the trigger groups is set to a threshold value in the range of 300-400 DAC counts. With these settings the main measurement is started. Several runs each of 10-minute duration are performed taking waveforms of 256 ns length of each of the 64 SiPMs when triggered. After the first run a malfunction of the power supply of the SiPMs affected the performance of the following runs, which could neither be resolved by restarting the power supply nor by an additional tuning of the trigger thresholds. After shutting down the power supply of the SiPMs and setting the trigger thresholds into the noise region, dark noise measurements were performed in order to obtain data for a baseline calibration.

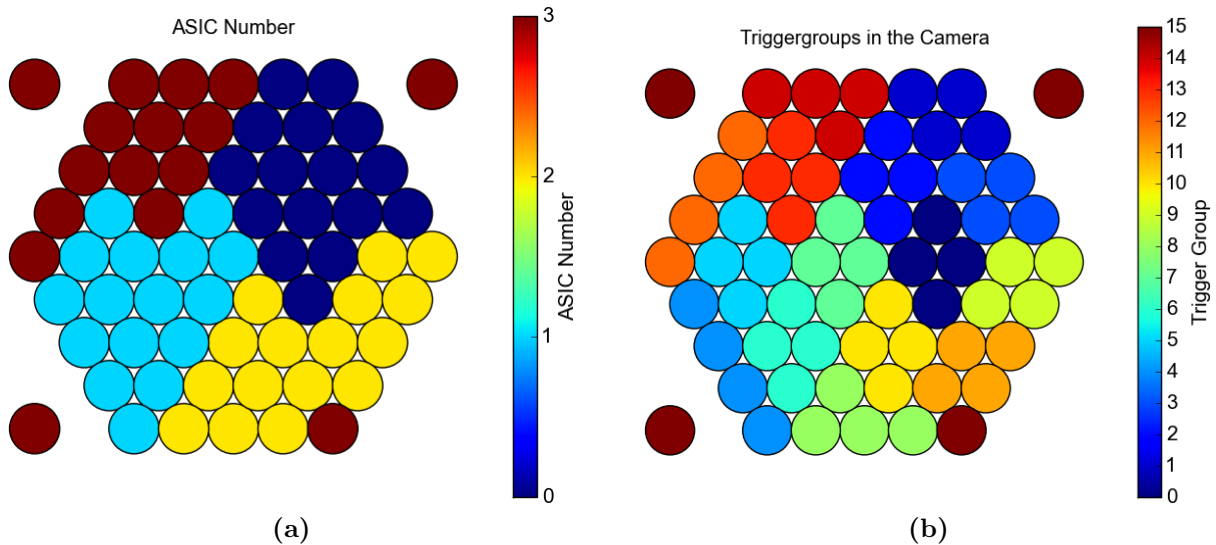


Figure 4.5: Pixel layout of the camera. (a) The left presents the allocation of the color-coded four ASICs of the TARGET 7 module to the camera pixels. The three pixels outside of the hexagon are the blind pixels. (b) On the right the number of the trigger group is denoted by the color.

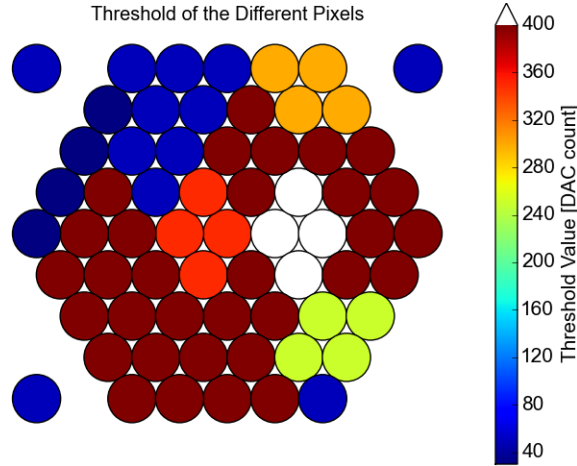


Figure 4.6: Threshold values of trigger groups. The threshold value is labelled by the color, where the white trigger group in the center has a threshold value of 3100 DAC counts. A lower DAC count corresponds to a higher threshold voltage.

4.3 Event View and First Analysis

As explained in the previous section, a malfunction of the power supply of the SiPMs affected all runs except for the first run, only this run 0 is analysed in the following. Therewith 10 minutes of data and correspondingly 2183 events are investigated. Moreover it is important to note that the following analysis is preliminary and exclusively meant to investigate the capability of the TARGET 7 module to work as DAQ for the IceAct prototype. The analysis searches indications, whether an event might originate from Cherenkov light produced by air showers. A more sophisticated analysis as well as further measurements are essential for physics analyses.

The baseline is shifted to 0 ADC counts for the event selection by subtracting the mean of the first 100 samples from each sample of the waveform. Because of an adjusted trigger delay, the signal pulses are expected to emerge at about the 140th sample corresponding to a delay of 140 ns. Figure 4.7 shows event 1633 of run 0 as a generic example of a signal event that might originate from an air shower, since four SiPMs feature a large signal pulse at the expected position of about 140 ns after the measurement start. As the TARGET 7 module shapes the signal differentially, the signal does not exactly look like a raw SiPM pulse. The signal pulses are about 20 ns long while the whole waveform comprises 256 ns. Because these short-lived but intense signals are characteristic for Cherenkov light from air showers, events of this type are selected by demanding that within a time window between 120 ns and 160 ns at least three SiPMs have to yield a maximum signal height of 300 ADC counts after the baseline shift. With this cut 11 events are selected from a total of 2183 events within run 0. For every event, the maximum ADC count after the baseline shift and within the time window of 120-160 ns as well as the timestamp of the maximum are plotted in a camera view as shown for event 1633 in figure 4.8. Figure 4.8 (a) shows the maximum signal height within a time window of 120-160 ns of each SiPM in ADC counts. The clustering of the SiPMs yielding the highest signals on the bottom right indicates that the event might have been generated by

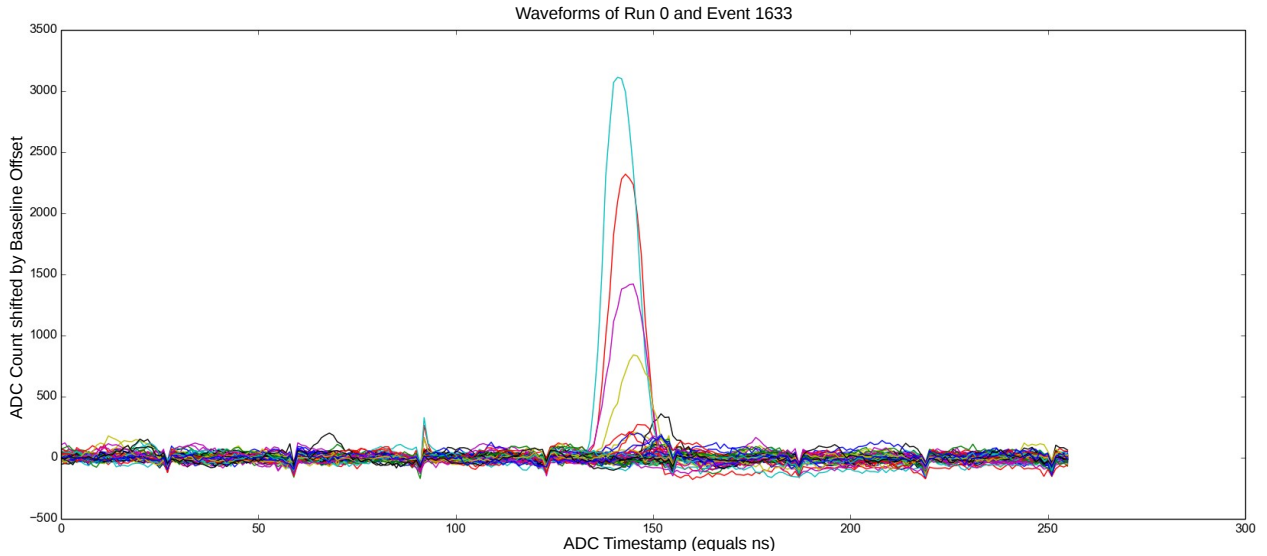


Figure 4.7: Waveforms of air shower candidate event 1633. The baseline of each SiPM is shifted to 0 ADC counts. About 140 ns after the measurement start four SiPMs feature a large signal pulse.

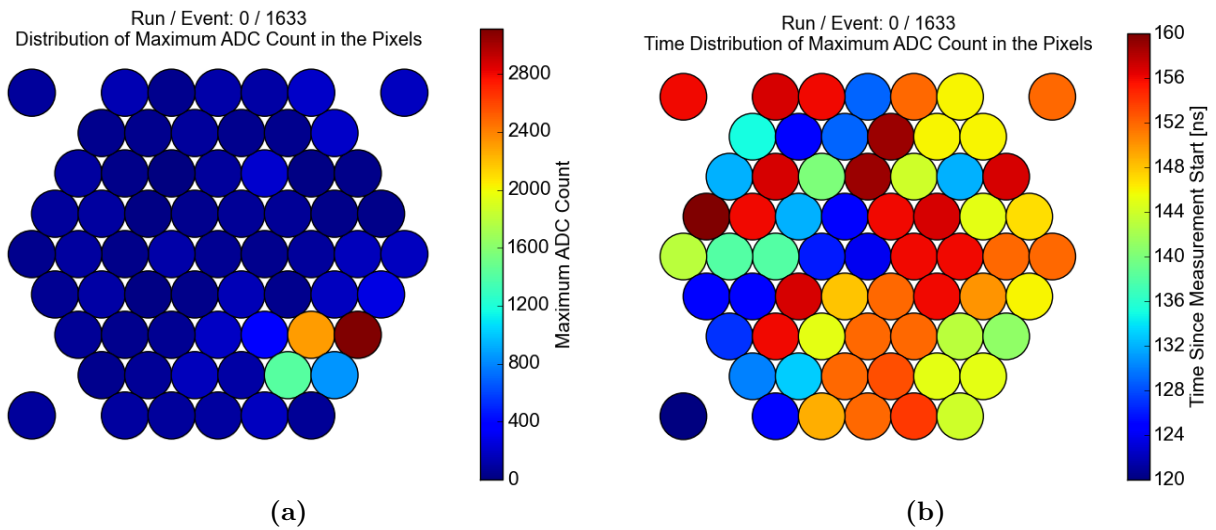


Figure 4.8: Camera view of event 1633. (a) The left shows the maximum signal height within a time window of 120-160 ns of each SiPM in ADC counts. (b) The right shows the distribution of the time corresponding to the maximum signal height.

an air shower. Figure 4.8 (b) shows the distribution of the time corresponding to the maximum signal height. While the left side of the camera has random timing, the timing on the right side and especially on the bottom right contains a structure, which fits to the structure of the signal height in figure 4.8 (a). Therewith the SiPM pulses of event 1633 are correlated in their position on the camera and in time, which substantiates the assumption that this event was generated by an air shower. The same arguments hold for all 11 events, that have been selected.

The waveform in figure 4.9 is the brightest event detected in run 0. Several SiPMs

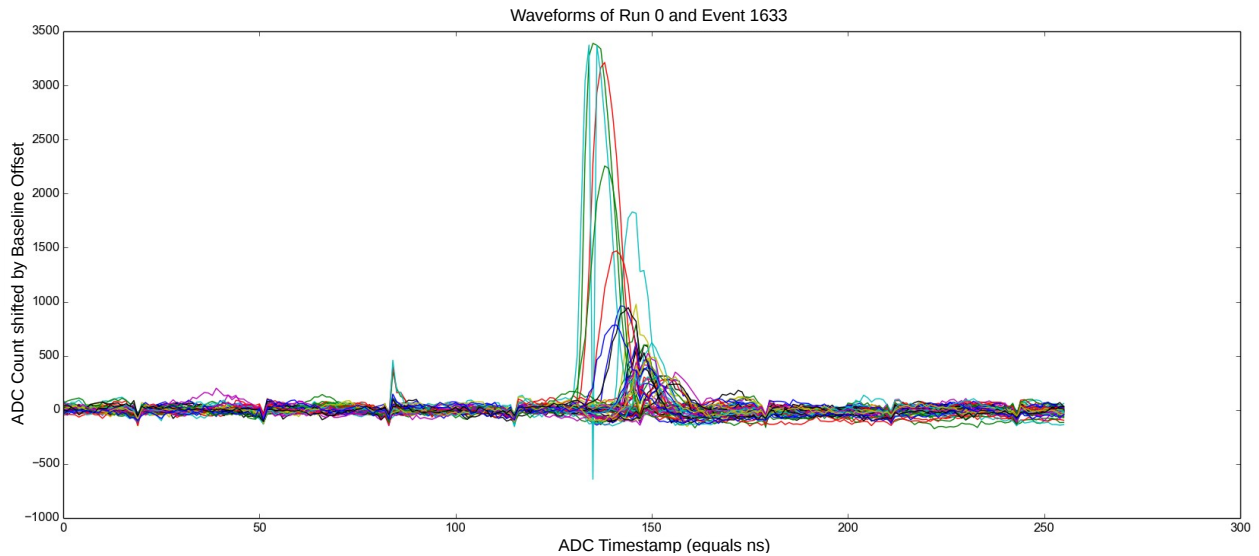


Figure 4.9: Waveforms of brightest air shower candidate event 2102. The baseline of each SiPM is shifted to 0 ADC counts. About 140 ns after the measurement start several SiPMs feature a large signal pulse.

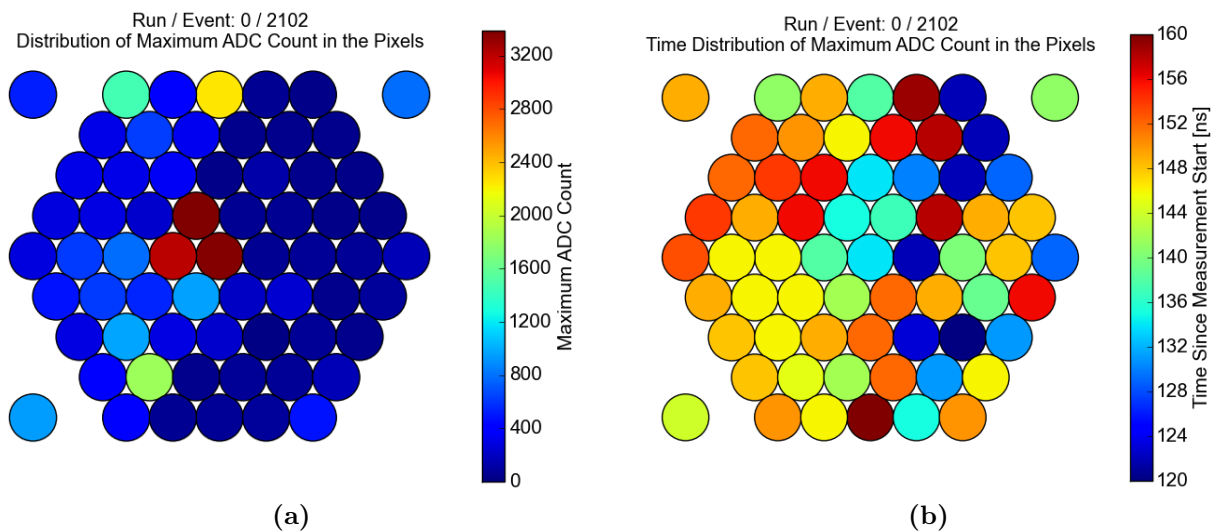


Figure 4.10: Camera view of brightest event 2102. (a) The left shows the maximum signal height within a time window of 120-160 ns of each SiPM in ADC counts. (b) The right shows the distribution of the time corresponding to the maximum signal height.

show large signal pulses in the same time window and some of them are so large that the shaper saturates. The distribution of the maximum ADC counts of the SiPMs in the camera view of figure 4.10 (a) reveals that the whole left side of the camera is illuminated with a bright core in the center of the camera. Since figure 4.10 (b) shows that this side of the camera features less pixel to pixel time fluctuations compared to the dark right side of the camera, this event might also have been generated by an air shower. Nevertheless both figures feature that also the blind pixels contribute

with pulses of several hundred ADC count heights that are correlated in time with the other signal pixels. Therewith crosstalk between the SiPM channels seems to affect the performance of the system, which has to be investigated in more detail.

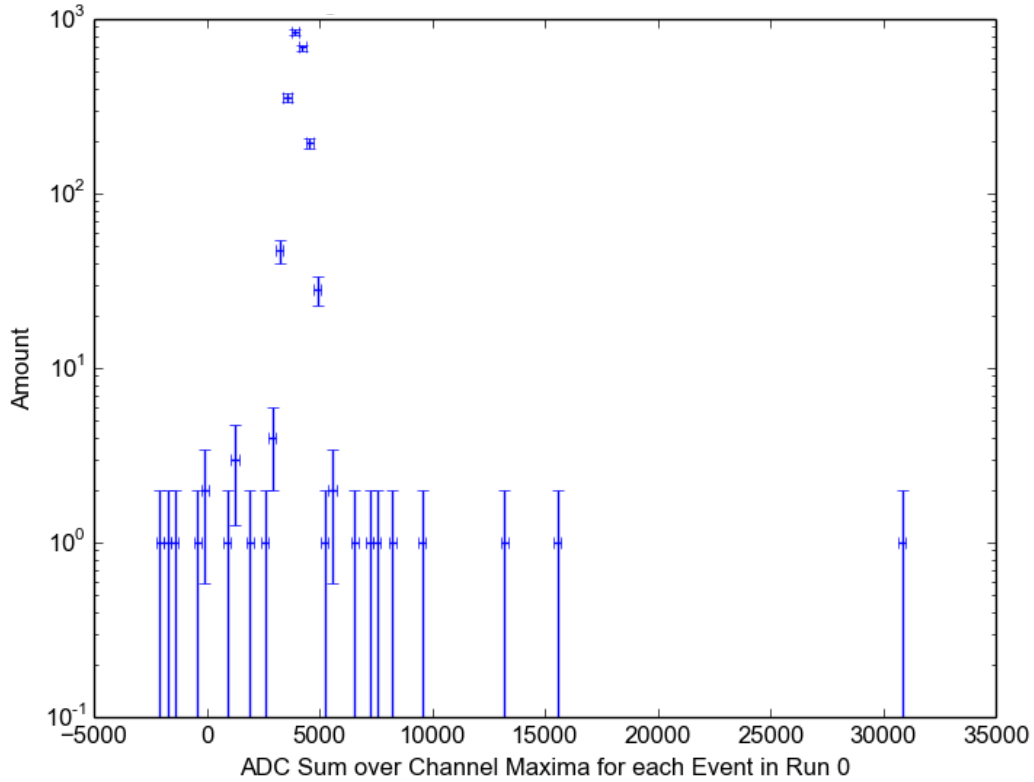


Figure 4.11: Histogram of summed up event signal height. The maximum ADC count of all SiPMs is summed up and the resulting event signal height in ADC counts is histogrammed.

In order to gain information on the fluctuations and the size of all events recorded in run 0, the maximum ADC counts after the baseline shift and within the time window between 120 ns and 160 ns of each SiPM are summed up for each event. These summed up event signal heights are shown in the histogram in figure 4.11. The peak at about 4000 ADC counts arises from the night sky background light and from noise effects, while the events above 5000 ADC counts are the 11 events that were previously found to be possibly caused by air showers. If the baseline was calibrated and there was enough statistics, a power law fit to these bright events would provide the information whether the events originate from air showers, since the energy of the primary particle is proportional to the amount of particles generated in the air shower, which is again proportional to the amount of Cherenkov light produced and therewith to the height of the SiPM pulses. For cosmic ray induced air showers a spectral index of $\gamma \approx -2.7$ as described in section 2.1 is expected for the energy range of the IceAct prototype. The plateau on the left of the peak in the histogram of figure 4.11 arises from the absence of a dedicated baseline calibration. This can be understood with figure 4.12 where the waveforms of event 1779 are plotted. The step in the baseline at about 120 ns corresponds to the first block of the storage array

of the TARGET 7 ASIC. The baselines of TARGET 7 ASICs feature a shallow rise from the second block over the in total 512 blocks up to the first block, resulting in a step after the first block. The spikes in the blocks to the right of the step in figure 4.12 are probably also inherent to the ASIC and also observed by other working groups utilizing other TARGET 7 modules but not studied in detail yet [65]. These effects as well as the spikes occurring every 32nd sample, so once per storage array block, can be resolved by a dedicated baseline calibration. Since the step is about 100 ADC counts high the worst case effect on the histogram entries in figure 4.11 equals the product of the 64 SiPMs times the step height so 6400 ADC counts. Nevertheless a qualitative summary can be drawn from this analysis. The TARGET 7 module was successfully deployed in the IceAct prototype triggering on the signals of the 64 SiPMs of the camera without requiring an external trigger. A single 10 minute run already provided bright events that are probably induced by air showers with a rate of above 1 per minute. Further automation of the telescope operation with the TARGET 7 module as well as baseline calibrations are ongoing.

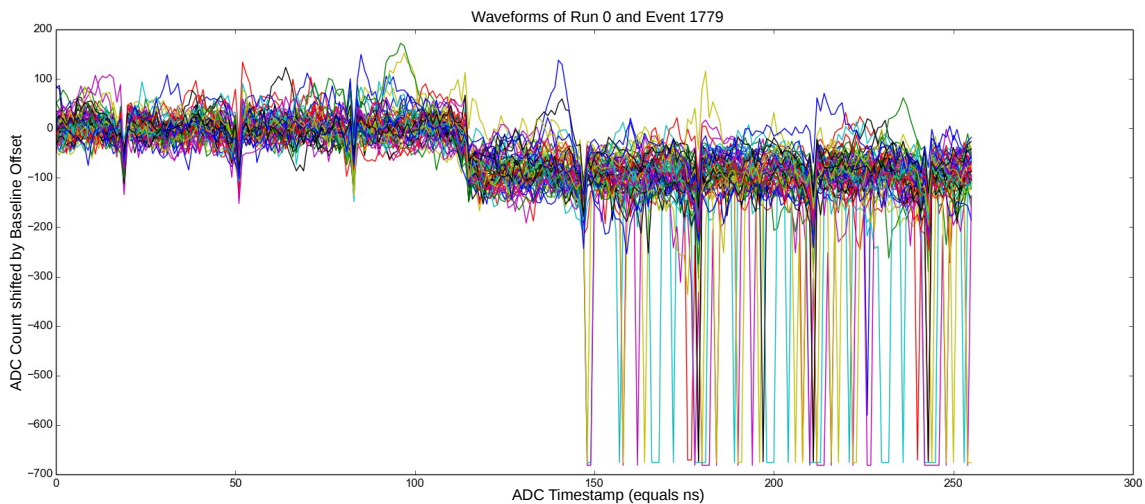


Figure 4.12: Waveforms of event 1779 with baseline step.

Apart from the TARGET 7 DAQ deployed in the IceAct prototype, a DAQ based on the 9 channel Domino Ring Sampler (DRS 4) chip used by the FACT collaboration [67] is deployed in the FAMOUS telescope that was brought to the HAWC gamma ray observatory in order to carry out field tests. The DRS4 based DAQ was successfully operated recording events coincident with HAWC, thus substantiating the prospect of compact air Cherenkov telescopes serving as an enhancement of ground based air shower detectors [25] [48]. Moreover the DRS 4 DAQ can be operated remotely, which is not yet implemented for the TARGET 7 DAQ. On top of that the TARGET 7 DAQ has issues due to the crosstalk between sampling and trigger paths. Nonetheless the TARGET 7 DAQ has advantages as cheapness, compactness, smaller trigger groups, a larger sampling buffer of about $16 \mu\text{s}$ and the possibility to operate as temperature compensating power supply with 16 channels for the in total 64 SiPMs. Especially the successor model of the TARGET 7 module, which deploys two separate ASICs, TARGET C and T5TEA, might be an alternative DAQ for future IceAct telescopes, since it solves the crosstalk issues.

5. Development of Light-Collecting Cones for the IceAct Camera

Since the former Circular Al cone, which is installed in the previous IceAct and FAMOUS prototypes as the one that was operated in Erlangen (see chapter 4), is not yet optimized for the 61-pixel camera layout, this chapter presents the development of new light-collecting cones. The installation of light-collecting cones focussing the light on SiPMs instead of just filling the whole focal plane with SiPMs is reasoned by higher costs and the shielding from stray light. In the case of the IceAct telescope stray light is already reduced by the carbon tube between Fresnel lens and camera, as the tube shields the most light outside of the field of view. Nevertheless only installing SiPMs would be more expensive especially if each SiPM was read out separately increasing the costs of a multichannel DAQ significantly. Feeding several SiPMs into one DAQ channel is disadvantageous, as the dark noise increases with the active detection area. The objective is the development of a light-collecting cone that increases the photon detection efficiency of the IceAct telescope significantly, which lowers the energy threshold in the detection of air showers via Cherenkov light. Moreover the coupling between the light-collecting cones and the SiPMs is optimized taking the extremely low temperatures at South Pole into account. During the development of improved light-collecting cones several requirements introduced in the following section are taken into account.

5.1 Requirements on the Light-Collecting Cones

To study the requirements on the light-collecting cones, figure 5.1 shows a schematic of the camera of the 61-pixel IceAct telescope. The cones, whose entrance windows are situated on a hexagonal grid in the focal plane at $f = 502.1$ mm distance to the Fresnel lens of $D = 549.7$ mm diameter, need to collect and transmit all light coming from the Fresnel lens within the maximum field of view of $2\Omega \approx 13.6^\circ$ calculated in section 3.3.1. For the central cone located in the center of the hexagonal focal plane this leads to a maximum incidence angle of:

$$\gamma = \arctan\left(\frac{D/2}{f}\right) \approx 28.7^\circ . \quad (5.1)$$

But this is not the maximum angle of incidence for all the cones, which is defined

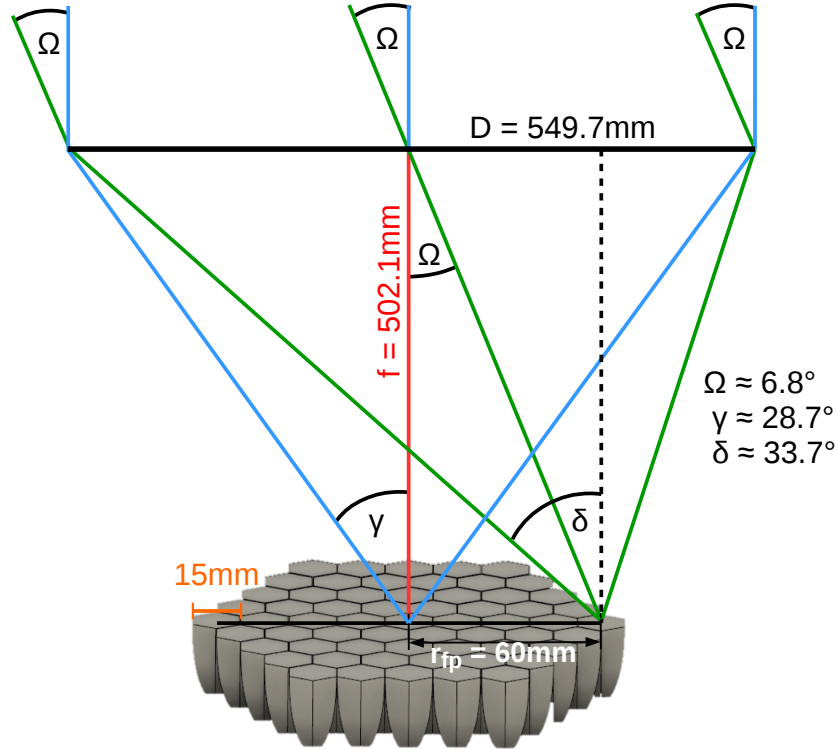


Figure 5.1: Camera layout yielding requirements on light-collecting cones. On top of the schematic there is the Fresnel lens with diameter $D = 549.7\text{mm}$ and focal length $f = 502.1\text{mm}$ focussing the light on the entrance windows of the light-collecting cones. The maximum incidence angle of photons reaching the central cone from the Fresnel lens equals $\gamma \approx 28.7^\circ$, while the cone in the edge of the hexagonal focal plane is reached by photons of $\delta \approx 33.7^\circ$ incidence angle, which hit the Fresnel lens under the maximum angle of view of $\Omega \approx 6.8^\circ$.

by the edge cones located in the edges of the hexagonal focal plane. These edge cones need to collect light up to an incidence angle of:

$$\delta = \arctan\left(\frac{D/2 + r_{fp}}{f}\right) \approx 33.7^\circ. \quad (5.2)$$

Consequently the first requirement on the light-collecting cone is a high detection efficiency in the interplay with the SiPM within the field of view of the telescope and thus for incidence angles of up to $\delta \approx 33.7^\circ$. Moreover this high detection efficiency is especially required in the deep blue and UV range, since this is the spectral range within which most Cherenkov photons reach the telescope. Another requirement is the achievement of a large fill factor in the focal plane by the entrance windows of the cones. As the focal plane consists of a hexagonal grid, a hexagonal entrance window is worth striving for. Furthermore not the cones themselves but the SiPMs detect the photons, which yields the requirement that the SiPM has to be illuminated homogeneously, because hotspots on the SiPM might affect the dynamic range of the photon detection. Therefore a cone with a square exit window fitting to the SiPM

shape is desired. On the bottom of figure 5.1 the hexagonal focal plane consists of 61 identical cones whose design has been optimized in this thesis. The cone consists of a hexagonal entrance window, a square exit window and is based on the modelling of two Winston curves. Winston curves are used to create three-dimensional Winston cones, whose theory and applications are topic of the following section.

5.2 Theory on Winston Cones

Winston cones are a non-imaging compound parabolic concentrator (CPC) constructed from the revolution of off-axis parabolas as shown in figure 5.2. Therewith a Winston cone consists of a circular entrance and a circular exit area with radius a_{en} and a_{ex} , respectively. In order to adapt to the hexagonal grid of the focal plane and the square SiPMs, most of the investigated light-collecting cones feature entrance and exit areas with edges. Though many of these cones are constructed with Winston curves, the cones are only an approximation of the "ideal" circular Winston cone presented in this section.

Each light ray impinging on the entrance area of the Winston cone under incidence angles up to the acceptance angle ϑ_M is transmitted to the exit area, while each light ray with an incidence angle above ϑ_M is reflected back and does not reach the exit area. This distinctive property of Winston cones is valuable for the suppression of stray light. Moreover Winston cones feature a concentration ratio between entrance area $A_{en} = \pi a_{en}^2$ and exit area $A_{ex} = \pi a_{ex}^2$, which is equal to the maximum possible value calculated in theory of [68]:

$$\frac{A_{en}}{A_{ex}} = \frac{n^2}{\sin(\vartheta_M)^2}, \quad (5.3)$$

where n represents the refractive index of the medium, which the cone consists of. Thus Winston cones are perfect candidates for the light-collecting cones of the IceAct prototype, as they provide the largest possible acceptance angle ϑ_M , which optimizes the requirement of collecting and transmitting all the light coming from the Fresnel lens within the field of view. The off-axis parabola forming the Winston cone by revolving around the CPC axis drawn in figure 5.2 is defined by the symmetry around the CPC axis and by demanding that rays impinging under the acceptance angle ϑ_M are focussed on the edge point of the exit window. Thus the off-axis parabola, called Winston curve in the following, is parametrized by [68]:

$$x = \frac{2a_{ex}(1 + \sin(\vartheta_M)) \sin(\phi - \vartheta_M)}{1 - \cos(\phi)} - a_{ex}, \quad (5.4)$$

$$y = \frac{2a_{ex}(1 + \sin(\vartheta_M)) \cos(\phi - \vartheta_M)}{1 - \cos(\phi)}, \quad (5.5)$$

where x is the cone radius, y the cone length and ϕ the angle between the parabola axis of one parabola and a point on the opposite parabola as sketched in figure 5.2.

The angle ϕ runs from $2\vartheta_M$ to $90^\circ + \vartheta_M$. The length of the Winston cone L with an entrance window radius a_{en} and an exit window radius a_{ex} is given by [68]:

$$L = \frac{a_{ex}(1 + \sin(\vartheta_M)) \cos(\vartheta_M)}{\sin^2(\vartheta_M)} \sim \frac{2a_{en}}{2\vartheta_M}, \quad (5.6)$$

which yields that the length enlarges for larger entrance window radii a_{en} and shortens for larger acceptance angles ϑ_M . Equation 5.6 can be rewritten using the following equation, which is the 2D equivalent to the concentration ratio equation 5.3, where the refractive index is set to $n = 1$ [68]:

$$a_{en} = \frac{a_{ex}}{\sin(\vartheta_M)}, \quad (5.7)$$

which yields [68]:

$$L = \frac{a_{en} + a_{ex}}{\tan(\vartheta_M)}. \quad (5.8)$$

In summary the acceptance angle is fixed by equation 5.7 when the window radii a_{en} and a_{ex} are given, such that the parabola describing the Winston cone can be calculated via the parametrizations 5.4 and 5.5 resulting in a cone length given by equation 5.8.

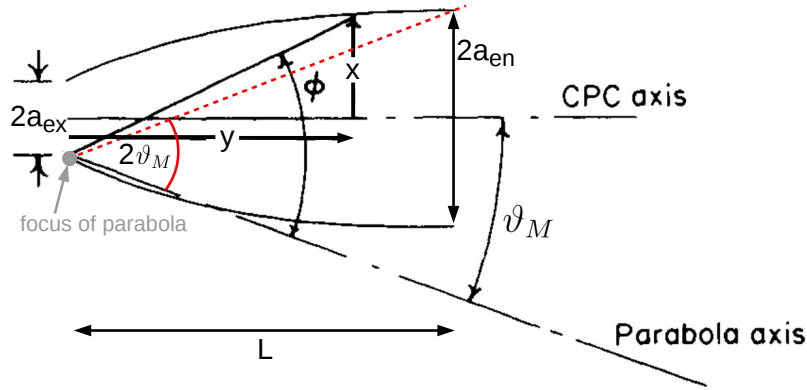


Figure 5.2: 2D view of Winston cone. Sketched are two off-axis parabolas with focus points on the opposite edge of the exit window of diameter $2a_{ex}$ on the left of the figure. Angle ϕ , cone radius x and cone length y are parameters used to parametrize the off-axis parabolas, which form a Winston cone of length L and acceptance angle ϑ_M by a rotation around the CPC axis. Taken from [68].

A Winston cone can be built from a reflective material or from a refractive material using internal total reflection. In case of a hollow reflective Winston cone the Winston curves consist for example of aluminum while the medium of the Winston cone is air with a refractive index of approximately $n = 1$. On the other hand a solid refractive Winston cone consists of a medium with a refractive index $n > 1$ such that the acceptance angle of the refractive Winston cone ϑ_M^n equals the refracted acceptance angle of the reflective Winston cone ϑ_M following Snell's law:

$$\vartheta_M^n = \arcsin \left(\sin(\vartheta_M) \cdot n \right) > \vartheta_M. \quad (5.9)$$

Due to this refraction at the entrance window, Winston cones using refractive materials with $n > 1$ reach larger concentration ratios and acceptance angles than reflective cones with the same entrance and exit window radius, which is also given by equation 5.3. This positive effect of refractive materials is used in the development of new optimized light-collecting cones, which are presented in the following section.

5.3 Design of Investigated Cone Models

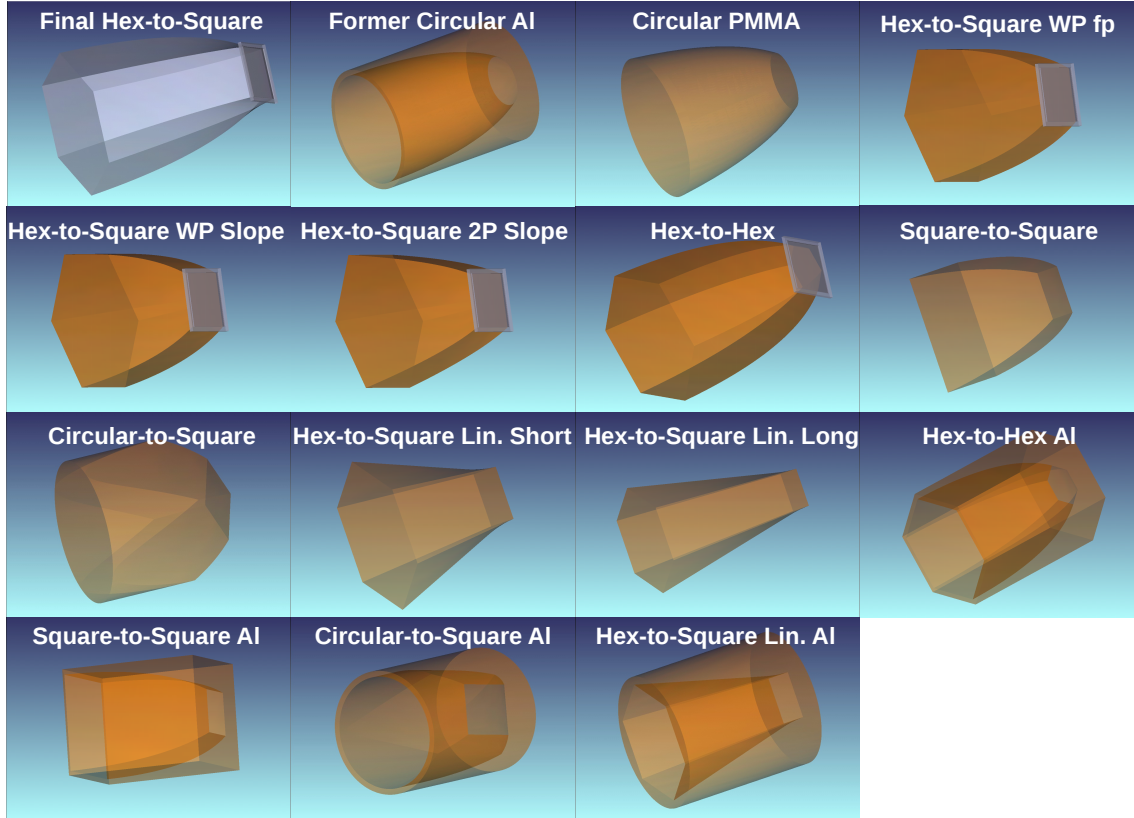


Figure 5.3: Compilation of investigated cones. The first cone, going from top to bottom and left to right, shows the final Hex-to-Square cone, which emerges as the best cone for the application in IceAct from the simulations in section 5.4. Second and third cone are the currently installed former Circular Al cone and its follow-up Circular PMMA cone made from the refractive material PMMA. The following cones are part of the continuous improvement of the cone design. If *Al* is not in the label of the cone, the cone is not made from aluminum, but from PMMA. An SiPM is shown at the exit window of 5 cones. Characteristics of the cones are given in table 5.1 on page 46, where also the notations are explained.

The cones were designed with the Autodesk Inventor computer-aided design software [69]. Figure 5.3 gives an overview on all the investigated cones, while the notation is introduced in table 5.1, where the characteristics of each investigated cone are given. In the following the design of the different cone types is explained in detail.

Cone model	L [mm]	a_{en} [mm]	a_{ex} [mm]	ϑ_M or $\vartheta_M^n(\vartheta_M)$ (value after refraction)	Optimized curves W = Winston; P = Parabola
Final Hex-to-Square	23.5	7.4	3	37.2°(23.9°)/30.6° (20°)	Side: W / Edge: cut W
Former Circular Al	19.4	6.71	3	26.56°	W
Circular PMMA	14.7	7.4	3	33.7°(21.9°)	cut W
Hex-to-Square WP fp	14.7	7.4	3	33.7°(21.9°)/not def.	Side: cut W / Edge: upright P
Hex-to-Square WP Slope	14.7	7.4	3	33.7°(21.9°)/not def.	Side: cut W / Edge: upright P
Hex-to-Square 2P Slope	14.7	7.4	3	not def./not def.	Side: upright P / Edge: upright P
Hex-to-Hex	24.4	7.4	2.6	31.5°(20.5°)	Sides: W
Square-to-Square	14.7	7.4	3	33.7°(21.9°)	Sides: cut W
Circular-to-Square	14.7	7.4	3	33.7°(21.9°)	Upper cone cut by cylinder
Hex-to-Square Lin. Short	14.7	7.4	3	not def.	Lin. interpol. between windows
Hex-to-Square Lin. Long	26.8	7.4	3	not def.	Lin. interpol. between windows
Hex-to-Hex Al	22.2	6.71	2.6	22.78°	Sides: W
Square-to-Square Al	19.4	6.71	3	26.56°	Sides: W
Circular-to-Square Al	19.4	6.71	3	26.56°	Upper cone cut by cylinder
Hex-to-Square Lin. Al	19.4	6.71	3	not def.	Lin. interpol. between windows

Table 5.1: Characteristics of investigated cones. The naming x -to- y of the cones implies that the entrance window of the cone has the shape x while the exit window has the shape y . If there is only one shape given, both windows have the same shape. Listed are length L , radius of the entrance and exit window a_{en} and a_{ex} respectively (in case of non-circular windows, the half distance between opposite window sides is given), acceptance angle ϑ_M (in case of PMMA cones, the acceptance angles before ϑ_M^n and after refraction (ϑ_M)) are given) and the type of the optimized curves forming the 3D cone. If the cone model is not denoted with *Al*, the cone model is made of PMMA; the corresponding acceptance angle used for the design of the Winston curves is the one given in brackets, which translates into the non-bracketed value ϑ_M^n due to refraction at the entrance window following Snell’s Law. *cut W* signifies that the Winston curve is truncated to the given length L to achieve the given radius of the entrance window a_{en} . In case of the Hex-to-Square cones the notation *side/edge* relates to the *blue/green* curves in figure 5.4 (a). Hex-to-Square cones designed with parabolas are marked with *Slope*, if the parabola is determined by optimizing its slope at the edge of the exit window as shown in figure 5.4 (b), or *fp*, if the parabola is determined by setting its focal point into the plane of the exit window.

Circular cones - ”ideal” Winston cones

These Winston cones are investigated, as they provide the maximum possible concentration ratio needed to collect the light from the Fresnel lens. Currently the camera of the IceAct prototype has former Circular Al cones installed. As already shown in figure 3.6 on page 21, the maximum diameter of circular cones is fixed by the spacing of the hexagonal grid on the SiPM PCB of 15 mm. The diameter of the entrance window of aluminum cones is furthermore limited by a finite wall thickness, which equals 0.79 mm, resulting in a radius of the entrance window of

$a_{en} = 6.71$ mm. The radius of the exit window equals $a_{ex} = 3$ mm, since it is given by the size of the 6×6 mm² SiPMs. Therewith the maximum possible acceptance angle of the former Circular Al cone can be calculated from a_{en} and a_{ex} via equation 5.7 yielding $\vartheta_M = 26.56^\circ$. Recalling the maximum incidence angle $\delta = 33.7^\circ$ in equation 5.2 required to be accepted by the cones to collect the light coming from the Fresnel lens, it is obvious that the former Circular Al cone cannot meet the requirements. Moreover the fill factor in the focal plane is worsened by both the circular shape and the wall thickness of the former Circular Al cone.

Therefore a follow-up cone is designed from PMMA, as PMMA has a refractive index $n = 1.49$ at a photon wavelength of $\lambda = 546$ nm [26], which provides a maximum possible ϑ_M^n of 37.2° as given by equation 5.9, which is larger than required for the IceAct telescope. In the following the conservative approximation $n = 1.49$ is used for the parametrization of the Winston curves, as the refractive index n of PMMA rises towards the UV region [26], such that the acceptance angles are even larger in the UV range. In principle a radius of the entrance window $a_{en} = 7.5$ mm is possible for PMMA cones, which then would touch each other on the focal plane resulting in a maximum fill factor. Nevertheless all the PMMA cones are designed with $a_{en} = 7.4$ mm, because otherwise tensions caused by temperature variations might damage the touching cones. Thus a *Circular PMMA* cone with $\vartheta_M = 21.9^\circ$ and $a_{ex} = 3$ mm is parametrized by the equations 5.4 and 5.5 yielding a Winston curve with acceptance angle $\vartheta_M^n = \delta = 33.7^\circ$ and $a_{en} > 7.4$ mm. As a_{en} is larger than desired, the Winston curve is truncated such that a_{en} equals 7.4 mm resulting in a cone length of $L = 14.7$ mm. These two cones are shown as second and third screenshot in figure 5.3.

Square-to-Square, Circular-to-Square and Hex-to-Hex cones

The four side surfaces of the *Square-to-Square* cones are obtained by extruding the Winston curve defining the respective circular cone. This cone is investigated, since the exit window covers the whole SiPM. Nevertheless this cone would require a redesign of the SiPM PCB, as the square entrance windows do not fit into the hexagonal grid of the current SiPM PCB. Therefore the *Circular-to-Square* cones are designed matching the hexagonal grid with their circular entrance window and covering the whole SiPM with their square exit window. The Circular-to-Square cones originate from the corresponding Square-to-Square cone by cutting the edges of the entrance window with a cylinder of length L and radius a_{en} . The *Hex-to-Hex* cones are of interest as their hexagonal entrance windows maximize the fill factor in the focal plane. The six side surfaces of these cones are also designed by an extrusion of a Winston curve. But here the Winston curve is calculated anew due to the smaller radius of the exit window a_{ex} , which reduces the achievable maximum acceptance angle ϑ_M .

Hex-to-Square Lin. cones

The side surfaces of the *Hex-to-Square Lin.* cones are designed by a linear interpolation between the hexagonal entrance window and the square exit window such that every cone surface is described by straight lines. The length of these cones is adapted to the length of the previously discussed cones. Because this cone does

not require the design of complex non-linear curves, though yielding the maximum possible fill factor in the focal plane and covering the whole SiPM, this is the first try of a Hex-to-Square cone model.

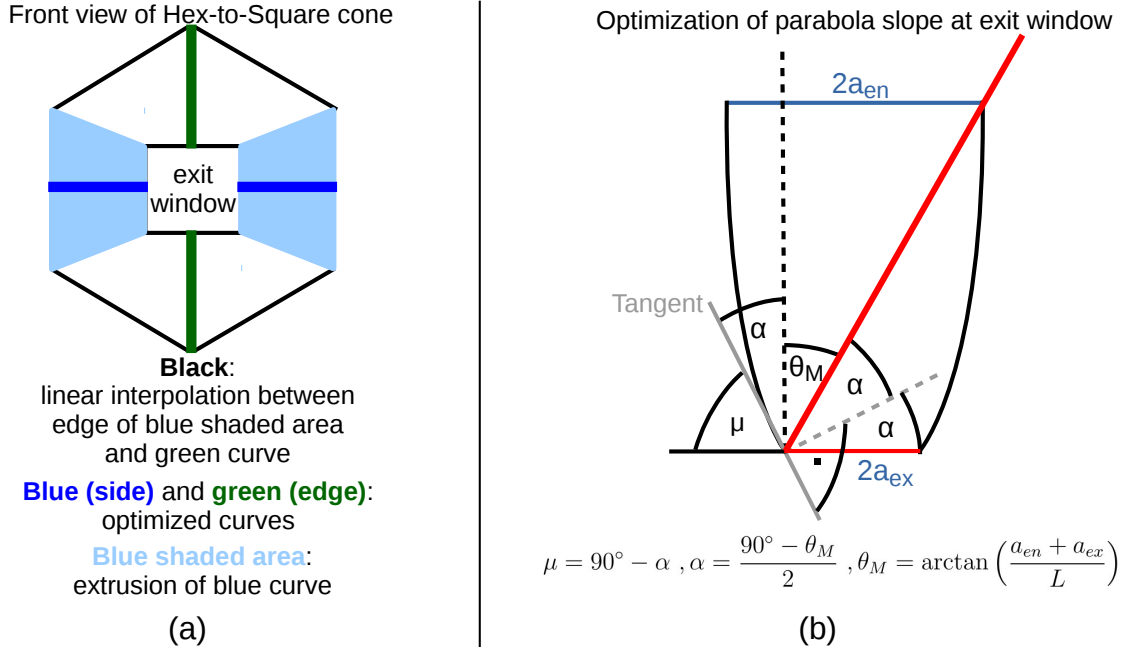


Figure 5.4: Layout of Hex-to-Square cones and sketch of parabola optimization. (a) Shows a front view of a Hex-to-Square cone. The blue and green lines mark optimized non-linear curves. The curves marked blue are extruded and form the two blue shaded opposing surfaces of the cone. Black marked linear interpolations between the green curves and the edges of the blue shaded surfaces form the other four surfaces of the cone. (b) Sketches the cross-section of an upright parabolic cone, whose parabola is optimized to reflect the red ray in parallel to the exit window, where the red ray impinges on the exit window edge under the maximum possible incidence angle θ_M . The optimization fixes the slope of the parabola at the exit window edge to the corresponding angle μ .

Figure 5.4 (a) sketches the layout of Hex-to-Square cone models that are designed with two optimized non-linear curves that are marked blue and green. The blue curves are located on opposite sides of the cone and run from the middle of a side of the hexagonal entrance window to the middle of the parallel side of the square exit window. In the front view of the cone the green curves are perpendicular to the blue curves. The green curves are also located on opposite sides of the cone and run from an edge of the hexagonal entrance window to the middle of a side of the square exit window. The curves marked blue are extruded and form the two blue shaded opposing surfaces of the cone. Black marked linear interpolations between the green curves and the edges of the blue shaded surfaces form the other four surfaces of the cone.

Upright parabolic Hex-to-Square cones - WP fp, WP Slope and 2P Slope
Inspired by the PMMA light concentrators developed by the FACT collaboration,

which also feature the Hex-to-Square design and which are designed from upright parabolas [70] instead of more complex Winston curves, three Hex-to-Square cones were at least partly designed with upright parabolas.

In case of the *Hex-to-Square WP fp* cone the blue curves are parametrized by the Winston curve of the Circular PMMA cone, while the green curve is given by an upright parabola that is meant to be an approximation of a more complex Winston curve. The general equation describing an upright parabola is given by:

$$\begin{aligned} f(x) &= bx^2 + cx + d \\ &= b\left(x + \frac{c}{2b}\right)^2 + \frac{4bd - c^2}{4b} \\ &= \frac{1}{4f}(x - x_0)^2 + y_0 , \end{aligned}$$

where f equals the focal length of the parabola, which is given by the distance between focal point and vertex of the parabola at (x_0, y_0) . The parabola of the Hex-to-Square WP fp cone is optimized to have its focal point within the plane of the exit window leading to a fixed $y_0 = -f$. This is motivated by the location of the focal point of Winston curves that is located at the opposite edge of the exit window and thus also in the plane of the exit window. As the parabola has to cross the edges of both entrance and exit window and since the height of the cone is given by the length of the Winston curve $L = 14.7$ mm, the parabola has to cross the points $(a_{ex}, 0$ mm) and $(a_{en}, 14.7$ mm), where $a_{ex} = 3$ mm and $a_{en} = 2 \cdot 7.4/\sqrt{3}$ mm. Therewith the upright parabola of the Hex-to-Square WP fp cone is defined by:

$$f(x) = 0.30 \cdot (x - 1.33)^2 - 0.84 . \quad (5.10)$$

In case of the *Hex-to-Square WP Slope* cone the blue curves are also parametrized by the Winston curve of the Circular PMMA cone, while the green curve is given by an upright parabola that is meant to approximate a more complex Winston curve in another way. Here the upright parabola is defined via the slope at the edge of the exit window as shown in figure 5.4 (b). Analog to a Winston curve, the upright parabola reflects the ray, impinging on the exit window edge under the maximum possible incidence angle θ_M , in parallel to the exit window. Equivalent to the parabola of the previously treated cone, the parabola of this cone has to cross the points $(a_{ex}, 0$ mm) and $(a_{en}, 14.7$ mm), where $a_{ex} = 3$ mm and $a_{en} = 2 \cdot 7.4/\sqrt{3}$ mm. Moreover the slope of the parabola is defined as shown in figure 5.4 (b):

$$\left. \frac{d}{dx} f(x) \right|_{x=a_{en}} = \tan(\mu) . \quad (5.11)$$

Therewith the parameters of the parabola are well defined with the following system of equations:

$$\begin{aligned} L &= b \cdot a_{en}^2 + c \cdot a_{en} + d \\ 0 &= b \cdot a_{ex}^2 + c \cdot a_{ex} + d \\ \tan\left(90^\circ - \frac{90^\circ - \arctan\left(\frac{a_{en} + a_{ex}}{L}\right)}{2}\right) &= 2b \cdot a_{ex} + c , \end{aligned}$$

resulting in the upright parabola of the Hex-to-Square WP Slope cone:

$$f(x) = 0.11 \cdot x^2 + 1.42 \cdot x - 5.21 . \quad (5.12)$$

In case of the last of these three Hex-to-Square cones based on parabolas, the *Hex-to-Square 2P Slope* cone, the blue curves are parametrized by an upright parabola, whose slope at the edge of the exit window is equivalently optimized as in case of the previous cone, while the green curve is also given by equation 5.12. The only difference between the two parabolas is the radius of the entrance window of the blue colored parabola of $a_{en} = 7.4$ mm, as this parabola ends in a side of the hexagonal entrance window and not in an edge. Therewith the upright parabola colored green in figure 5.4 (a) is given by equation 5.12 for the Hex-to-Square 2P Slope cone, while the other upright parabola colored blue is given by:

$$f(x) = 0.32 \cdot x^2 + 0.02 \cdot x - 2.94 . \quad (5.13)$$

All these upright parabolas are plotted in figure 5.6, where also the Winston curves of the final Hex-to-Square cone are included for comparison.

5.3.1 The Final Hex-to-Square Cone

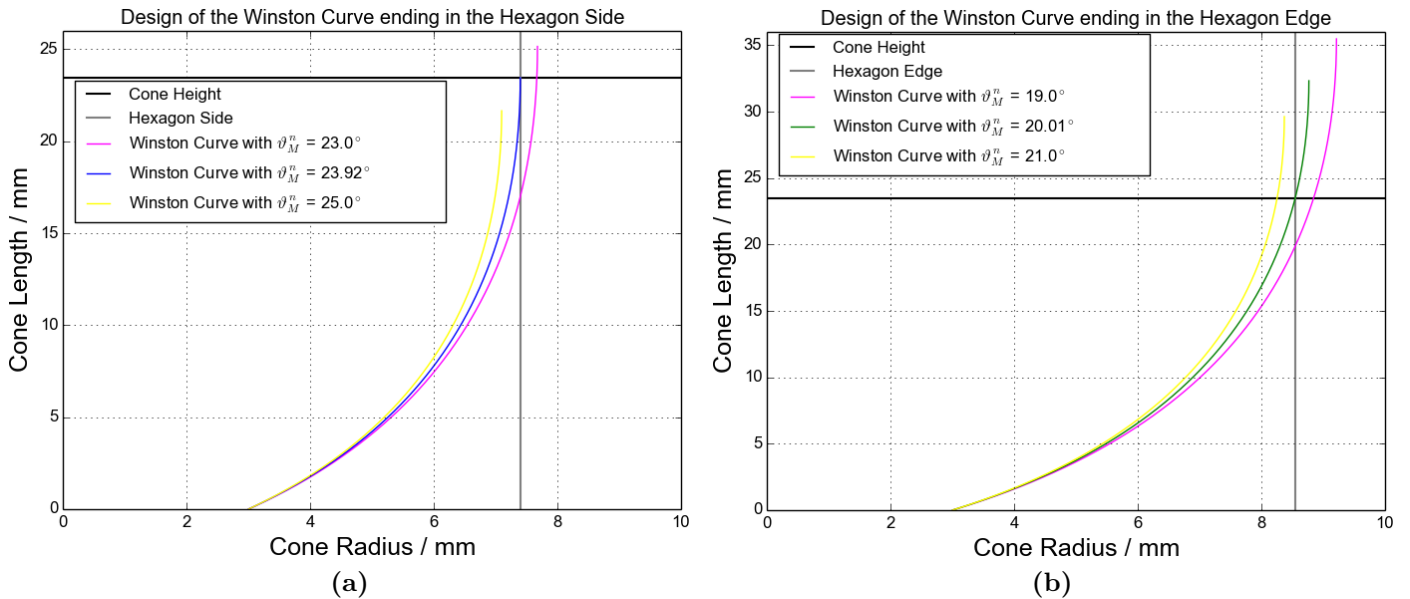


Figure 5.5: Development of Winston curves for final Hex-to-Square cone. (a) The Winston curve ending at the hexagon edge of the final Hex-to-Square cone is plotted in blue (equal to the blue lines in figure 5.4 (a)). (b) The Winston curve crossing the hexagon edge of the final Hex-to-Square cone is plotted in green (equal to the green lines in figure 5.4 (a)).

The *final Hex-to-Square* cone is designed equivalently to the cones presented at the end of the last section as shown in figure 5.4 (a), but in this case both curves are optimized, so the blue curve ending at the hexagon side as well as the green

curve ending at the hexagon edge, are parametrized by Winston curves. Since the maximum possible acceptance angle of the Winston curve with the smaller radius of the entrance window, thus the blue Winston curve ending at the hexagon side, is, with $\vartheta_M^n = 37.2^\circ$, larger than the one of the green Winston curve ending at the hexagon edge of $\vartheta_M^n = 31.5^\circ$, the former Winston curve is fixed in the first step setting the length of the final Hex-to-Square cone of $L = 23.5$ mm via equation 5.8. The acceptance angles have been calculated from the given radii of entrance and exit window via equation 5.7, whose result was inserted in equation 5.9 to account for the gain caused by the refraction in PMMA. The Winston curve ending at the hexagon side of the final Hex-to-Square cone is plotted blue colored in figure 5.5 (a).

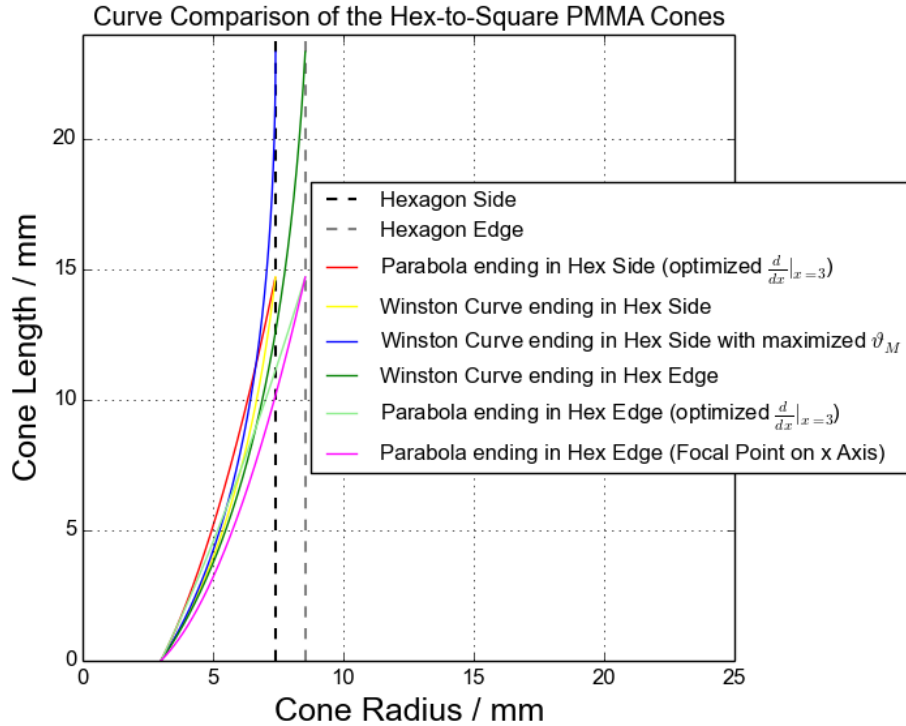


Figure 5.6: Comparison of the Hex-to-Square cone curves. The two long curves are the Winston curves of the *final Hex-to-Square* cone, where the colors, blue and green, fit to figure 5.4 (a). The *Hex-to-Square WP Slope* and *Hex-to-Square WP fp* cones are both designed with the yellow Winston curve and the turquoise and magenta upright parabolas, respectively. The *Hex-to-Square 2P Slope* cone is designed with the red and the magenta upright parabolas. Moreover the yellow Winston curve forms the *Circular PMMA* cone via a rotation around the y-axis.

The Winston curve ending at the hexagon edge plotted green colored in figure 5.5 (b) is found by varying the acceptance angle such that the curve crosses the hexagon edge at $a_{en} = 2 \cdot 7.4 / \sqrt{3}$ mm after the length of the final Hex-to-Square cone $L = 23.5$ mm, which is already defined by the Winston curve ending at the hexagon side. At this crossing point the Winston curve is truncated. Because of the constraints originating from the desired cone geometry, the acceptance angle of the Winston curve ending at the hexagon edge is limited to $\vartheta_M = 20.01^\circ$, which translates into $\vartheta_M^n = 30.6^\circ$. Nevertheless this is close to the maximum possible value of 31.5° and sufficient for

the central cones of the IceAct camera to collect all the light coming from the Fresnel lens at maximum under incidence angles of $\gamma = 28.7^\circ$.

Figure 5.6 gives an overview on the different Hex-to-Square cones discussed in detail previously. As Winston curves give the largest possible concentration ratio required to collect the light from the whole Fresnel lens and since a hexagonal entrance window provides the largest possible fill factor in the focal plane while a square exit window covers the whole SiPM, the final Hex-to-Square cone is the minion in the simulations of the following sections, which target to identify the cone that fits best for the application in IceAct.

5.4 Zemax Simulations for the Cone Development

Now that all investigated light-collecting cones are introduced, the cone has to be identified, which fits best to the requirements given by the application in the IceAct telescope. This cone optimizes the light detection efficiency of the combined cone and SiPM system as illuminated in the telescope. Since a measurement under the correct illumination is currently not feasible, a versatile simulation chain is developed and verified against an available measurement setup. If the corresponding simulation can reproduce the laboratory measurements, the other simulations can be used to extract the in-system efficiency of the cone. First, in section 5.4.1, the simulation determining the in-system efficiency of the investigated cones is presented to be able to rule out the new cones with inferior performance. Subsequently the illumination of the SiPM (section 5.4.2) and the angular acceptance of the cone and SiPM system (section 5.4.3) is simulated for the cones performing best in the first simulation and for the former Circular Al cone. Afterwards the simulation of the measurement setup (section 5.4.4) is presented, which consists of a small beam that scans the respective cone by sliding the beam or rotating the cone. In section 5.5 the corresponding measurement is compared to this simulation.

The simulations are carried out with the Zemax OpticStudio software [71]. The cone models designed in Autodesk Inventor [69] can be imported as *.stp*-files and other objects like an SiPM, which is connected to the cone in the camera of IceAct, can be build in Zemax using predefined materials. The objects are illuminated by light sources of selectable wavelengths that can be placed anywhere inside or outside of the objects. Zemax simulates the light rays following the physical reality and calculates for instance the fraction of simulated photons reaching a detector. It has to be stated that all the performed simulations do not involve absorption within the materials. Nonetheless the materials have an extinction property, as a maximum number of transitions or reflections at object boundaries is defined by Zemax.

Unlike absorption, the reflectivity of light rays at the transition from a medium with refractive index n_1 to a medium with refractive index n_2 follows the scientific laws in Zemax. The reflectivity is dependent on the angle of incidence α_i and the polarization of the light relative to the plane of incidence such that for perpendicularly and parallel polarized light, respectively, it is given by the Fresnel-equations [72]:

$$R_s = \left(\frac{n_1 \cos(\alpha_i) - n_2 \cos(\alpha_r)}{n_1 \cos(\alpha_i) + n_2 \cos(\alpha_r)} \right)^2, \quad R_p = \left(\frac{n_2 \cos(\alpha_i) - n_1 \cos(\alpha_r)}{n_2 \cos(\alpha_i) + n_1 \cos(\alpha_r)} \right)^2, \quad (5.14)$$

where α_r denotes the refracted angle of incidence inside of the second medium with refractive index n_2 , given via Snell's law:

$$\alpha_r = \frac{n_1}{n_2} \sin(\alpha_i) . \quad (5.15)$$

The light is unpolarized in the case of IceAct and the simulations carried out in this thesis, which yields a total reflection fraction of:

$$R = \frac{1}{2}(R_s + R_p) , \quad (5.16)$$

which is plotted against the angle of incidence in figure 5.7. The cones made of PMMA use internal total reflection to collect the light coming from the Fresnel lens of IceAct, which is given for light rays hitting any surface between PMMA and air under angles of incidence above about 40° . Furthermore the loss due to reflection of rays vertically penetrating the entrance as well as the exit window of the cone equals about 4%, if the other medium is air. This loss is visible as the plateau of the green and blue curves on the left of figure 5.7. It has been cross-checked that this is also the case in the Zemax software.

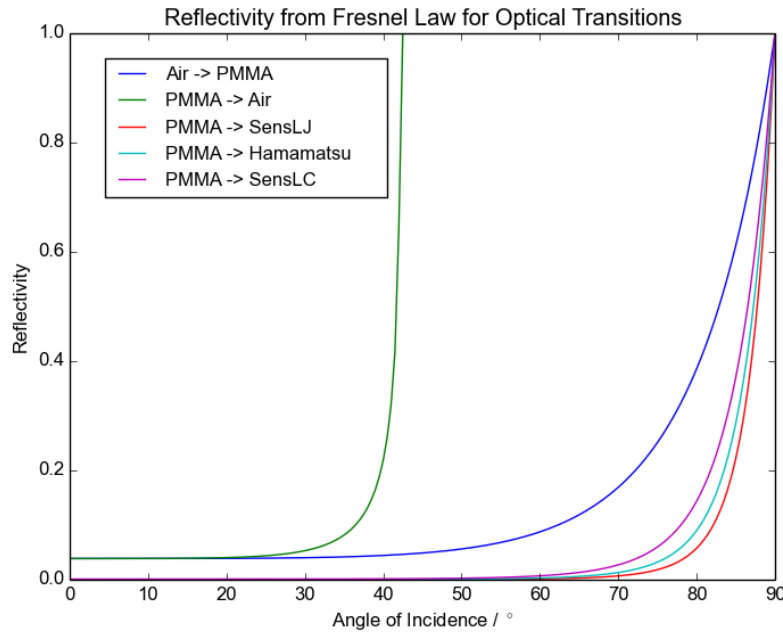


Figure 5.7: Reflectivity at optical transitions between cone and SiPM. Green and blue curve describe the reflectivity between PMMA and air. The other curves describe the reflectivity between PMMA and coating of the respective SiPM.

The other curves describe the reflectivity between the PMMA cones and the different SiPMs that are part of this thesis. The refractive indices of the SensL SiPMs is given in table 3.1 on page 26 and the one of the Hamamatsu SiPM installed in the setup of the measurements in section 5.5 is given in table 5.6 on page 72. Since the refractive index of the SensL J-Series SiPM $n_d = 1.53$ matches best to the one of

PMMA $n = 1.49$, this SiPM reflects the smallest fraction of the incident photons. This optical matching is also an advantage of the PMMA cones over the aluminum cones, where the optical transition from air directly into the SiPM coating, which is optically denser than PMMA for each considered SiPM, is harder. On top of that the surface of the aluminum cones only reflects about 92% of the incident light for the 380 nm and 532 nm wavelengths studied in this thesis [73], which is less than the 100% reflectivity achieved by the total reflection within the PMMA cones.

5.4.1 Simulation of Efficiency of Cone and SiPM in IceAct

5.4.1.1 Simulation Setup and Procedure

This Zemax simulation is meant to determine the detection efficiency of light coming from the Fresnel lens and entering the investigated cone, as sketched in figure 5.1 on page 42. Therefore the simulation consists of a point source, the investigated cone and an SiPM with a detector plane. The material of the PMMA cones is defined to be the Zemax *PMMA* material with a refractive index of $n_d = 1.49$, or, in case of an aluminum cone, the chosen Zemax material is *MIRROR*, since this material equals a thick aluminum coating with a reflectivity that is cross-checked to equal the previously mentioned 92%. The surfaces of the cones are considered to be perfect, thus omitting scattering due to surface roughness, if not stated differently. A SensL C-Series SiPM is coupled to the exit window of the investigated cone. In case of PMMA cones the coating of the SiPM touches the exit window of the cone with no air gap between the two objects. The geometry of the SiPM is adopted from the datasheet of the SensL C-Series SiPM [56]. The simulated SiPM consists of a *POLYCARB* coating with the refractive index $n_d = 1.59$, which fits to the value given in the datasheet and table 3.1, and of a *SILICON* layer with $n_d = 4.03$ inside of the coating. Inside of the silicon layer a detector plane of the same size of $6 \times 6 \text{ mm}^2$ is placed, such that the simulation accounts for the reflection losses at the surface of the silicon.

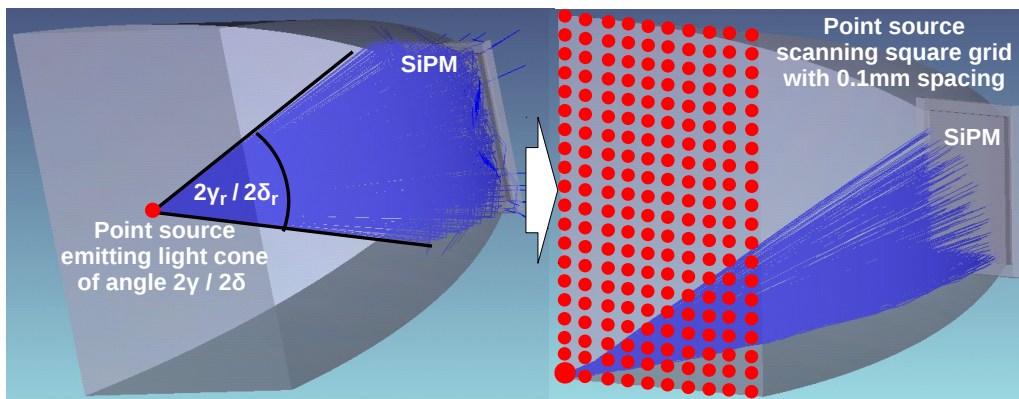


Figure 5.8: Simulation of the Cone Efficiency within the Telescope. A point source is simulated just above the entrance window of the investigated cone; the *Square-to-Square* cone in this example; which is coupled to the SensL C-Series SiPM comprising a detector plane.

The efficiency is defined as the fraction of photons that are detected by the detector plane in the SiPM, which previously penetrated the entrance window of the investigated cone. It is important to note that the efficiency of the cone and SiPM system is determined, because for the IceAct telescope the performance of the interplay of cone and SiPM has to be optimized, not the performance of the cone alone.

The two most extreme cases of the illumination within IceAct are considered. First the central cone in the center of the focal plane and the edge cone in the edge of the focal plane. These are illuminated by photons coming from the Fresnel lens under maximum angles of incidence of $\gamma = 28.7^\circ$ and $\gamma = 33.7^\circ$, respectively. γ and δ are calculated in section 5.1 by equation 5.1 and 5.2, respectively. Figure 5.8 sketches the principle of the simulation. The Fresnel lens is approximated to focus the incident light homogeneously in a circular cone of apex angle 2γ or 2δ on the entrance window of the central cone and edge cone, respectively. This approximation is sketchy for the edge cone, since this cone is not illuminated symmetrically by the Fresnel lens. Nonetheless the approximation is conservative for the determination of the detection efficiency, as a larger fraction of the simulated photons impinges the edge cone under large angles of incidence. These photons are collected less efficiently than photons of small angle of incidence, as analysed in the simulation of section 5.4.3, resulting in an underestimated detection efficiency. Since the entrance window is located in the focal plane of the Fresnel lens, a point source is simulated just above the entrance window of the investigated cone to account for reflection losses at the entrance window, as well as refraction in case of PMMA cones. The source homogeneously emits 15000 light rays within a circular light cone with an apex angle of $2\gamma = 2 \cdot 28.7^\circ$, in case of simulating the central cone, or $2\delta = 2 \cdot 33.7^\circ$, in case of simulating the edge cone. The wavelength of the point source is chosen to be $\lambda = 380$ nm, as IceAct is meant to detect atmospheric Cherenkov light peaking in the UV range. In the simulation this source scans the whole entrance window of the cone on a square grid with a resolution of 0.1 mm. The fraction of photons reaching the detector inside the SiPM's silicon layer is saved for each point source position as this is considered the efficiency of light detection for light rays crossing the entrance window at the point source position.

In order to account for the photon detection efficiency (PDE) of the SensL C-Series SiPM, a preparatory simulation is carried out, where only the SiPM is simulated and its active area is illuminated by perpendicularly impinging rays. Here the active area equals the area of the silicon and detector plane, respectively, which is shown as the dark grey part of the SiPM on the right in figure 5.8. The obtained efficiency called PDE_{SiPM}^{Zemax} can be used to correct for the PDE of the SensL C-Series SiPM $PDE_{SiPM}^{datasheet}$ at the simulated wavelength given in the datasheet [56], since $PDE_{SiPM}^{datasheet}$ is assumed to be reflection loss corrected and given for perpendicularly impinging photons. Because the simulation only considers the optical properties of the materials and does not take quantum efficiency, fill factor and trigger probability into account, PDE_{SiPM}^{Zemax} does not equal $PDE_{SiPM}^{datasheet}$. Therefore the raw efficiencies ε_0 coming from the following simulations are corrected for the PDE of the SiPM resulting in the efficiency ε :

$$\varepsilon = \frac{\varepsilon_0}{PDE_{SiPM}^{Zemax}} \cdot PDE_{SiPM}^{datasheet} . \quad (5.17)$$

Figure 5.9 shows the wavelength dependence of the PDE of each SiPM used in this thesis, especially the SensL C-Series SiPM. Moreover the simulated PDEs of each SiPM PDE_{SiPM}^{Zemax} , denoted with $Zemax$ in the legend, are included. These simulated PDEs are very similar for each SiPM, since the only difference in the simulations is the material and the thickness of the SiPM coating, where absorption inside a medium is not considered and the refractive indices of the different materials only differ within 1.53 and 1.59. The black line marks the wavelength $\lambda = 380$ nm simulated for instance in this simulation, while the grey line marks the wavelength of the laser which is used in the setup of the measurements presented in section 5.5.

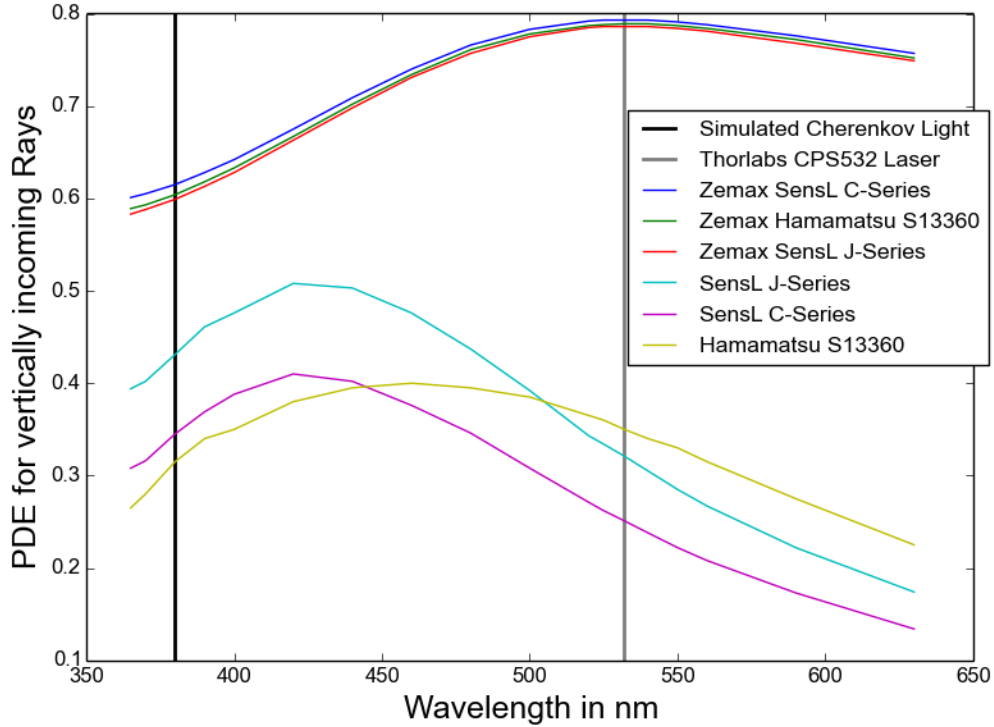


Figure 5.9: Wavelength dependence of PDE of SiPMs. The black line marks the wavelength $\lambda = 380$ nm simulated for instance in this simulation, while the grey line marks the wavelength of the laser which is used in the setup of the measurements in section 5.5. The simulated PDEs of each SiPM PDE_{SiPM}^{Zemax} , denoted with $Zemax$ in the legend, are obtained by a simulation with light rays penetrating the active area of the respective SiPM perpendicularly. The PDEs of the SiPMs are given for the typical overvoltages of 6 V, in case of the SensL J-Series SiPM, 5 V, in case of the SensL C-Series SiPM, and 1.4 V, in case of the Hamamatsu SiPM, and are taken from the datasheets [57], [56] and [74], going downwards in the legend.

The detection efficiency for light generated by a simulated point source shown in figure 5.8 is given by ε_γ , in case of simulating a central cone, and ε_δ , in case of simulating an edge cone of the focal plane, via equation 5.17 with $\varepsilon = \varepsilon_{\gamma/\delta}$ and ε_0 being the raw efficiency coming from the particular simulation.

A further detection efficiency $a_{\gamma/\delta}$ is defined to account for the fill factor achieved

by the entrance window of the investigated cone in the focal plane of IceAct. This detection efficiency considering the fill factor is given by:

$$a_{\gamma/\delta} = \varepsilon_{\gamma/\delta} \cdot \frac{A_{cone}}{2\sqrt{3} \cdot 7.5^2}, \quad (5.18)$$

where A_{cone} equals the area of the entrance window of the investigated cone and $2\sqrt{3} \cdot 7.5^2$ the area of a hexagon filling a cell of the hexagonal grid in the focal plane completely.

5.4.1.2 Analysis of Cone Efficiencies

Resulting 2D plots of the detection efficiency ε are shown in figure 5.10 (a)-(d) for the final Hex-to-Square cone and the Circular PMMA cone. The color denotes the detection efficiency ε and x- and y-axis the position of the point source on the entrance window of the cone. The colorbar is identical in each plot and covers only a small range from 31.57% to 35.56%, yielding a very homogeneous detection efficiency across the entrance surface of both investigated cones. The structure in the simulation of the final Hex-to-Square cone in figure 5.10 (a) and (b) is intrinsic to the design of the cone with two different Winston curves, as the structure does neither change when simulating a SensL J-Series SiPM instead of the C-Series SiPM nor when no SiPM is simulated and the detector plane is located directly on the exit window of the cone. Both left and right side of the hexagon, where the efficiency is largest, are defined by the Winston curve with acceptance angle $\vartheta_M = 37.2^\circ$, while the top and bottom edge of the hexagon, where the detection efficiency is also large, is defined by the Winston curve with acceptance angle $\vartheta_M = 30.6^\circ$. As expected, the detection efficiency close to the hexagon edge, where the $\vartheta_M = 30.6^\circ$ Winston curve is located, drops from 5.10 (a) to (b), since the maximum simulated angle of incidence rises to $\delta = 33.7^\circ$ for the edge cone, which is above the acceptance angle $\vartheta_M = 30.6^\circ$. Moreover the regions of the four sides of the hexagon, where the surfaces are described by a linear interpolation between the two Winston curves, feature lower detection efficiencies, as rays starting from these regions hit a non-ideal surfaces more often.

Nevertheless it has to be kept in mind that the overall fluctuations are small, even in the edge cone case shown in figure 5.10 (b) and (d). This can be read from the title of each plot, where the mean and RMS of the detection efficiency $\varepsilon_{\gamma/\delta}$ are given. The RMS is a measure of the homogeneity of the efficiency across the entrance window of the investigated cone. As the half apex angle of the light cone of the simulated point source is larger and close to or above the acceptance angle of the Winston curves in case of the edge cone, the RMS increases and the mean decreases.

As the Circular PMMA cone is a truncated Winston cone of acceptance angle $\vartheta_M = 33.7^\circ$, the corresponding plots in figure 5.10 (c) and (d) feature a lower RMS than in case of the final Hex-to-Square cone. The square structure in figure 5.10 (d) originates from the square SiPM, as a simulation with the SensL J-Series SiPM features the same square structure, while a simulation without SiPM, where a circular detector plane is located on the exit window of the Circular PMMA cone, only features a circular structure.

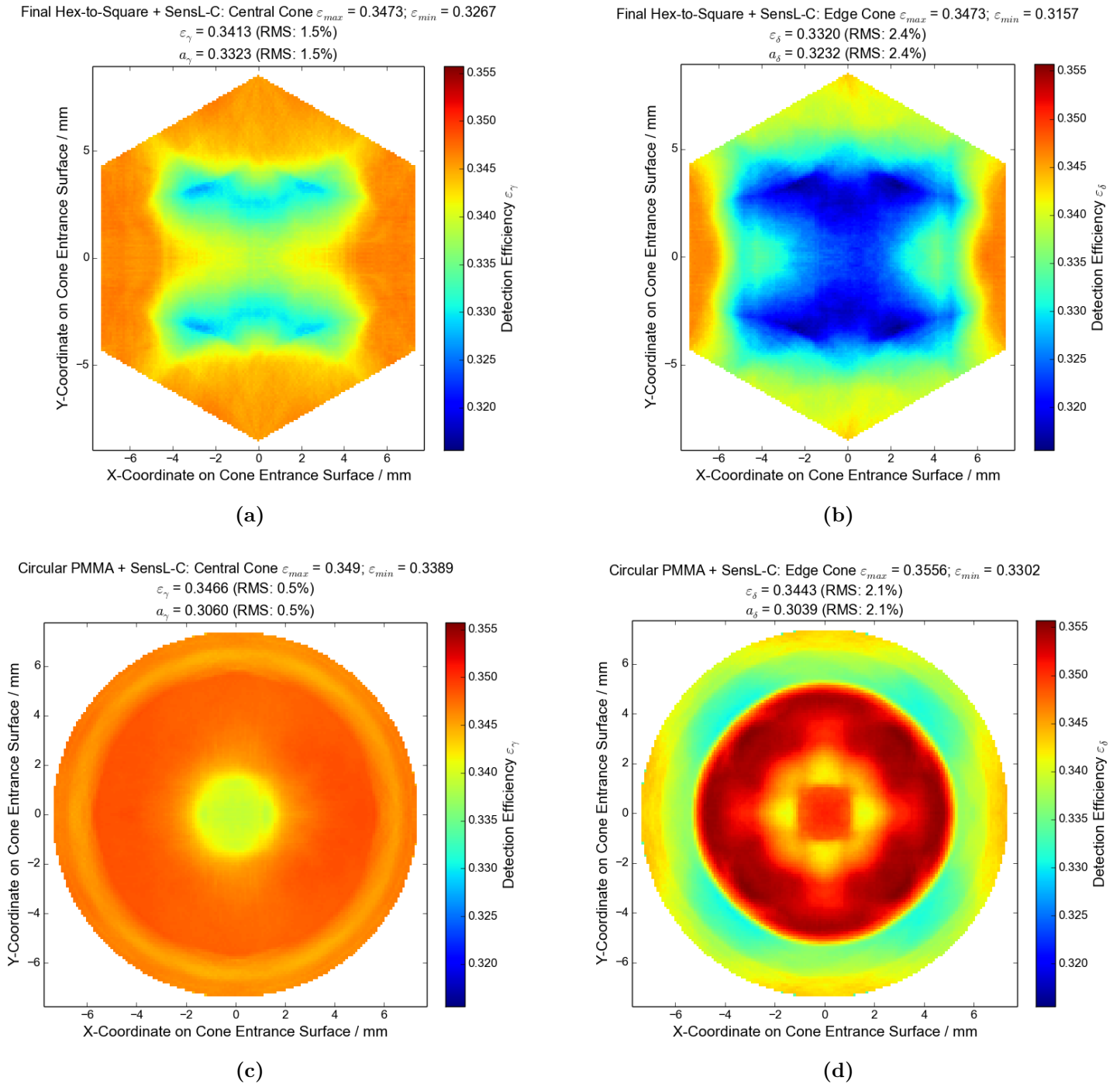


Figure 5.10: Simulated detection efficiencies for final Hex-to-Square and Circular PMMA cone with SensL C-Series SiPM. (a) and (c) on the left show the simulation of the final Hex-to-Square and Circular PMMA cone, respectively, for a central cone position. (b) and (d) on the right show the simulation of the final Hex-to-Square and Circular PMMA cone, respectively, for a edge cone position. The titles quote the maximum and minimum detection efficiency $\varepsilon_{max/min}$ as well as the mean and RMS of the detection efficiency $\varepsilon_{\gamma/\delta}$ and the efficiency regarding the fill factor $a_{\gamma/\delta}$.

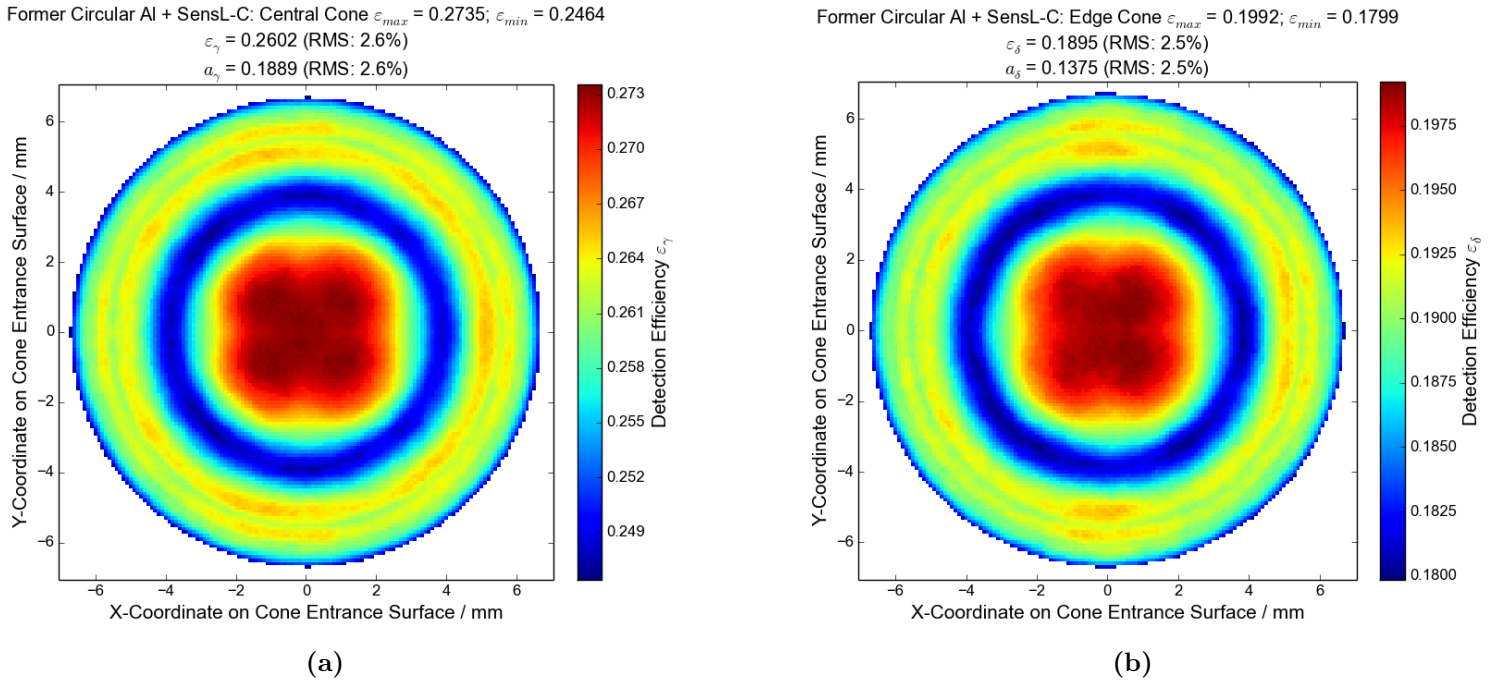


Figure 5.11: Simulated detection efficiencies for former Circular Al cone with SensL C-Series SiPM. (a) The left shows the detection efficiency of the former Circular Al cone in the central cone position. (b) The right shows the same in the edge cone position. The colorbar ranges are different from figure 5.10.

The plots for the former Circular Al cone are given in figure 5.11. The central hotspot in the center of both plots can be reasoned by the inferior reflectivity of aluminum compared to the total reflection in PMMA and reflection losses at the coating of the SiPM, as the photons of the point sources in the center most likely hit the SiPM directly and photons reflected from the aluminum walls of the cone hit the coating of the SiPM under larger angles of incidence, resulting in higher reflection losses. The latter effect is larger for aluminum cones than for PMMA cones, as the optical transition from air to coating is harder than from PMMA to coating. The drop of the detection efficiency from central to edge cone is much larger than in case of the previously discussed PMMA cones, because the Winston curve forming this cone has an acceptance angle, which is smaller than the maximum angle of incidence.

Comparison of the investigated cones

Table 5.2 gives an overview on the resulting mean detection efficiencies $\epsilon_{\gamma/\delta}$ and corresponding efficiencies considering the fill factor $a_{\gamma/\delta}$ of all investigated cones read out by a SensL C-Series SiPM, whose PDE is taken into account, at the wavelength of $\lambda = 380$ nm. The detection efficiencies of the aluminum cones cannot compete with any of the PMMA cones, especially at the edge cone position and when considering the fill factor. This is due to the reflectivity of aluminum of about 92% [73], which is less than the simulated 100% reflectivity achieved by the total reflection within the PMMA cones. Moreover the aluminum cones suffer from the harder optical transition to the SiPM coating causing larger reflection losses, the smaller

acceptance angle of the Winston curves and the smaller fill factor limited by the wall thickness of the aluminum cones.

As expected, the Circular PMMA cone yields the largest detection efficiency and the most homogeneous behaviour across the entrance window encoded in the small RMS, since this cone is an "ideal" Winston cone, whose concentration ratio is the largest achievable by definition as given in equation 5.3 and whose acceptance angle $\vartheta_M = 33.7^\circ$ matches the maximum angle of incidence reached in the edge cone position. Nonetheless the final Hex-to-Square cone yields the best overall performance with a detection efficiency considering the fill factor of $a_\gamma = 33.23\%$ in the central cone position and $a_\delta = 32.32\%$ in the edge cone position. This cone improves the performance of the currently installed former Circular Al cone of $a_\gamma = 18.89\%$ and $a_\delta = 13.75\%$ by approximately a factor of 2.

Nevertheless it has to be stated that Zemax does not implement absorption within the PMMA material. There are PMMA compounds available, which are transparent down to 350 nm wavelength, as for instance the Evonik XT 0A070 GT PMMA [75]. At this wavelength the PDE of all considered SiPMs begins to decay steeply (see datasheets [74], [56] and [57]), as for the SensL C-Series SiPM from about 29% at 350 nm to below 5% at about 315 nm [56]. Hence the difference in the performance of final Hex-to-Square cone and former Circular Al cone is not affected significantly by absorption in PMMA. A measurement of the absorption in different PMMA compounds at different wavelengths is presented in section 5.6.

Studies with modified simulations

For the two most promising cones, final Hex-to-Square and Circular PMMA cone, as well as the former Circular Al cone another simulation is carried out in the edge cone position to study the influence of surface imperfections. In this simulation 5% of the rays hitting the surfaces of the investigated cone are ideally diffuse reflected via Lambertian scattering. Moreover these 5% of the rays are each split into two rays during the diffuse reflection. Table 5.3 shows that the detection efficiency of the former Circular Al cone is almost not affected, while the PMMA cones lose about 10% relative to the simulation with ideal surfaces in table 5.2. This loss in the PMMA cones is caused by the loss of internal total reflection at steep incidence angles. The loss can be larger than the defined 5%, as rays hit the surfaces of the cones multiple times before entering the SiPM. Nevertheless the PMMA cones are still about a factor of 2 more efficient than the aluminum cone in case of the simulated edge cone position.

Since a future perspective of IceAct is the installation of SensL J-Series SiPMs with a superior UV response down to a wavelength of 200 nm [57] and a superior overall PDE as shown in figure 5.9, the same cones are simulated with this SiPM instead of the SensL C-Series SiPM. The geometry of the SiPM is again adopted from the datasheet of the SiPM [57] and the coating is chosen to be the Zemax material *N-PK51* with a refractive index of $n_d = 1.53$. Table 5.4 summarizes the results. Because of better matching refractive indices and especially the larger PDE of the SiPM, the resulting detection efficiencies of all cones are about 25% larger compared to the SensL C-Series SiPM. The differences between the cones are similar to the SensL C-Series SiPM, such that also in this case the final Hex-to-Square cone fits best for the

application in IceAct with a detection efficiency considering the fill factor of 41.69% in case of the central cone position and 40.69% in case of the edge cone position.

Furthermore a simulation for the edge cone position without any SiPM is carried out with the exit window of the cones as detector plane. The resulting detection efficiencies are given in table 5.5. These pure detection efficiencies of the cones reveal the outstanding collection properties of the PMMA cones. While the former Circular Al cone loses almost 50% of the light on the way to the exit window, both final Hex-to-Square and Circular PMMA cone almost transmit all the light that enters the cone, since the reflection loss at the entrance window equals about 4% and more than 92% reach the exit window. The performance of the former Circular Al cone is mostly limited by the small acceptance angle.

In summary these simulations show the potential of the final Hex-to-Square cone, which significantly improves the former Circular Al cone with a larger acceptance and with an optimized fill factor in the focal plane. Since another requirement presented in section 5.1 is the homogeneity of the SiPM illumination, the next section studies, whether the final Hex-to-Square cone can convince in this field, too.

Cone type	Central cone		Edge cone	
	ε_γ	a_γ	ε_δ	a_δ
Final Hex-to-Square	$0.3413 \pm 1.5\%$	$0.3323 \pm 1.5\%$	$0.3320 \pm 2.4\%$	$0.3232 \pm 2.4\%$
Former Circular Al	$0.2602 \pm 2.6\%$	$0.1889 \pm 2.6\%$	$0.1895 \pm 2.5\%$	$0.1375 \pm 2.5\%$
Circular PMMA	$0.3466 \pm 0.5\%$	$0.3060 \pm 0.5\%$	$0.3443 \pm 2.1\%$	$0.3039 \pm 2.1\%$
Hex-to-Square WP fp	$0.328 \pm 5.7\%$	$0.320 \pm 5.7\%$	$0.314 \pm 7.5\%$	$0.306 \pm 7.5\%$
Hex-to-Square WP Slope	$0.319 \pm 13.0\%$	$0.310 \pm 13.0\%$		
Hex-to-Square 2P Slope	$0.311 \pm 10.1\%$	$0.303 \pm 10.1\%$		
Hex-to-Hex	$0.330 \pm 6.7\%$	$0.321 \pm 6.7\%$	$0.311 \pm 11.3\%$	$0.303 \pm 11.3\%$
Square-to-Square	$0.326 \pm 6.3\%$	$0.318 \pm 6.3\%$	$0.305 \pm 8.2\%$	$0.297 \pm 8.2\%$
Circular-to-Square	$0.322 \pm 6.5\%$	$0.285 \pm 6.5\%$		
Hex-to-Square Lin. Short	$0.282 \pm 17.2\%$	$0.274 \pm 17.2\%$		
Hex-to-Square Lin. Long				
Hex-to-Hex Al	$0.192 \pm 14.8\%$	$0.153 \pm 14.8\%$	$0.140 \pm 14.8\%$	$0.112 \pm 14.8\%$
Hex-to-Square Lin. Al	$0.247 \pm 7.5\%$	$0.198 \pm 7.5\%$		
Circular-to-Square Al				
Square-to-Square Al	$0.246 \pm 9.4\%$	$0.197 \pm 9.4\%$		

Table 5.2: Results of detection efficiency simulation of investigated cones. The system of cone and SensL C-Series SiPM is simulated considering the PDE of the SiPM at a wavelength of $\lambda = 380$ nm. The left side presents the mean detection efficiency ε_γ and the mean detection efficiency considering the fill factor a_γ with their corresponding RMSs at the central cone position. The right side provides the same parameters at the edge cone position. Not all the investigated cones have been simulated, as they were ruled out as promising candidates beforehand. Table 5.1 on page 46 lists the characteristics of the investigated cones.

Cone type	Central cone	
	ε_δ	a_δ
Final Hex-to-Square	$0.3003 \pm 1.8\%$	$0.2923 \pm 1.8\%$
Former Circular Al	$0.1837 \pm 2.7\%$	$0.1333 \pm 2.7\%$
Circular PMMA	$0.3143 \pm 3.1\%$	$0.2775 \pm 3.1\%$

Table 5.3: Results of detection efficiency simulation with imperfect surfaces. 5% of the rays hitting the cone surfaces are split into two and both rays are reflected ideally diffuse. The system of cone and SensL C-Series SiPM is simulated considering the PDE of the SiPM at a wavelength of $\lambda = 380$ nm. Presented are the mean detection efficiency ε_δ and the mean detection efficiency considering the fill factor a_δ with their corresponding RMSs at the edge cone position.

Cone type	Central cone		Edge cone	
	ε_γ	a_γ	ε_δ	a_δ
Final Hex-to-Square	$0.4282 \pm 1.3\%$	$0.4169 \pm 1.3\%$	$0.4180 \pm 2.3\%$	$0.4069 \pm 2.3\%$
Former Circular Al	$0.3343 \pm 2.7\%$	$0.2427 \pm 2.7\%$	$0.2433 \pm 2.6\%$	$0.1766 \pm 2.6\%$
Circular PMMA	$0.4329 \pm 0.3\%$	$0.3822 \pm 0.3\%$	$0.434 \pm 2.6\%$	$0.383 \pm 2.6\%$

Table 5.4: Results of detection efficiency simulation for SensL J-Series SiPM. The simulated wavelength equals $\lambda = 380$ nm and the corresponding PDE of the SiPM is taken into account. The left side presents the mean detection efficiency ε_γ and the mean detection efficiency considering the fill factor a_γ with their corresponding RMSs at the central cone position. The right side provides the same parameters at the edge cone position.

Cone type	Edge cone	
	ε_δ	a_δ
Final Hex-to-Square	$0.926 \pm 2.2\%$	$0.901 \pm 2.2\%$
Former Circular Al	$0.568 \pm 2.3\%$	$0.4124 \pm 2.3\%$
Circular PMMA	$0.936 \pm 1.5\%$	$0.826 \pm 1.5\%$

Table 5.5: Results of detection efficiency simulation of cones only. The simulated wavelength equals $\lambda = 380$ nm. Presented are the mean detection efficiency ε_δ and the mean detection efficiency considering the fill factor a_δ with their corresponding RMSs at the edge cone position.

5.4.2 Simulation of the SiPM Illumination

This Zemax simulation analyses the homogeneity of the illumination of the SensL C-Series SiPM, which is connected to the final Hex-to-Square, former Circular Al and Circular PMMA cone, respectively. 10 million light rays of 380 nm wavelength are simulated with their source position being randomly distributed within the entrance window of the investigated cone. In case of PMMA cones, the sources are simulated just above the entrance window of the cone to account for refraction at the surface. As the illumination of the SiPM is studied, the detector plane within the silicon layer of the SiPM is evenly divided into 138x138 square cells emulating the 18980 G-APD cells of the SensL C-Series (see table 3.1 on page 26).

Three different illuminations are simulated. First all rays are simulated in parallel to each other penetrating the entrance window of the cone perpendicularly, in order to investigate the focussing property of the cone. Second the illumination of the entrance window of the cone within IceAct is simulated. Here again the two extreme cases of central and edge cone position are chosen analog to the previous section. Thus the angle of incidence of each ray is randomly chosen between $\pm\gamma$ and $\pm\delta$ in case of the central and edge cone position, respectively. Again the simulation of the edge cone is approximated to be symmetric, which influences the results, such that the focus will be on the central cone position. Figure 5.12 shows the resulting detector views of the 6x6 mm² large SiPM, where the relative intensity in terms of the maximum cell intensity is color-coded with red being the highest intensity, thus 1, and dark blue being almost 0 intensity. The mean of the relative intensity given on top of each detector view is a measure for the homogeneity of the SiPM illumination, though the high binning results in statistical fluctuations between the cells decreasing the mean value systematically.

On the left of figure 5.12 the detector view for perpendicular illumination is shown for each cone model, where the former Circular Al cone in the middle features white areas in the edges indicating that there the SiPM is not hit by a single ray. All three cones focus the perpendicular light on the exit window, which is specific for Winston cones. Consequently the SiPM illumination features circular hotspots for the circular cones and four dot-shaped hotspots in case of the final Hex-to-Square cone. This behaviour of collecting the perpendicular light on small hotspots of the SiPM decreases the dynamic range of the SiPM, since a fired G-APD cell cannot detect the photons impinging during the recovery time. Fortunately the cones are located behind the Fresnel lens, such that the cones are never illuminated by parallel light in case of IceAct.

The detector views for the illumination of IceAct's central cone are shown in the central column of figure 5.12. The structure of the illumination of the whole SiPM is most homogeneous for the final Hex-to-Square cone due to its square exit window, while the former Circular Al cone features the most homogeneous illumination within the circular exit window, which is dominated by statistical fluctuations. In case of both circular cones the edges of the SiPM are dark blue, thus practically not illuminated, as only a very small fraction of the photons reach the edges by multiple reflections within the SiPM. In contrast the final Hex-to-Square cone even illuminates the edges with about 60% of the maximum cell intensity, such that the final Hex-to-

Square cone yields the best results with a mean relative intensity of 0.7 for the square SiPM. The structure in the detector view of the Circular PMMA cone in the middle of the bottom of figure 5.12 might be caused by the larger acceptance angle compared to the former Circular Al cone as well as multiple reflections including total reflection at the entrance window, which is not existent in case of the aluminum cone. Since the IceAct telescope observes Cherenkov light pulses generated by air showers with fluxes in the range of tens to a few hundreds of photons per event for the whole 61-pixel camera, each of the three cones matches the requirement of not lowering the dynamic range of the SiPM by strong local inhomogeneities in the illumination.

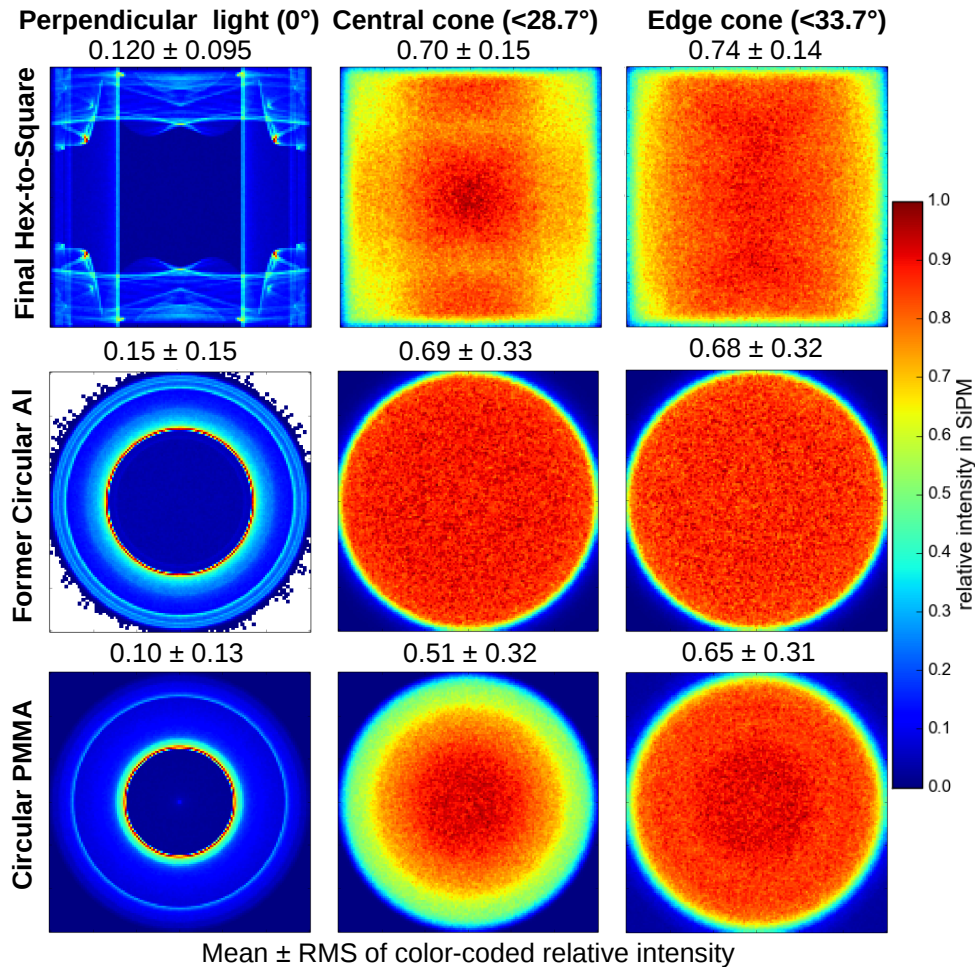


Figure 5.12: Simulated SiPM illumination for investigated cones. The top row gives the detector views for the final Hex-to-Square cone, while middle and bottom row correspond to former Circular Al and Circular PMMA cone, respectively. Photons of $\lambda = 380$ nm wavelength are simulated randomly on the entrance window of each cone perpendicular to the entrance window or with maximum angles of incidence of $\gamma = 28.7^\circ$ and $\delta = 33.7^\circ$, respectively, going from left to right column.

5.4.3 Simulation of the Angular Acceptance

While the simulation in section 5.4.1 studied the overall detection efficiency of the investigated cones, here the angular acceptance along different symmetry axes is analysed to characterize the final Hex-to-Square, former Circular Al and Circular PMMA cone in more detail. Figure 5.13 shows the simulation setup comprising cone and SensL C-Series SiPM using the example of the final Hex-to-Square cone. An extended source emits 50000 parallel rays of $\lambda = 380$ nm wavelength perpendicularly illuminating the whole entrance surface of the final Hex-to-Square cone. The cone is rotated around any of the four axes to determine the angular acceptance along the particular axis. A hexagonal cylinder encloses the cone to absorb rays that do not hit the entrance window of the cone, when the cone is rotated. This is necessary since the shape of the source does not change with the cone rotation such that the effective area of the entrance window of the cone, hit by the parallel light of the source, decreases with increasing cone rotation angle θ , which is corrected for by dividing the detection efficiencies given by the simulation by $\cos(\theta)$. In case of the circular cones the rotation axis is chosen to traverse two opposite points, where the circular exit window of the cone touches the square side of the SiPM.

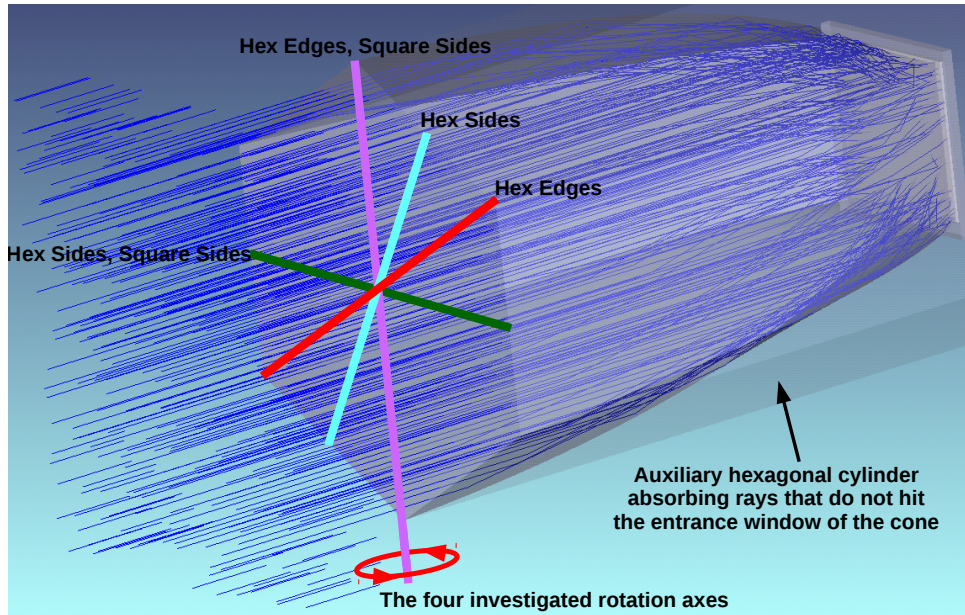


Figure 5.13: Screenshot of the simulation of the angular efficiency.

Figure 5.14 summarizes the results plotting the efficiency, which is weighted with the PDE of the SensL C-Series SiPM via equation 5.17, against the cone rotation angle θ . The former Circular Al cone cannot compete with the PMMA cones, since its acceptance angle of $\vartheta_M = 26.6^\circ$ causes the drop of the efficiency before the reaching the maximum angle of incidence in the IceAct camera of $\delta = 33.7^\circ$. Moreover the efficiency plateau of any aluminum cone at small cone rotation angles lies below the one of PMMA cones, because of reflection losses caused by the harder optical transition at the coating of the SiPM and the inferior reflectivity of aluminum compared to the total reflection within PMMA.

The purple curve in figure 5.14 yields that the angular acceptance of the final Hex-to-Square cone is largest, when the cone is rotated around the purple axis in figure 5.13 running through the edges of the hexagon, where the Winston curves with the smaller acceptance angle end, which are labelled as green line in figure 5.4 (a) on page 48. This is expected as for this rotation axis the fraction of rays being reflected at the surface, defined by the Winston curves with the larger acceptance angle $\vartheta_M = 37.2^\circ$, is largest. The same argument holds for the rotation around the green axis in figure 5.13 running through the end points of the Winston curve with the larger acceptance angle, where most rays hit the imperfect surfaces of the cone resulting in the smallest and most washed-out angular acceptance.

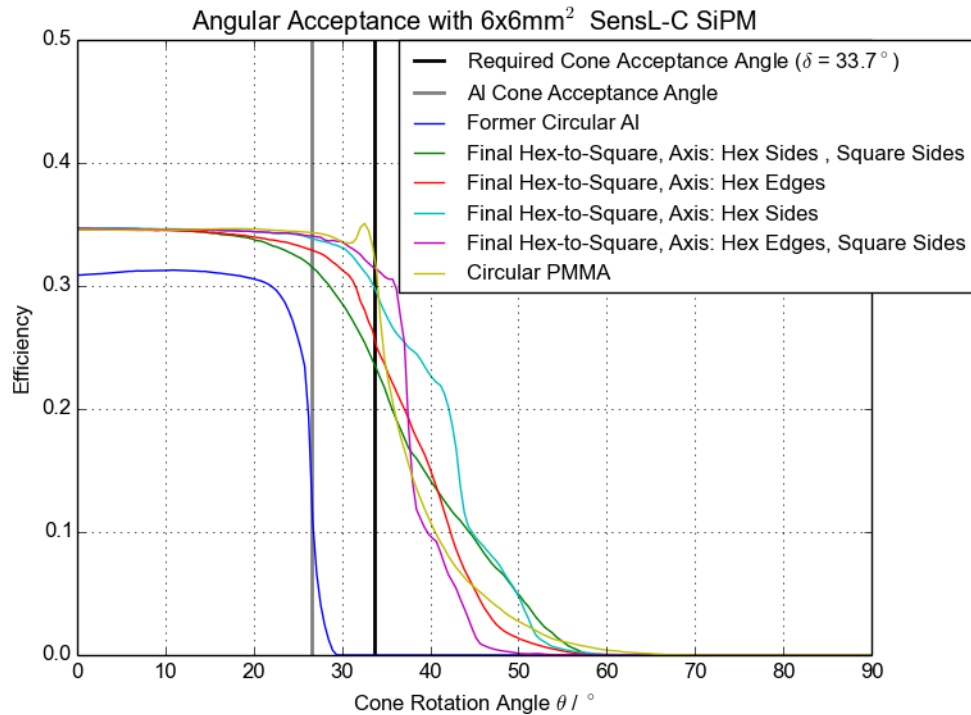


Figure 5.14: Plot of angular efficiency obtained from simulation. *Axis* in the legend denotes the rotation axis of the final Hex-to-Square cone shown in figure 5.13 (color-coding fits to this figure).

Since the Circular PMMA cone is a truncated "ideal" Winston cone with an acceptance angle of 33.7° , this cone yields the best performance in the angular acceptance cutting the efficiency sharply at the cone rotation angle of $\theta = 33.7^\circ$. The bump in the efficiency just before reaching $\theta = 33.7^\circ$ is reasoned with figure 5.15. Since a ray tracing of this simulation is confusing due to the large area of the source, the figure shows the ray tracing of the Circular PMMA cone being illuminated by a circular source of 0.1 mm Gaussian width hitting the entrance window of the cone centrally under an angle of incidence of 32° . On the bottom multiple reflections at the side-wall of the SiPM increase the detection efficiency of rays impinging under these angles of incidence. This efficiency can be larger than the one of perpendicular illumination, because the overall probability of a photon hitting the detector plane

may increase, if the photon is reflected multiple times, which is accounted for in Zemax by ray splitting at surface transitions.

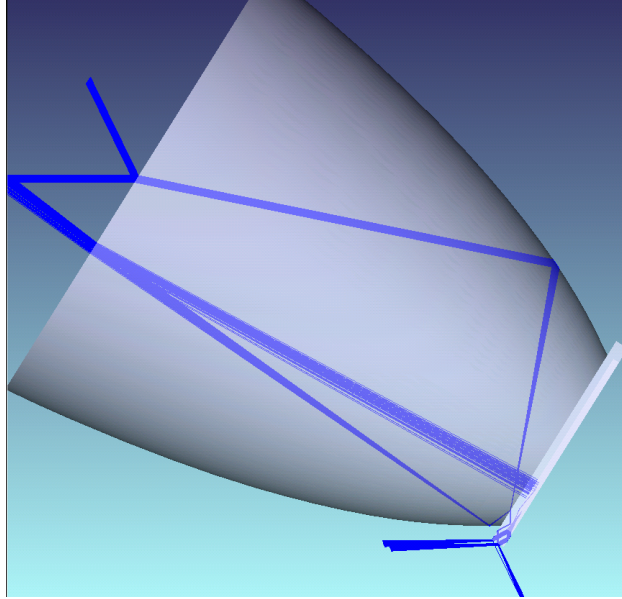


Figure 5.15: Ray tracing of Circular PMMA cone. The cone is illuminated by a circular source of 0.1 mm Gaussian width hitting the entrance window of the cone centrally under an angle of incidence of 32° .

In summary this simulation of the angular acceptance yields that the Circular PMMA cone provides the most ideal performance followed by the final Hex-to-Square cone, while the former Circular Al cone cannot compete, which is in agreement with the results of the simulations in section 5.4.1. Nevertheless the final Hex-to-Square cone has the best overall performance taking fill factor in the focal plane and homogeneity of the illumination of the SiPM into account. Therefore this cone is built to perform measurements for cross-checks of the simulations in section 5.5 and to compare with measurements of the former Circular Al cone. Moreover the effect of absorption in PMMA has to be studied to quantify the effect on the results of the simulations, which is done in section 5.6.

5.4.4 Simulation for Comparison with Measurement

This simulation emulates the measurements of final Hex-to-Square and former Circular Al cone in section 5.5 to cross-check, whether all the Zemax simulations carried out can reproduce the reality. Figure 5.16 shows the setup exemplary for the final Hex-to-Square cone consisting of cone and coupled $6 \times 6 \text{ mm}^2$ Hamamatsu S13360 SiPM used in the measurement. The geometry of the SiPM is adopted from the datasheet [74] and *N-PSK3* with a refractive index of $n_d = 1.55$ is chosen as coating material. Again the PDE of the SiPM is included in the efficiency of the simulation via equation 5.17. As the measurement uses a green laser as light source, here 10000 light rays with a wavelength of $\lambda = 532 \text{ nm}$ are simulated hitting the center of the entrance window perpendicularly. The width of the laser beam is simulated for both

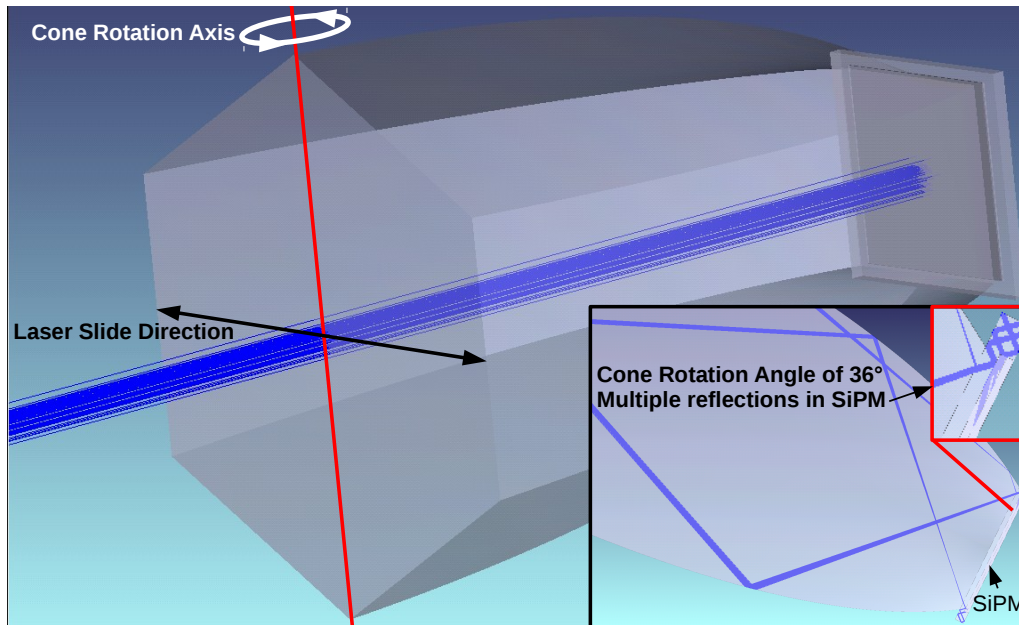


Figure 5.16: Simulation for measurement comparison and multiple reflections in SiPM. The final Hex-to-Square cone and Hamamatsu S13360 SiPM are illuminated by a source of $\lambda = 532$ nm wavelength penetrating the center of the entrance window perpendicularly. The cone is either rotated or the laser is moved. The small box on the bottom right shows a blow-up for a 36° cone rotation angle.

0.45 mm and 0.85 mm Gaussian width yielding about 0.9 mm and 1.7 mm beam diameter, respectively. Either the cone is rotated around the labelled cone rotation axis running through top and bottom edge of the hexagonal entrance window, where the Winston curves with the smaller acceptance angle end, or the laser is moved along the labelled laser slide direction running through the surfaces that are defined by extrusions of the Winston curve with larger acceptance angle. Therefore always the surfaces that are defined by extrusions of the Winston curve with larger acceptance angle are scanned by the laser beam. In case of the former Circular Al cone the scan runs parallel to a side wall of the square SiPM and crosses the points, where the circular exit window of the cone touches the side of the SiPM. The simulations of the final Hex-to-Square cone are carried out with touching cone exit window and SiPM as well as with a 0.001 mm small air gap between cone exit window and SiPM to study the effect of total reflection.

Figure 5.17 gives the resulting efficiency plots for the sliding of the laser on the left and the cone rotation on the right. The only difference between simulations with different laser beam diameters of 0.9 mm or 1.7 mm is a minor resolution in case of the larger beam diameter working like a sliding average on the efficiency values of the smaller beam diameter.

This effect is relevant in the top left plot of figure 5.17, where the laser slides across the final Hex-to-Square cone coupled to the SiPM with an air gap, because the two peak structure between ± 5 mm and ± 7.5 mm distance to the cone center is not resolved by the simulation with the larger beam diameter. Because of the total

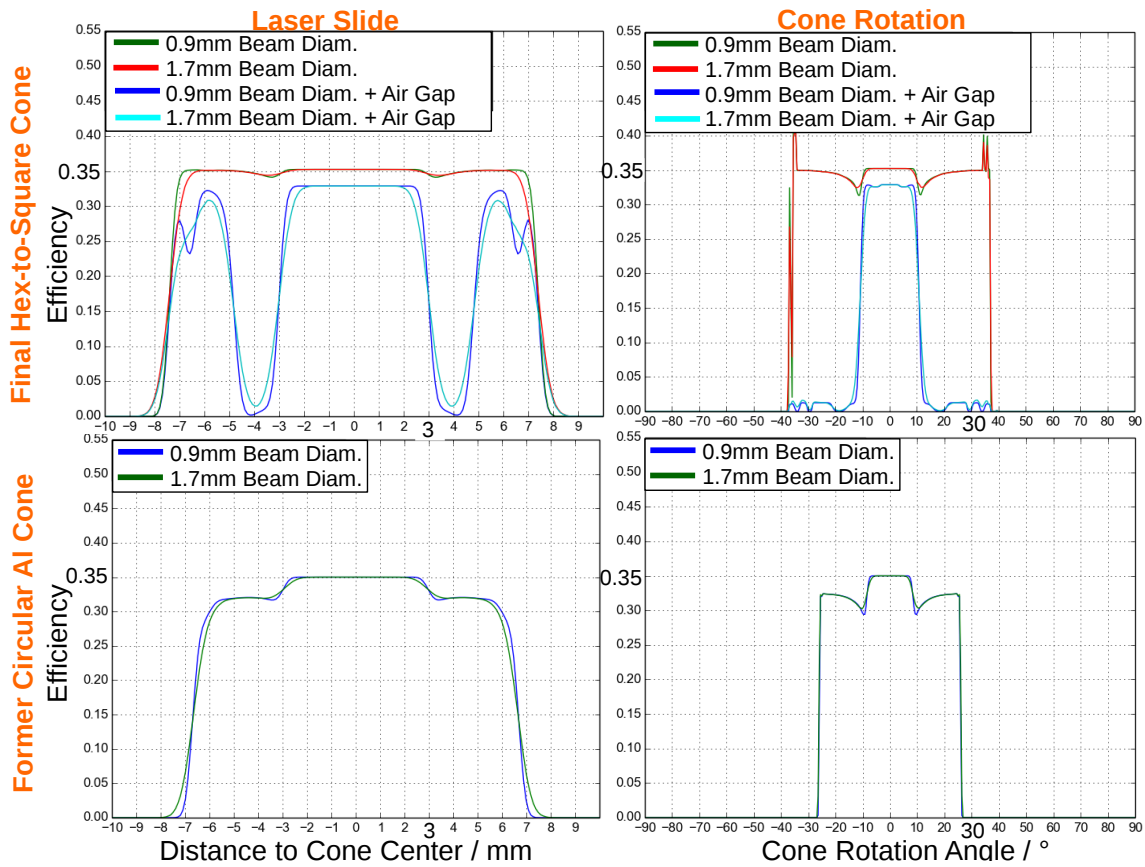


Figure 5.17: Resulting efficiency plots of the simulation of the measurement. The top row shows results for the final Hex-to-Square cone, while the bottom row shows the same for the former Circular Al cone. On the left the efficiency is plotted as function of the laser position and on the right as function of the cone rotation angle.

reflection at the air gap between cone and SiPM, the efficiency drops drastically, when the laser beam leaves the exit window of the cone at ± 3 mm distance to the cone center. The slope of the Winston curve is flattest close to the exit window and steepens to infinite slope at the entrance window. Therefore laser beams reflected by the Winston curve at larger distances to the cone center reach the exit window of the cone under smaller angles of incidence such that they are not totally reflected anymore at about ± 6 mm distance.

If there is no air gap between the cone and the SiPM the efficiency of the final Hex-to-Square cone is almost independent of the laser beam position, which is also plotted in the top left of figure 5.17. The small dip at 3 mm distance to the cone center, thus at the edge of the exit window, is caused by the flat slope of the Winston curve at this position, which reflects the laser beam with such large incidence angles into the SiPM, that a large fraction of the beam gets lost at the sides of the coating of the SiPM, since there is no total reflection as for instance in figure 5.15. This effect is the same in the plots on the right of figure 5.17 at cone rotation angles of about $\pm 10^\circ$, since at these angles the laser beam also hits the edge of the exit window. The top right plot features sharply peaking maxima just before the cone

rotation angle equals the acceptance angle of the final Hex-to-Square cone surfaces of $\vartheta_M = \pm 37.2^\circ$. The reason for these peaks is analog to the effect discussed in figure 5.15 of the previous section. On the bottom right of figure 5.16 a ray tracing at a cone rotation angle of 36° is shown with a blow-up of the side wall of the SiPM. The multiple reflections between SiPM coating and silicon layer sustained by total reflections between SiPM coating and air allow for a larger overall photon detection efficiency compared to perpendicular illumination. The top right plot in figure 5.17 also shows that the SiPM has to be coupled to a PMMA cone without an air gap, as otherwise all the rays that do not reach the SiPM directly are totally reflected and do not reach the SiPM. On the left edge of the curves for well-coupled cone and SiPM there is an additional peak at about -40° , which is not present on the right side at $+40^\circ$, because the Hamamatsu SiPM is asymmetric. The silicon layer is not placed in the center of the coating.

The plots of the former Circular Al cone also feature the dip structure, but here the efficiency does not recover to the plateau of central and perpendicular illumination, because of the inferior reflectivity of aluminum and larger reflection losses at the harder optical transition to the SiPM. Moreover this cone has a smaller entrance window diameter than the final Hex-to-Square cone resulting in a cutoff at ± 6.71 mm distance to the cone center instead of ± 7.4 mm. Furthermore the acceptance angle cuts of the efficiency at cone rotation angles of $\pm 26.6^\circ$ instead of $\pm 37.2^\circ$ in case of the final Hex-to-Square cone. In exchange this aluminum cone is not affected by total reflection losses. Whether this simulation can be reproduced in reality, is studied in the following section.

5.5 Cone Measurement for Verification of Simulation and Manufacturing Optimization

Since the final Hex-to-Square cone yields the best performance for the application in the camera of the IceAct telescope, in this section measurements of this cone and the former Circular Al cone are presented and compared to the simulations of the previous section. Models of the final Hex-to-Square cone built by three different manufacturers are investigated to study how the manufacturing of the cone can be optimized. Measurement setup and procedure as well as the simulation of the measurement in the previous section are based on a Bachelor's thesis carried out at the III. Physikalisches Institut B, RWTH Aachen [76].

5.5.1 Measurement Setup and Procedure

The measurement setup is shown in figure 5.18, where the entrance window of the respective cone is scanned by a Thorlabs CPS532 laser of $\lambda = 532$ nm wavelength [77]. The light intensity reaching the exit window of the cone is measured by a 6×6 mm² Hamamatsu S13360-6050PE SiPM [74], whose specifications are given in table 5.6. Either the laser is slid across the entrance window of the cone or the cone is rotated around its entrance window, as shown in figure 5.16 on page 68.

The laser beam diameter is regulated by a Thorlabs SM1D12 lever-actuated iris diaphragm [78]. In case of a beam diameter of 0.9 mm, the Thorlabs neutral density

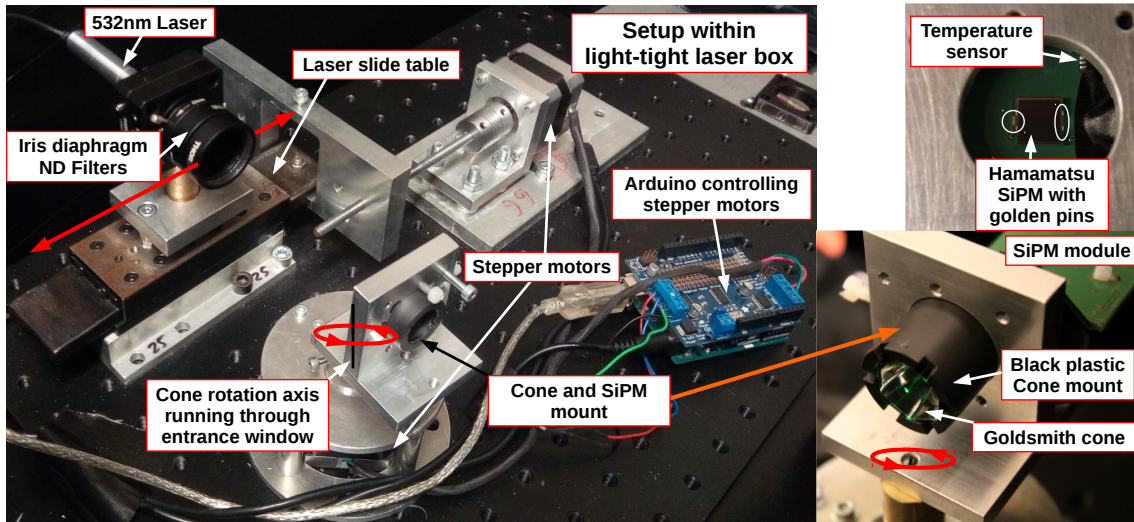


Figure 5.18: Setup of cone measurement for verification of simulation and manufacturing optimization. The setup is placed inside of a light tight laser box and controlled by a Laptop. An Arduino operates two stepper motors, one sliding the laser, whose attenuated beam scans the entrance window of the studied cone, and the other rotating the cone, which is mounted in a black plastic cylinder and coupled to a Hamamatsu SiPM controlled by a temperature compensating power supply. The green PCB in the top right picture is completely covered with black tape, while the visible golden pins at the sides of the SiPM are always uncovered.

filters NE20A-A [79] and NE30A [80] attenuate the beam to a factor of about 10^{-5} of the initial intensity, while the Thorlabs neutral density filters NE10A-A [79] and NE50A [80] attenuate the beam to a factor of about 10^{-6} of the initial intensity in case of a 1.7 mm beam diameter, because the intensity has to be adapted to the SiPM.

The rotation of an Adafruit NEMA-17 stepper motor [81] is transformed into a translational movement via a thread to slide the laser across the entrance window of the cone, while another stepper motor of this type rotates the mounting of the cone around the axis running through the center of entrance surface of the cone. The stepper motors are controlled by an Adafruit Motor Shield V2 [82] mounted to an Arduino Uno Rev3 [83]. All these components are controlled by a python-script on a laptop outside of the laser box. The stepper motors feature 200 steps per revolution and a MICROSTEP mode with 16 intermediate steps. The stepper motor moving the laser is operated in DOUBLE mode resulting in a higher torque accounting for the power needed to rotate the thread. Using graph paper it is found that the laser travels a distance of 4 cm with 10000(50) steps, resulting in a minimum step size of the stepper motor of $4.00(02) \mu\text{m}$.

As shown on the bottom right of figure 5.18, the cone is housed in a black plastic cylinder, which is fastened in an aluminum block by a screw. The mount is produced in the workshop of the III. Physikalisches Institut B, RWTH Aachen, and can be adjusted for the length of the final Hex-to-Square cone and the former Circular Al cone.

At the backside of the aluminum block the Hamamatsu SiPM is attached as shown on the top right of figure 5.18. The PCB of the SiPM houses a temperature sensor on the top right and a second SiPM behind the aluminum at the right side. This spare SiPM is additionally protected from incident light by black tape. The summed signal of both SiPMs is read out by a power supply module [84] operating the Hamamatsu C11204-02 power supply [85], which adjusts the bias voltage of the SiPM V_o for temperature variations with a resolution of about 1.8 mV and a precision of ± 10 mV [85]. SiPM module and a characterization of the SiPMs are provided by the Auger group of the III. Physikalisches Institut, RWTH Aachen.

In order to obtain the default overvoltage of 1.4 V, the bias voltage of the SiPMs has to be set to $V_b = 54.4$ V at $T_b = 25^\circ\text{C}$, while the linear temperature coefficient is given by $\beta = 52 \frac{\text{mV}}{\text{K}}$. The power supply adjusts the bias voltage via $V_o = \beta(T - T_b)/1000 + V_b$, where T equals the temperature measured by the temperature sensor in $^\circ\text{C}$ [84]. During the measurements the current flowing through the two SiPMs is read out from the power supply module via the python-script on the laptop. The current is limited to a maximum of 2 mA and the resolution equals 0.005194 mA [86]. Because currents in the SiPM reach about 0.2 mA during the measurements, the digitization can be neglected, since the systematic uncertainties caused by operating the SiPM at the edge of its dynamic range, are dominating. The current is read out, because the continuous laser beam does not allow for short-lived dim pulses, which could be triggered on for voltage pulse measurements. The measurements were also carried out with a photodiode, but as the results for the PMMA cones are affected by an unavoidable air gap intrinsic to the photodiode, these measurements are not shown here.

Figure 5.19 (a) gives an overview on the models of the final Hex-to-Square cone produced by a dental laboratory on the left and at the Erlangen Centre for Astroparticle Physics on the right. The dental laboratory cone features sharp edges, which are desired, since this conserves the shape of the surfaces defined by Winston curves. However the surfaces show small grooves and the PMMA of this cone is not as pure and transparent as the one from Erlangen, which will be discussed in section 5.6. Moreover the polish of the Erlangen cone resulted in smooth surfaces but therefore

	Hamamatsu S13360-6050PE
Temp. and V_{Ov}	25 $^\circ\text{C}$, 3 V
Breakdown voltage	(53 \pm 5) V
Sensor size	6 x 6 mm ²
Cell / Pitch size	50 μm (pitch)
Number of cells	14400
Fill factor	74 %
Coating refractive index	1.55 (Epoxy resin)
PDE at λ_p	40 % at 450 nm
Spectral response range	320 nm - 900 nm
β	54 $\frac{\text{mV}}{\text{K}}$
Gain	$1.7 \cdot 10^6$
0.5 p.e. dark noise	2 Mcps
Optical Crosstalk	3 %
Afterpulsing	-
Recovery time	-

Table 5.6: Characteristics of the SiPM used in the setup. This Hamamatsu S13360-6050PE SiPM is the follow-up version of the Hamamatsu S12573-100X SiPM used in the FAMOUS / IceAct prototype tested in Erlangen (see table 3.1). The values are taken from the datasheet [74].

also rounded edges and a bellied exit window, which makes the coupling via silicone gel difficult, as shown in figure 5.19 (b), where air bubbles in the center and overflowing silicone gel at the exit window sides occur. Another model from a goldsmith, whose properties are comparable to the ones of the Erlangen cone, is shown on the bottom right of figure 5.18.

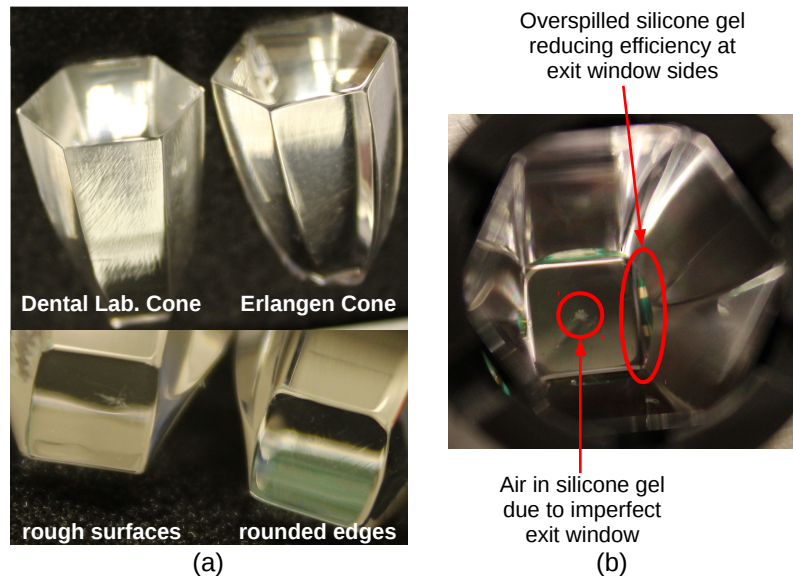


Figure 5.19: Final Hex-to-Square cones from different manufacturers and coupling issues. (a) The left shows a cone from the dental laboratory and from the university in Erlangen. (b) The right reveals issues of the coupling to the SiPM.

The exit window of the final Hex-to-Square cones is coupled to the SiPM either with a high viscous silicone gel or without any coupling, thus an air gap. The former Circular Al cone is pressed on the SiPM using another black plastic cylinder.

The measurement procedure begins with the alignment of the starting position of the setup, which is carried out with the laser beam reflections at cone entrance window and SiPM visible on the iris diaphragm. In the starting position, the laser penetrates the center of the entrance window perpendicularly and the entrance window is aligned in parallel to the sliding direction of the laser. Hereafter the entrance window of the cone is scanned with the laser in 0.1 mm steps. Afterwards the cone is rotated in MICROSTEP mode between incidence angles of the laser of $\pm 90^\circ$ with a 0.45° step size. After each step a delay of 1.5 s is implemented to allow the SiPM current to stabilize. Then for each step position three current measurements are carried out with 0.2 s delays in between to calculate mean and standard deviation of the current at each position.

5.5.1.1 Adjustment of Laser Beam Diameter

In order to check, whether the laser beam is attenuated enough to measure within the dynamic range of the SiPM for the minimum possible diameter of 0.9 mm, the ratio of the current between central perpendicular illumination and the indirect illumination after a reflection on the surface of the former Circular Al cone at the -4 mm position

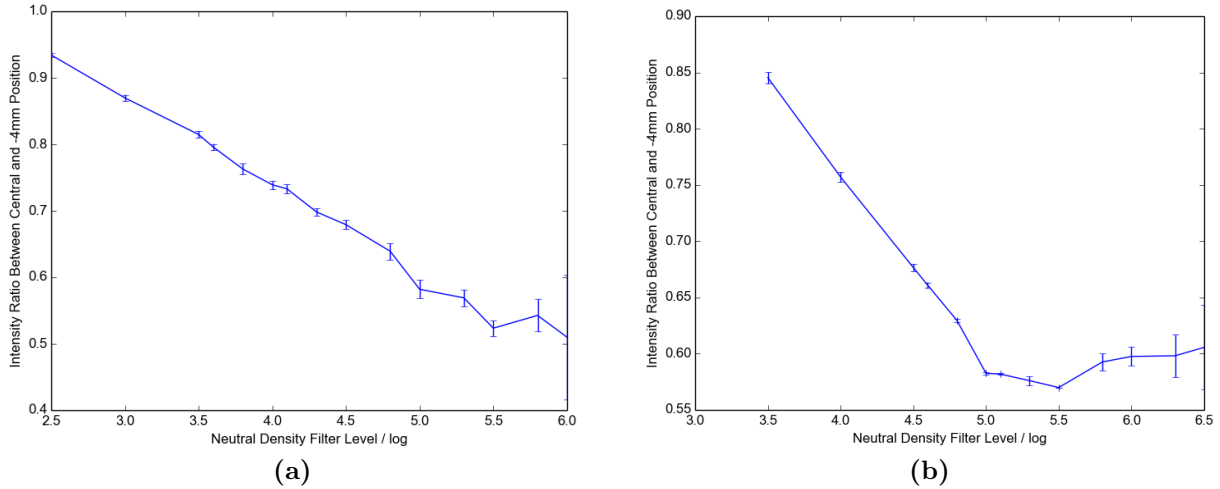


Figure 5.20: Dynamic range of SiPM considering different beam diameters. (a) The left plots the intensity ratio of the SiPM currents measured for direct illumination and indirect illumination after a reflection on the surface of the former Circular Al cone at the -4 mm position on the left of figure 5.24 against the attenuation of the laser with the minimum beam diameter of 0.9 ± 0.1 mm. (b) The right plots the same for a beam diameter of the laser of 1.7 ± 0.2 mm.

on the left of figure 5.24 is plotted against the attenuation by different neutral density filters from Thorlabs [79], [80]. Figure 5.20 (a) shows the resulting plot. Each data point equals the ratio of the mean SiPM currents and the propagated standard deviations obtained from 2.5 min continuous data taking per position. The error on the attenuation, thus the neutral density filter level, is not plotted, since the interest is in finding the minimum neutral density filter level from which on the intensity ratio does not change anymore. This plateau indicates that the intensities lie within the dynamic range of the SiPM. Although no clear plateau is visible, the attenuation of 10^5 is chosen to obtain a maximum current during the measurements of 0.212954 mA for the 0.9 mm beam diameter well above the digitization of 0.005194 mA. The error resulting from measuring outside of the dynamic range is accepted, because the high resolution of the cone scan is desired.

Measurements with lower resolution are carried out with a beam diameter of 1.7 mm and a attenuation of 10^6 resulting in the same maximum current of 0.212954 mA. For this beam diameter and attenuation the intensity lies within the dynamic range of the SiPM as indicated by the plateau in figure 5.20 (b). It is not completely understood why the plateau starting at an attenuation of 10^5 is clearly visible for the 1.7 mm beam diameter in figure 5.20 (b), while figure 5.20 (a) for the 0.9 mm beam diameter does not feature such a clear plateau. It is expected, that the plateau is already reached for weaker attenuations in case of the smaller beam diameter than in case of the larger beam diameter, since a smaller beam diameter at the same attenuation induces a smaller current in the SiPM. Possibly the inhomogeneity of the laser beam affects the measurements, as the intensity is largest in the center of the beam, which is used for the smaller beam diameter.

Besides this effect of the variation of the laser beam intensity, the dynamic range is reached for the larger beam diameter with the same maximum current as in case of the smaller beam diameter, because the intensity is spread over a larger area and thus a larger amount of G-APD cells. Because the intensity ratio equals about 0.6 for both 0.9 mm and 1.7 mm beam at the chosen attenuations, the measurements with the 0.9 mm beam can be investigated under reservation. Another cross-check with a photodiode is given in section 5.6. The beam diameters are estimated by the analysis of pictures of the beam penetrating graph paper resulting in 0.9 ± 0.1 mm and 1.7 ± 0.2 mm, respectively.

5.5.2 Analysis of Different Cone Models

Final Hex-to-Square cone without coupling

At first the dental laboratory model of the final Hex-to-Square cone is investigated with a 0.9 mm laser beam diameter and without the silicone gel coupling, thus with and air gap between exit window and SiPM coating. The top row in figure 5.21 plots the SiPM current in blue and the efficiency from the simulation in section 5.4.4 in red for sliding the laser across the entrance window of the cone on the left and rotating the cone on the right. The bottom row shows the corresponding temperature and SiPM bias voltage history. The diameter of the exit window equals the green shaded region, where the beam hits the SiPM without being reflected at the Winston shaped sides beforehand, while the region, where the beam still hits the entrance window, is red shaded.

On the top left of figure 5.21 the slope of the plateau in the green region, thus the direct perpendicular illumination of the SiPM, is potentially caused by the SiPM, which is true for all following plots including the slope of the plateau in the $\pm 10^\circ$ region of the cone rotation plots. This has been investigated by scanning only the SiPM and covering the whole aluminum mount with black tape to minimize the parasitic effect of reflections. In this case the plateau, which is expected to be flat when scanning the SiPM, features the same slope. Thus the slope seems to be intrinsic to the SiPM. Reasons might be an inhomogeneity of the silicon wafer across the SiPM or the influence of the signal path within the SiPM, which both affect the gain of the G-APD cells across the SiPM. Moreover reflections inside of the light-tight laser box might have an influence.

Apart from that, the simulation is reproduced by the measurement on the top left of figure 5.21, as the efficiency, i.e. the current in the SiPM, drops as soon as the beam does not hit the exit window directly. The reasons for this and the other features in the simulation are discussed in section 5.4.4. Also the recovery of the efficiency for larger distances to the cone center and the corresponding double peak structure fits the simulation, though misalignments of cone and laser or the imperfections of the exit window of the cone affect the height of the rightmost peak.

The cone rotation on the right of figure 5.21 features a broad bump on the left, which is an artifact of reflections on the green SiPM PCB and an imperfect shielding of the second SiPM behind the aluminum block shown in the picture on the top right in figure 5.18. In the following measurements, the whole SiPM PCB and the second SiPM are covered with black tape. Apart from this feature, the measurement also

reproduces the simulation of the cone rotation, though the small peak on the right at about 35° cone rotation angle is larger than the simulated one and the small variations in the simulation cannot be resolved by the current measurement with the SiPM. The heights of the peaks relative to each other are probably affected by the issues with the dynamic range of the SiPM discussed before for the small beam diameter as well as local temperature variations over the SiPM, which are not included in the error bars of the measurement plots. Though the temperature compensating tracking of the SiPM bias voltage follows the temperature history shown on the bottom of figure 5.21, the temperature sensor is located at a distance to the SiPM, as visible in the top right picture in figure 5.18. Therefore the temperature of the silicon layer of the SiPM is most probably larger than measured. The slope in the baseline of the temperature and SiPM bias voltage plots originates from the installation of the cone, since the aluminum block, housing cone, SiPM and temperature sensor, has to be touched to align the exit window of the cone on the SiPM resulting in a heating of the aluminum block, which cools down during the measurement. Nevertheless the measured temperature variations are, with less than 0.5°C , small during the whole measurement procedure and dominated by the heating of the SiPM by the current induced by the laser beam.

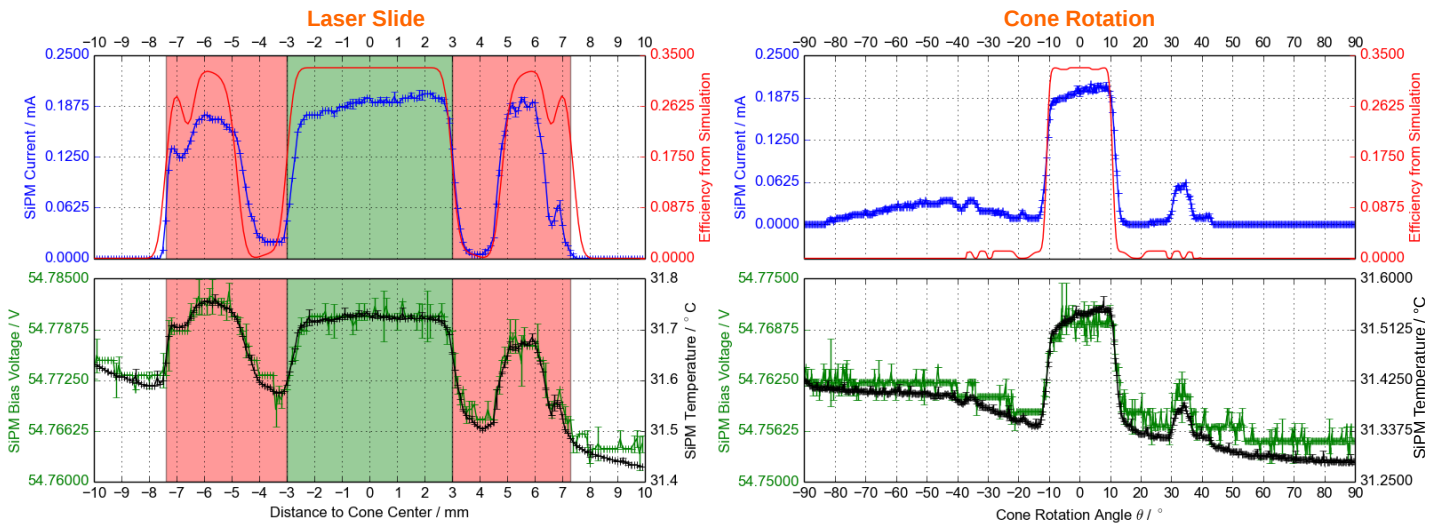


Figure 5.21: Dental laboratory Final Hex-to-Square cone without optical coupling. The top row plots the SiPM current in blue and the efficiency from the simulation in section 5.4.4 in red for sliding the laser across the entrance window of the cone on the left and rotating the cone on the right. The bottom row shows the corresponding temperature and SiPM bias voltage history. The measurement is carried out with a 0.9 mm laser beam diameter.

Comparison of different final Hex-to-Square cone models

A comparison of the performance of dental laboratory and Erlangen cone model is given in figure 5.22. Both cones are illuminated by the 0.9 mm laser beam and their exit windows are coupled to the SiPM via silicone gel. The laser slide plot shows, that the dental laboratory cone loses less intensity in the red shaded regions, where the side-walls of the cone reflect the beam before the SiPM is reached. A prob-

able reason is the polish of the Erlangen cone, which leads to rounded edges and a bellied exit window such that the Winston shape of the cone is distorted. Since the dental laboratory cone features a rougher polished shape closer to the initial Winston shape, this cone is closer to the simulation, in which the efficiency of light that is reflected at the side surfaces recovers to the plateau of central perpendicular illumination. The fluctuations in the red shaded region of the dental laboratory cone might be caused by the grooves on the cone surfaces.

The dip at the transition from direct to indirect SiPM illumination at ± 3 mm distance to the cone center on the left of figure 5.22 is studied for both cones, as it is larger than simulated. The size of the dip is identified to be correlated to overspilling silicone gel at the sides of the exit window as shown in figure 5.19 (b). The dip gets smaller when less silicone gel is deployed.

Because the exit window of the Erlangen cone is bellied, the amount of silicone gel cannot be optimized as far as in case of the dental laboratory cone. The overspilling silicone gel affects the performance of the Winston curves at the exit window sides. Therefore the amplitude of the fluctuations at larger distances to the cone center is larger for the Erlangen cone. The same argument holds for explaining the cone rotation measurements on the right of figure 5.22. The peaks at cone rotation angles beyond the acceptance angle of 37.2° of the Winston curve defining the illuminated surfaces originate from reflections of the golden pins of the SiPM shown in the top right picture of figure 5.18.

The SiPM current without installing the respective cone equals 0.212954 mA for central perpendicular illumination of the SiPM in case of both cones. Nevertheless the central plateau of the dental laboratory cone is located at only about 0.18 mA. The plateau of the Erlangen cone does not feature this absorption within the digitization uncertainty of $0.005194/\sqrt{12}$ mA. This absorption in the PMMA of the dental laboratory cone is also observed in section 5.6 and is visible as yellowness of the respective cone in figure 5.19 (a).

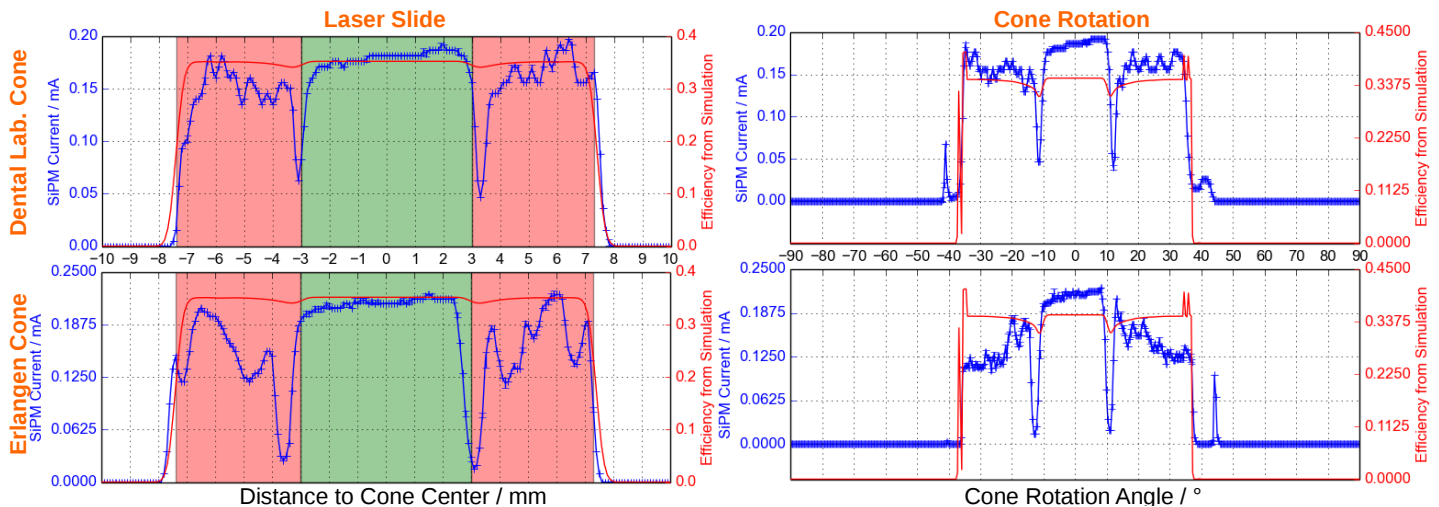


Figure 5.22: Comparison of dental laboratory and Erlangen cone model. The exit window of the respective cone is coupled to the SiPM via silicone gel. The dental laboratory cone model is on the top and the Erlangen cone model is on the bottom.

To investigate the effect of the dynamic range of the SiPM in case of the small laser beam diameter, the measurement of the goldsmith cone model is carried out with both 0.9 mm and 1.7 mm beam diameter. The results are shown in figure 5.23, where the cone is coupled with silicone gel again. As already estimated from looking at the different cone models by eye, comparing the bottom row of figure 5.22 with the top row of figure 5.23 yields that the properties of the goldsmith cone including absorption, surface roughness and polish are comparable to the Erlangen cone previously investigated. A systematic difference between the measurement with the 0.9 mm beam diameter on the top and 1.7 mm beam diameter on the bottom of figure 5.23 cannot be identified except for the expected sliding average behaviour of the larger beam diameter. Therewith the measurements with the smaller beam diameter seem to lie at the edge of the dynamic range of the SiPM, which is cross-checked with a photodiode in section 5.6.

The simulation of the cone rotation yields a recovery of the efficiency of the central plateau above $\pm 15^\circ$ cone rotation angle, which is not achieved in the measurements. This systematic difference might originate from the overspilling silicone gel as well as the surface roughness of the investigated cone models. The effect of surface roughness is expected to reduce the efficiency globally within the whole red shaded area in the laser slide measurements, as in this region the laser beam is reflected at a cone side surface. Nevertheless it is observed that the SiPM current recovers to the value of the central plateau for large distances to the cone center. Therefore it is probable that the effect of surface roughness is smaller than the effect of the coupling as well as the influence of polishing the Winston surfaces too much.

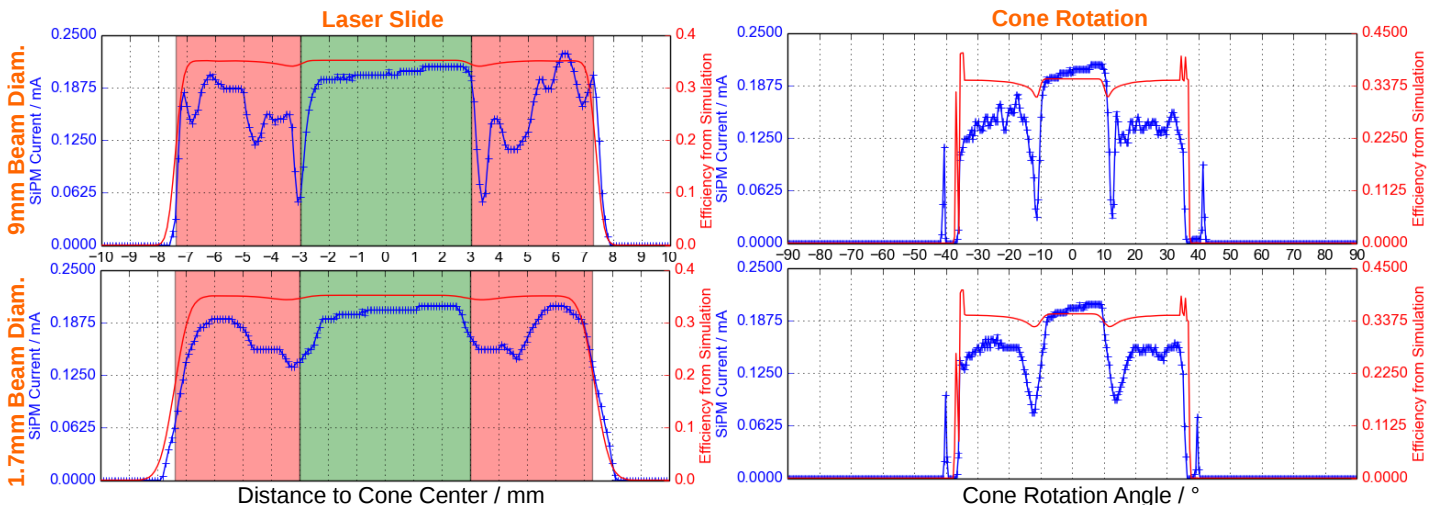


Figure 5.23: Comparison of different laser beam diameters with goldsmith cone model. Silicone gel couples the goldsmith cone to the SiPM.

Measurements of the former Circular Al cone

As shown in figure 5.24, also the former Circular Al cone reveals a worse performance than expected from the simulation when the laser beam does not hit the SiPM directly. Nonetheless the general shape of the efficiency curves obtained from the simulation can be reproduced. However the measurement with the smaller 0.9 mm

beam diameter features fluctuations in the red shaded regions of figure 5.24, while the 1.7 mm beam diameter measurement results in a smoothed shape. This deviation from the simulation can be reasoned by variations in the reflectivity or the surface roughness of the cone surface.

In the cone rotation measurement the sharp spikes just before reaching the acceptance angle of the cone at cone rotation angles of $\pm 26.6^\circ$ originate from the golden pins of the SiPM.

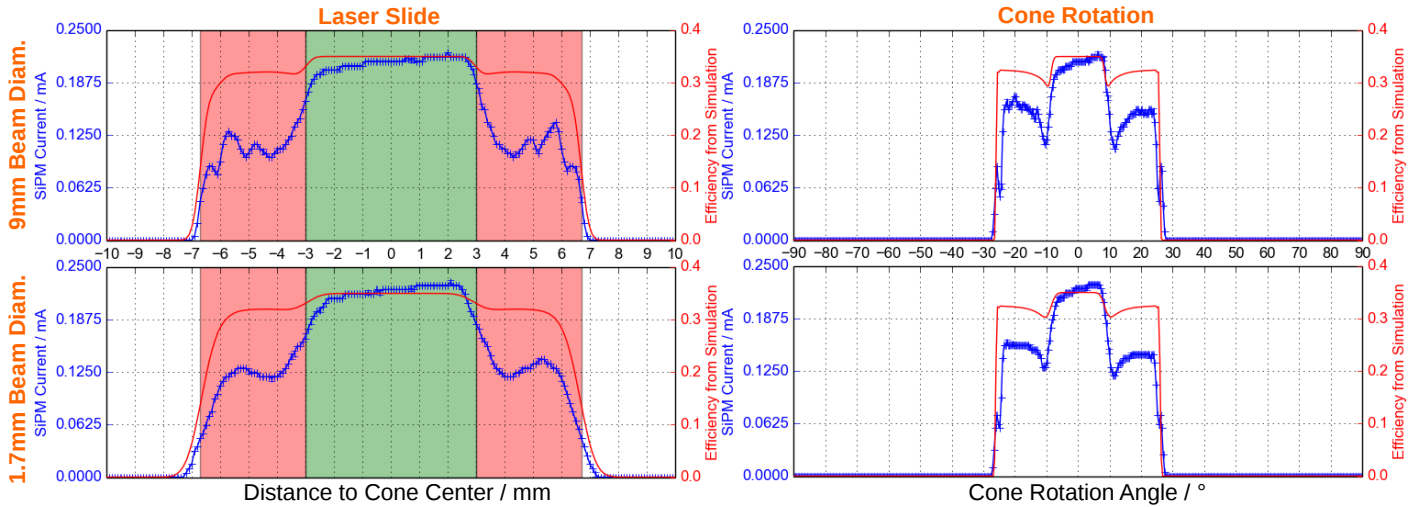


Figure 5.24: Measurement results of former Circular Al cone. Again both beam diameters of 0.9 mm on the top and 1.7 mm on the bottom are used to scan the cone.

Summarizing comparison with simulations

Though the simulation overestimates the performance of the surfaces of both final Hex-to-Square and former Circular Al cone, the cutoff observables of the simulation are reproduced. In case of the laser slide measurements the SiPM current drops exactly when the edge of the entrance window is reached. Whereas in the cone rotation measurements the SiPM current does not cut off completely until the acceptance angle of the illuminated surface is reached. Therefore the results of the simulations, which simulate the in-system performance of the cone within the IceAct telescope, have to be treated with caution.

To quantize the deviation of measurement and simulation in case of the larger laser beam diameter, the integrals over the SiPM currents and detection efficiencies, respectively, are calculated for the goldsmith cone model on the bottom of figure 5.23 and for the former Circular Al cone on the bottom of figure 5.24. The integrals are normalized to the value of central perpendicular illumination of the entrance window and the ratio of measurement to simulation integral is calculated. For the laser slide this results in a ratio of 91.6% for the final Hex-to-Square cone and 80.1% for the former Circular Al cone. Therewith the performance of the final Hex-to-Square cone is closer to the simulation. For the cone rotation both cones yield a comparable ratio of 78.0% and 80.1%, respectively.

The performance of the final Hex-to-Square cone can be improved by finding the correct amount of coupling fluid and a compromise between polishing the roughness of the cone surfaces and retaining the shape of the Winston surfaces, especially

at the exit window sides, while the optimization of the former Circular Al cone is almost exhausted. Therefore and since the performance of the former Circular Al cone is at least as much overestimated as the one of the final Hex-to-Square cone, the simulations allow for the inference, that the final Hex-to-Square cone significantly improves the performance of the light collection in the camera of the IceAct telescope.

5.6 Measurement of PMMA Absorption

As already observed in the previous sections, different PMMA compounds absorb light differently. Figure 5.25 gives an overview over the absorption of the investigated PMMA compounds. On the top left there is the yellowish absorbing PMMA, which the previously studied dental laboratory cone is made of, DD Bio Splint P HI [87]. On the top right another PMMA is shown, which is provided by the dental laboratory featuring only a few scattering impurities, Zirlux [88]. Moreover on the bottom there are two PMMA compounds stated to be UV-transparent. First, on the left the Evonik GS 0Z18 PMMA [89], which features only little scattering, and second the PMMA used for the production of the Erlangen cone, which only features visible scattering at the entrance surface, Evonik XT 0A070 GT [75]. The impurity of the DD Bio Splint P HI PMMA from the dental laboratory is stated to be an exceptional production or storage fault that has been fixed [47].

In order to investigate the absorption quantitatively, measurements have been performed with the laser of the setup and the Hamamatsu SiPM of the previous section. Therefore the laser beam is aligned such that the SiPM is hit perpendicularly into its center. Two measurements are performed, once with the PMMA within the beam path and once only with air within the beam path. Here and in the following the PMMA is not optically coupled to the light detector, such that the maximum expected transmittance equals 92%, as 4% of the light is lost due to reflections at each PMMA surface as shown in figure 5.7. The mean value of the measurement with PMMA is divided by the measurement with air and the statistical uncertainty on this ratio is calculated via Gaussian error propagation of the uncertainties on the mean of each measurement. The wavelength of the laser is given by $\lambda = 532.0(1.0)\text{nm}$ [77]. The measurement has been performed with the small 0.9 mm laser beam diameter and the large one of 1.7 mm to cross-check, whether the measurements of the

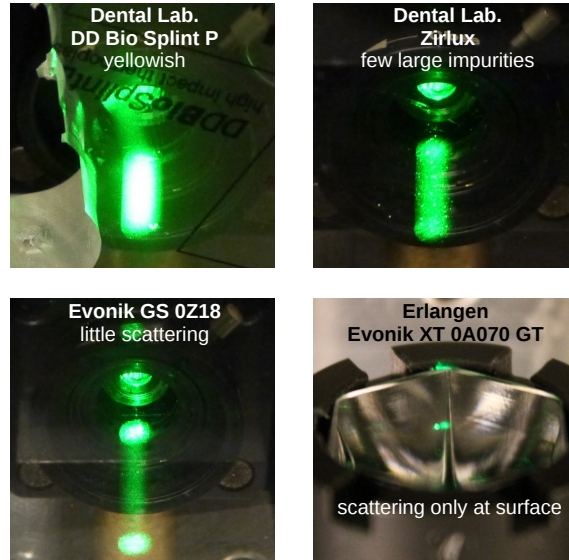


Figure 5.25: Absorption of visible light in different PMMA compounds. The pictures are taken with the same ISO values and exposure times except for the picture on the bottom right.

previous section are carried out within the dynamic range of the SiPM.

The same measurement is performed with a Hamamatsu S2281 photodiode [90], since photodiodes are meant to measure larger photon fluxes than SiPMs at the cost of single photon detection. The photodiode is connected to a pre-amplifier and controlled and read out by an Arduino Nano [91]. The low-gain channel of the pre-amplifier is read out providing an amplification of 10^9 . More informations on the pre-amplifier and the photodiode are given in [92] and [93].

The photodiode is also used to measure the absorption with LEDs of 405.0(5.0) nm [94] and 365.0(5.0) nm wavelength [95], thus in the UV-range covered by the spectral response of the SensL C-Series SiPM. The LEDs are collimated by a pin hole of 11 mm length and 2.5 mm diameter, which is not suited for measurements across distances in the range of centimetres due to the remaining beam divergence. Since the thicknesses of the investigated PMMA compounds given in table 5.7 range from 2 cm to 4 cm, the measurements only provide a trend of the absorption in PMMA, because the refraction in PMMA focusses the LED light counteracting the divergence, such that more light is focussed on the photodiode than in case of the air measurement. To counteract the effect of divergence and refraction, the reference measurement in air is carried out with the same distance between photodiode and LED as in case of the PMMA measurement. The transmittance is obtained through dividing the PMMA measurement by the air measurement. To account for the divergence, a systematic uncertainty on the transmittance is estimated to equal 0.15, where also the uncertainties of multiple reflections and surface roughness are included.

In case of the laser measurements with the larger beam diameter of 1.7 mm, the systematic uncertainty due to multiple reflections and surface roughness is estimated to equal 0.05 for both photodiode and the SiPM. Because the measurement of the small laser beam of 0.9 mm diameter with the SiPM is possibly not contained in the dynamic range of the SiPM, a larger systematic uncertainty of 0.1 is estimated. The resulting transmittances are listed in table 5.7 with their respective statistical and systematic uncertainty.

PMMA compound	DD Bio Splint P HI	Zirlux	Evonik GS 0Z18	Evonik XT 0A070 GT
Thickness	2 cm	2.5 cm	4 cm	2.35 cm
532 nm SiPM (0.9 mm)	0.86(01)(10)			0.95(00)(10)
532 nm SiPM (1.7 mm)	0.793(07)(50)			0.927(04)(50)
532 nm Photodiode	0.812(07)(50)			0.936(04)(50)
405 nm Photodiode	0.78(01)(15)	0.81(01)(15)	1.04(03)(15)	
365 nm Photodiode	0.37(03)(15)	0.36(00)(15)	1.10(00)(15)	

Table 5.7: PMMA transmittance measurement. The transmittance of the respective PMMA with given thickness is listed with statistical and systematic uncertainty. The values of the Evonik GS 0Z18 PMMA are larger than one, because of an unsuited collimation. The left column lists the deployed light sources and detectors. The 532 nm source is the laser used before [77], while the 405 nm and 365 nm sources are LEDs (see [94] and [95], respectively). Informations on the PMMA compounds are given in [87], [88], [89] and [75], respectively, going from left to right.

The difference in the transmittance between small and large beam diameter in case of the measurement with the SiPM originates from exceeding the dynamic range of the SiPM in case of the small beam diameter, since the measurement with the large beam diameter is compatible with the corresponding photodiode measurement. As already observed in the previous section, the PMMA DD Bio Splint P HI, which the dental laboratory cone model is made of, absorbs light in the visible range. The Evonik XT 0A070 GT PMMA, which is used for the Erlangen cone model, only features a light loss of 8%, which can be explained by reflection losses.

In the UV-region, which is of major importance in IceAct, the DD Bio Splint P HI and Zirlux PMMA feature the same drop in the transmittance, while the transmittance of the Evonik GS 0Z18 PMMA is compatible with 1 in the range of the measurement uncertainties. This emphasizes the statement of the manufacturer that the Evonik GS 0Z18 PMMA is UV-transparent [89].

A 3 mm thin DD Bio Splint P HI plate is stated to have a transmittance of 0.92 at 400 nm wavelength dropping steeply via 0.5 at 380 nm to 0 at 350 nm [47]. The transmittance at 380 nm of about 0.5 for 3 mm thickness translates to $0.5^{\frac{20}{3}} \approx 1\%$ for the 20 mm thick plate measured here, such that the statement is not compatible with the measurement, though the uncertainties of the measurement carried out here are large. Despite this ambiguity, both measurements show that the DD Bio Splint P HI and Zirlux PMMA compounds are not UV-transparent and should not be used for IceAct, especially if SensL J-Series SiPMs are installed, which provide a higher UV-transmittance than SensL C-Series SiPMs.

The transmittance of a 2.35 cm thick Evonik XT 0A070 GT PMMA block has been measured in Erlangen running from a transmittance of 0.92, corresponding to reflection losses, at 400 nm wavelength to 0.8 at 350 nm and then dropping steeply reaching 0 at 300 nm wavelength [65]. Therefore both Evonik PMMA compounds feature a UV-transmittance matching the SiPMs.

The PMMA of the Erlangen cone preserves a transmittance of 0.8 at 350 nm, thus about 8% reflection losses and 12% absorption. This is used to estimate the reduction of the in-system efficiency of the final Hex-to-Square cone in the simulation of section 5.4.1, where light rays of 380 nm wavelength are simulated. Absorption in PMMA, surface roughness and coupling issues are estimated to reduce the detection efficiency of the simulation relatively by 20%. This reduction can be included in the simulation by multiplying the resulting detection efficiencies of the tables 5.2 and 5.4 on the pages 61 and 62, respectively, with 0.8. Therewith the detection efficiency of the final Hex-to-Square cone coupled to a SensL C-Series SiPM in the central cone position, which is given in table 5.2, equals $\varepsilon_\gamma = 27.30\%$, while the corresponding detection efficiency accounting for the fill factor equals $a_\gamma = 26.58\%$. The relative reduction of the simulated detection efficiency of the former Circular Al cone is estimated to equal only 10%, since this cone features less issues with the coupling and absorption compared to the final Hex-to-Square cone. Therewith the detection efficiency accounting for the fill factor of the final Hex-to-Square cone is still a factor of about 1.6 larger than the one of the former Circular Al cone, which is a significant improvement.

5.7 Low Temperature Test of Cone-Coupling Glue

As discussed in section 5.5.2, the coupling of the exit window of the final Hex-to-Square cone to the SiPM is crucial for the performance in light detection. The coupling has to endure extreme environmental conditions at the South Pole. Therefore it is tested, whether the two-component epoxy glue EPO-TEK 310M-2 [96] withstands low temperature cycles. The glue is rated to be deployable continuously down to -55°C and matches the PMMA with a refractive index of 1.49 at 589 nm wavelength as well as the requirement of UV-transparency with $> 98\%$ spectral transmission down to 380 nm wavelength [96].

Acrylic blocks are glued on an acrylic plate as shown in figure 5.26. After hardening the glue for 20 hours at about 40°C the glued acrylic is put into a refrigerator at a temperature of $-42.0(5.0)^{\circ}\text{C}$ for 42 days. During this time the glued acrylic is extracted from the refrigerator 15 times and directly exposed to the skin temperature of a curious scientist, thus about $30.0(5.0)^{\circ}\text{C}$. Each time the glued acrylic is put into the refrigerator again after a few minutes. Despite of these temperature cycles, no changes at the glued surfaces are visible to the eye.

Therefore the glued acrylic is put into liquid nitrogen, thus into an environment of temperatures well below the deepest temperatures measured at South Pole. When exposing the glued acrylic to the extreme temperature drop between room temperature and liquid nitrogen promptly, the acrylic breaks and the glue fails. Nevertheless, when placing the glued acrylic just above the surface of the liquid nitrogen for a minute and pushing it under the surface afterwards, the acrylic does not break and the glued surfaces keep intact and transparent as shown in figure 5.26.

This extreme test of the temperature fluctuation resistivity indicates, that glueing a PMMA cone to an SiPM is possible even for the deployment at South Pole. Hence this glue is the default for the coupling of the final Hex-to-Square cones to the SensL C-Series SiPMs in the IceAct prototype, which will be brought to South Pole by the end of this year.

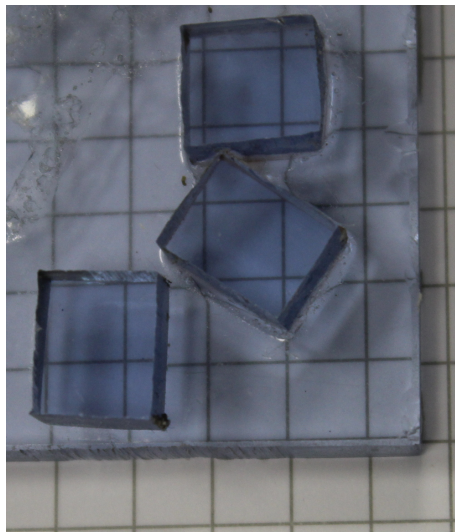


Figure 5.26: Glued acrylic after being exposed to liquid nitrogen.

6. Summary and Outlook

The IceAct telescope is designed to measure Cherenkov radiation generated in air showers in coincidence with the IceCube Neutrino Observatory. The objective of IceAct is vetoing air shower induced atmospheric muon and neutrino events penetrating IceCube and thus providing a larger sample of astrophysical neutrino events. Moreover IceAct can detect the cosmic ray flux in the knee region. Therefore IceAct can provide an additional independent measurement of the cosmic ray flux, which is also detected by IceTop and the IceCube Array. The new 61-pixel camera enables us to image air showers and allows for a composition measurement of cosmic rays in the energy regime of the knee. In the veto application especially the energy threshold of about 50 TeV is an advantage of IceAct over the IceTop surface detector with an energy threshold of about 300 TeV.

In the first part of this thesis a first night sky measurement with the 61-pixel IceAct prototype is described. The analysis of the events discovered several candidates that are likely to be produced by Cherenkov flashes from extensive air showers. In the future further analyses will need to be carried out and field tests experience with the new camera has to be gained.

The chief objective of this thesis was the development of light-collecting cones for the 61-pixel camera. Simulations and measurements proved the developed final Hex-to-Square cone to perform significantly better than the former Circular Al cone. The detection efficiency of the final Hex-to-Square cone is about 1.6 times larger compared to the former Circular Al cone, if the respective cone is coupled to a SensL C-Series SiPM, as stated in section 5.6. This is a significant improvement and a satisfying result.

Currently the new 61-pixel camera with final Hex-to-Square cones and SensL C-Series SiPMs is in production. After the assembly measurements with the fully equipped telescope can be performed to determine the response of each pixel. Afterwards the new IceAct prototype will be brought to the South Pole.

7. Appendix

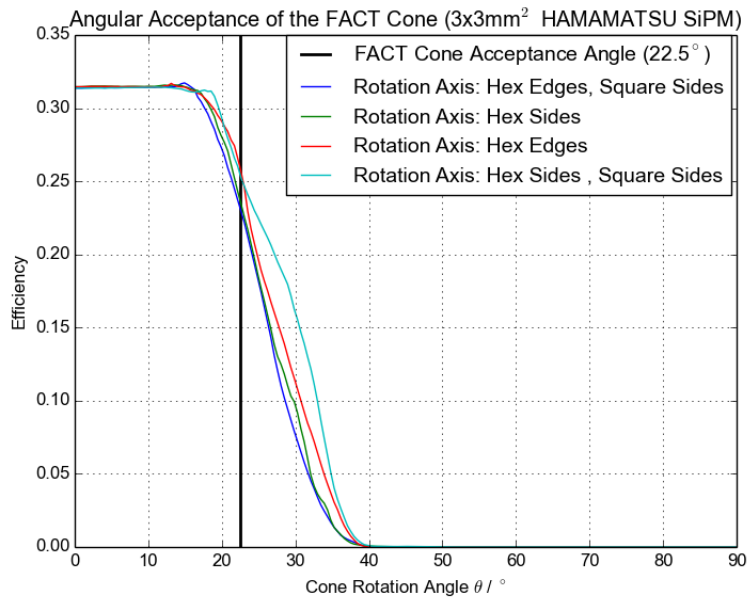


Figure 7.1: Angular acceptance of FACT cone. Simulation of section 5.4.3.

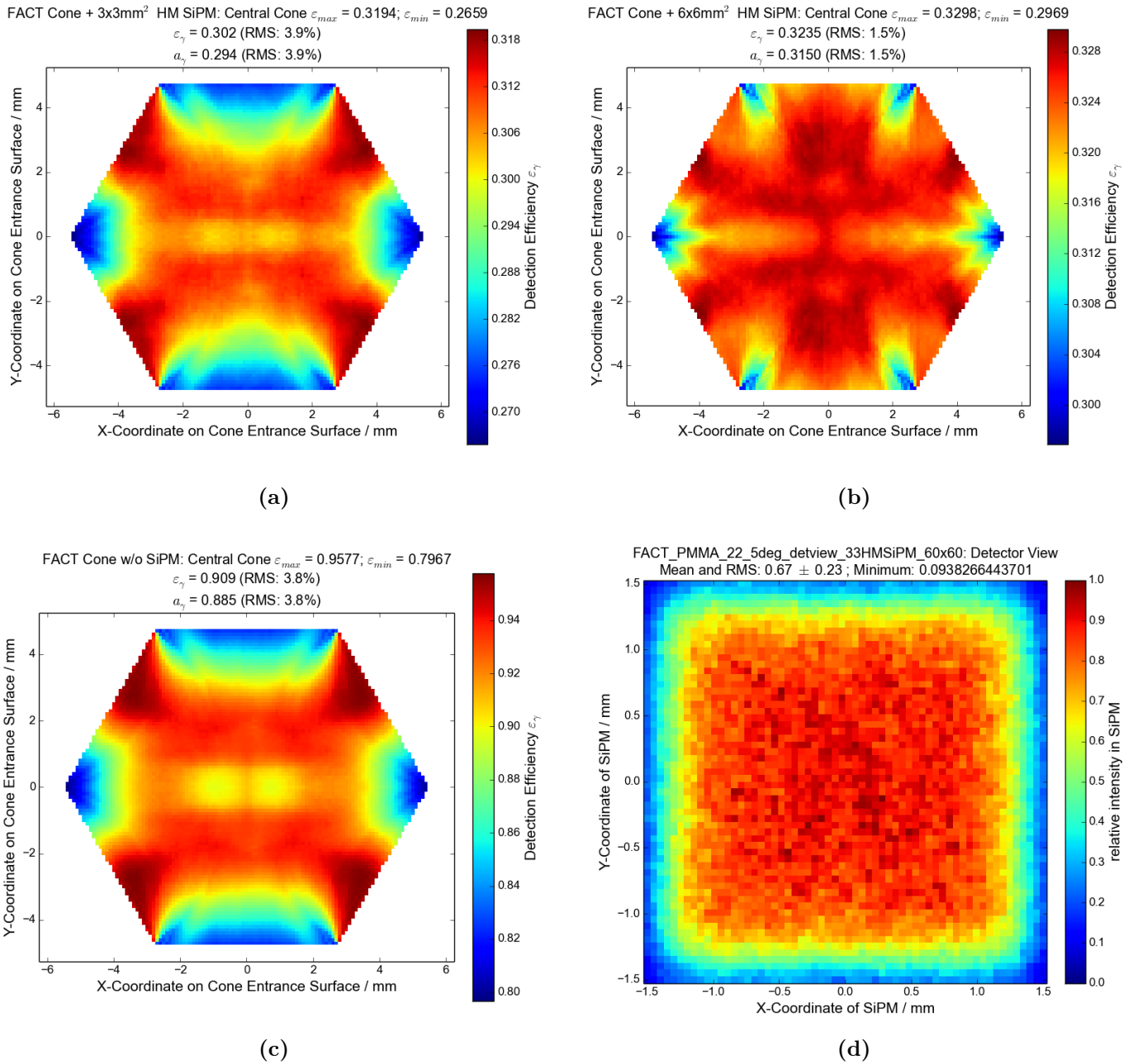


Figure 7.2: 2D Plots of simulated cone efficiencies and SiPM Illumination for FACT Cone. (a) - (c): Simulation of section 5.4.1 with 22.5° half apex angle of light cone. (a) Cone with 3x3² Hamamatsu S13360 SiPM. (b) Cone with 6x6² Hamamatsu S13360 SiPM. (c) Only cone. (d) SiPM illumination simulation of section 5.4.2 with 3x3² Hamamatsu S13360 SiPM and 60x60 detector cells and maximum incidence angle of 22.5°.

List of Figures

2.1	Differential energy spectrum of cosmic rays.	4
2.2	Sketched view of cosmological particle propagation.	6
2.3	Differential energy spectrum of neutrinos on Earth.	7
2.4	Sketches of IceCube and a Digital Optical Module.	8
2.5	Sketches of IceCube Gen2.	10
3.1	Cherenkov light cone.	13
3.2	First air Cherenkov telescope and principle of IACTs.	16
3.3	IceAct demonstrator at South Pole.	17
3.4	IceAct telescope design.	19
3.5	Comparison of former and new light-collecting cone.	20
3.6	Design of the camera.	21
3.7	p-n junction and G-APD cell structure of an SiPM.	23
3.8	Equivalent circuit diagram and typical waveforms of SiPMs.	25
4.1	Functional block diagram of the TARGET 7 ASIC.	30
4.2	Trigger circuit of the TARGET 7 ASIC.	31
4.3	The TARGET 7 module.	32
4.4	Setup in Erlangen.	34
4.5	Pixel layout of the camera.	35
4.6	Threshold values of trigger groups.	36
4.7	Waveforms of air shower candidate event 1633.	37
4.8	Camera view of event 1633.	37
4.9	Waveforms of brightest air shower candidate event 2102.	38
4.10	Camera view of brightest event 2102.	38
4.11	Histogram of summed up event signal height.	39
4.12	Waveforms of event 1779 with baseline step.	40

5.1	Camera layout yielding requirements on light-collecting cones.	42
5.2	2D view of Winston cone.	44
5.3	Compilation of investigated cones.	45
5.4	Layout of Hex-to-Square cones and sketch of parabola optimization. .	48
5.5	Development of Winston curves for final Hex-to-Square cone.	50
5.6	Comparison of the Hex-to-Square cone curves.	51
5.7	Reflectivity at optical transitions between cone and SiPM.	53
5.8	Simulation of the Cone Efficiency within the Telescope.	54
5.9	Wavelength dependence of PDE of SiPMs.	56
5.10	Simulated detection efficiencies for final Hex-to-Square and Circular PMMA cone with SensL C-Series SiPM.	58
5.11	2D Plots of simulated cone efficiencies for former Circular Al cone. . .	59
5.12	Simulated SiPM illumination for investigated cones.	64
5.13	Screenshot of the simulation of the angular efficiency.	65
5.14	Plot of angular efficiency of cones obtained from simulation.	66
5.15	Ray tracing of Circular PMMA cone.	67
5.16	Simulation for measurement comparison and multiple reflections in SiPM.	68
5.17	Resulting efficiency plots of the simulation of the measurement. . . .	69
5.18	Setup of cone measurement for verification of simulation and manu- facturing optimization.	71
5.19	Final Hex-to-Square cones from different manufacturers and coupling issues.	73
5.20	Dynamic range of SiPM considering different beam diameters.	74
5.21	Dental laboratory final Hex-to-Square cone without optical coupling.	76
5.22	Comparison of dental laboratory and Erlangen cone model.	77
5.23	Comparison of different laser beam diameters with goldsmith cone model.	78
5.24	Measurement results of former Circular Al cone.	79
5.25	Absorption of visible light in different PMMA compounds.	80
5.26	Glued acrylic after being exposed to liquid nitrogen.	83
7.1	Angular acceptance of FACT cone.	87
7.2	2D Plots of simulated cone efficiencies and SiPM Illumination for FACT Cone.	88

List of Tables

3.1	Characteristics of the SiPMs used for IceAct.	26
4.1	Characteristics of consecutive TARGET versions.	31
5.1	Characteristics of investigated cones.	46
5.2	Results of detection efficiency simulation of investigated cones.	61
5.3	Results of detection efficiency simulation with imperfect surfaces.	62
5.4	Results of detection efficiency simulation for SensL J-Series SiPM.	62
5.5	Results of detection efficiency simulation of cones only.	62
5.6	Characteristics of the SiPM used in the setup	72
5.7	PMMA transmittance measurement.	81

Bibliography

- [1] V. F. HESS, *Über Beobachtungen der durchdringenden Strahlung bei sieben Freiballonfahrten*, Physik. Zeitschr., 13 (1912), pp. 1084–1091. <http://www.mpi-hd.mpg.de/hfm/HESS/public/HessArticle.pdf>, accessed: 04.08.2017, 11:23.
- [2] C. PATRIGNANI *et al.*, *Review of Particle Physics*, Chin. Phys., C40 (2016), p. 100001.
- [3] J. BLÜMER, R. ENGEL, AND J. R. HÖRANDEL, *Cosmic rays from the knee to the highest energies*, Progress in Particle and Nuclear Physics, 63 (2009), pp. 293–338.
- [4] M. RAO AND B. SREEKANTAN, *Extensive Air Showers*, World Scientific Publishing Co. Pte. Ltd., 1998. ISBN 981-02-2888-0.
- [5] T. K. GAISSER, T. STANEV, AND S. TILAV, *Cosmic ray energy spectrum from measurements of air showers*, Frontiers of Physics, 8 (2013), pp. 748–758.
- [6] F. HALZEN AND D. HOOPER, *High-energy neutrino astronomy: the cosmic ray connection*, Reports on Progress in Physics, 65 (2002), pp. 1025–1078.
- [7] W. PAULI, *Open letter*. <http://microboone-docdb.fnal.gov/cgi-bin/RetrieveFile?docid=953;filename=pauli%20letter1930.pdf;version=1>, accessed: 29.07.2017, 16:35, 1930.
- [8] F. REINES AND C. L. COWAN, *Detection of the free neutrino*, Phys. Rev., 92 (1953), pp. 830–831.
- [9] C. L. COWAN *et al.*, *Detection of the free neutrino: a confirmation*, Science, 124 (1956), pp. 103–104.
- [10] M. G. AARTSEN *et al.*, *Evidence for high-energy extraterrestrial neutrinos at the IceCube detector*, Science, 342 (2013), p. 1242856.
- [11] C. SPIERING, *Towards high-energy neutrino astronomy*, The European Physical Journal H, 37 (2012), pp. 515–565.
- [12] J. YANG. https://gallery.icecube.wisc.edu/internal/v/graphics/physicus.pdf.html?g2_imageViewsIndex=1, password protected, accessed: 27.07.2017, 15:30.
- [13] F. HALZEN, *High-energy neutrino astrophysics*, Nature Physics, 13 (2016), pp. 232–238.

-
- [14] M. G. AARTSEN *et al.*, *The IceCube Neutrino Observatory: Instrumentation and Online Systems*, JINST, 12 (2017), p. P03012.
- [15] M. AARTSEN, R. ABBASI, Y. ABDU, AND M. ACKERMANN, *Measurement of south pole ice transparency with the IceCube LED calibration system*, Nuclear Instruments and Methods in Physics Research A, 711 (2013), pp. 73–89.
- [16] J. YANG. https://gallery.icecube.wisc.edu/internal/v/graphics/arraygraphics2011/ArrayWSeasonsLabels.jpg.html?g2_imageViewsIndex=1, password protected, accessed: 27.07.2017, 15:28.
- [17] ICECUBE COLLABORATION. <https://icecube.wisc.edu/gallery/view/140>, password protected, accessed: 27.07.2017, 15:35.
- [18] F. HALZEN AND S. R. KLEIN, *Invited review article: IceCube: An instrument for neutrino astronomy*, Review of Scientific Instruments, 81 (2010), p. 081101.
- [19] R. ABBASI, Y. ABDU, M. ACKERMANN, AND J. ADAMS, *IceTop: The surface component of IceCube*, Nuclear Instruments and Methods in Physics Research A, 700 (2013), pp. 188–220.
- [20] J. YANG. https://gallery.icecube.wisc.edu/internal/v/IceCubeGen2/IceCube_Gen2_Facility/gen2_layout_042115.jpg.html?g2_imageViewsIndex=1, password protected, accessed: 27.07.2017, 15:33.
- [21] S. FLOYD. https://gallery.icecube.wisc.edu/internal/v/IceCubeGen2/IceCube_Gen2_Facility/gen2_structure_101816.jpg.html?g2_imageViewsIndex=1, password protected, accessed: 27.07.2017, 15:34.
- [22] W. GALBRAITH AND J. V. JELLEY, *Light pulses from the night sky associated with cosmic rays*, Nature, 171 (1953), pp. 349–350.
- [23] T. BRETZ *et al.*, *FAMOUS - A fluorescence telescope using SiPMs*, in 34th International Cosmic Ray Conference (ICRC2015), July 2015, p. 649.
- [24] J. SCHUMACHER *et al.*, *Dedicated power supply system for silicon photomultipliers*, in 34th International Cosmic Ray Conference (ICRC2015), July 2015.
- [25] M. SCHAUFEL *et al.*, *Small size air-Cherenkov telescopes for ground detection arrays - a possible future extension?*, in 35th International Cosmic Ray Conference (ICRC2017), July 2017.
- [26] T. NIGGEMANN, *The silicon photomultiplier telescope FAMOUS for the detection of fluorescence light*, PhD Thesis, III. Phys. Inst. A, RWTH Aachen University, Okt. 2016.
- [27] J. AUFFENBERG *et al.*, *Design study of an air-Cherenkov telescope for harsh environments with efficient air-shower detection at 100 TeV.*, in 34th International Cosmic Ray Conference (ICRC2015), July 2015.

-
- [28] J. AUFFENBERG *et al.*, *On improving composition measurements by combining compact Cherenkov telescopes with ground based detectors*, in 35th International Cosmic Ray Conference (ICRC2017), July 2017.
- [29] THE ICECUBE-GEN2 COLLABORATION, *IceAct: Imaging Air Cherenkov Telescopes with SiPMs at the South Pole for IceCube-Gen2*, in 35th International Cosmic Ray Conference (ICRC2017), July 2017.
- [30] C. PATRIGNANI *et al.*, *Review of Particle Physics*, Chin. Phys., C40 (2016), p. 100001.
- [31] P. A. ČERENKOV, *Visible radiation produced by electrons moving in a medium with velocities exceeding that of light*, Physical Review, 52 (1937), pp. 378–379.
- [32] I. FRANK AND I. TAMM, *Coherent Visible Radiation of Fast Electrons Passing Through Matter*, Springer Berlin Heidelberg, Berlin, Heidelberg, 1991, pp. 29–35.
- [33] THE LHCb COLLABORATION, *LHCb detector performance*, International Journal of Modern Physics A, 30 (2015), p. 1530022.
- [34] J. HOLDER, *Atmospheric Cherenkov Gamma-ray Telescopes*, (2015).
- [35] J. G. LEARNED AND K. MANNHEIM, *High-energy neutrino astrophysics*, Annual Review of Nuclear and Particle Science, 50 (2000), pp. 679–749.
- [36] R. CHAVES, *Highlights from H.E.S.S.*, 2017.
- [37] J. RICO, *Overview of MAGIC results*, Nuclear and Particle Physics Proceedings, 273-275 (2016), pp. 328–333.
- [38] J. HOLDER, *Latest results from VERITAS: Gamma 2016*, 2017.
- [39] J. HINTON AND W. HOFMANN, *Teraelectronvolt astronomy*, Annual Review of Astronomy and Astrophysics, 47 (2009), pp. 523–565.
- [40] G. HALLEWELL. <http://timeline.web.cern.ch/timelines/Cosmic-rays?page=1>, accessed: 17.08.2017, 18:55.
- [41] D. NEISE, J. ADAM, AND M. AHNEN, *FACT – status and experience from five years of operation of the first g-APD cherenkov telescope*, Nuclear Instruments and Methods in Physics Research A, (2017).
- [42] W. HOFMANN, *The cherenkov telescope array – status*, 2017.
- [43] S. FUNK *et al.*, *Target: A digitizing and trigger ASIC for the cherenkov telescope array*, AIP Conference Proceedings, 1792 (2017), p. 080012.
- [44] L. HALVE, *Analysis of the first Data from the SiPM-Camera of the Air Cherenkov Telescope IceAct at the South Pole*, Bachelor’s Thesis, III. Phys. Inst. B, RWTH Aachen University, Apr. 2016.

- [45] M. GÜNDER, *Analyse der Zeitsynchronisation des IceACT-Luft-Čerenkov-Teleskop Prototypen mit dem IceCube Neutrino Observatorium anhand erster Felddaten*, Bachelor's Thesis, III. Phys. Inst. B, RWTH Aachen University, Aug. 2016.
- [46] T. SÄLZER, *Analysis of coincident air showers with IceCube, IceTop and IceAct during the Austral winter 2016*, Master's Thesis, III. Phys. Inst. B, RWTH Aachen University, Sept. 2017.
- [47] *Private communication with J. Auffenberg, III. Physikalisches Institut der RWTH Aachen, 2016-2017.*
- [48] M. SCHAUFEL, *HAWC's Eye – Implementing Hybrid Detection by combining a compact air-Cherenkov telescope with the HAWC Gamma-Ray Observatory*, Master's Thesis, III. Phys. Inst. A, RWTH Aachen University, Sept. 2017.
- [49] SCHOTT TECHNICAL GLASS SOLUTIONS GMBH, *SCHOTT BOROFLOAT[®] 33*. http://psec.uchicago.edu/glass/borofloat_33_e.pdf, accessed: 21.08.2017, 18:30.
- [50] ORAFOL FRESNEL OPTICS GMBH, *Positive Fresnel Lenses*, 2013. <http://www.orafol.com/energy/europe/en/positive-fresnel-lenses>, accessed: 21.08.2017, 12:50.
- [51] S. H. SIMON, *The Oxford Solid State Basics*, Oxford University Press, 2013. ISBN 978-0-19-968077-1.
- [52] J. P. KOSCHINSKY, *Signal extraction from SiPM traces taken by prototype electronics developed for AugerPrime*, Bachelor's Thesis, III. Phys. Inst. A, RWTH Aachen University, Sept. 2015.
- [53] D. RENKER AND E. LORENZ, *Advances in solid state photon detectors*, Journal of Instrumentation, 4 (2009).
- [54] T. BRETZ *et al.*, *Dynamic range measurement and calibration of SiPMs*, Journal of Instrumentation, 11 (2016), p. P03009.
- [55] HAMAMATSU PHOTONICS, *MPPC Array S12573 Series Product Array*, Oct. 2013.
- [56] SENSL TECHNOLOGIES LTD., *C-Series Low Noise, Blue-Sensitive Silicon Photomultipliers DATASHEET Rev. 2.6*, Dec. 2016.
- [57] —, *J-Series High PDE and Timing Resolution, TSV Package DATASHEET Rev. 2.5*, Nov. 2016.
- [58] E. GANSTER, *Test des TARGET-7-Datenerfassungsmoduls für das IceACT Luft-Cherenkov-Teleskop*, Bachelor's Thesis, III. Phys. Inst. B, RWTH Aachen University, Aug. 2016.

- [59] B. J. PESTKA, *Commissioning of the self-trigger of the TARGET read-out-board for FAMOUS*, Bachelor's Thesis, III. Phys. Inst. A, RWTH Aachen University, Sept. 2016.
- [60] N. L. HÖFLICH, *Implementation and calibration of the TARGET data acquisition system for FAMOUS*, Bachelor's Thesis, III. Phys. Inst. A, RWTH Aachen University, Sept. 2016.
- [61] G. DO, *Testmessungen zur Temperaturstabilität des TARGET-7 Datenerfassungsmoduls für das IceAct Luftschauber Teleskop*, Bachelor's Thesis, III. Phys. Inst. B, RWTH Aachen University, Sep. 2017.
- [62] A. ALBERT *et al.*, *Target 5: A new multi-channel digitizer with triggering capabilities for gamma-ray atmospheric cherenkov telescopes*, *Astroparticle Physics*, 92 (2017), pp. 49 – 61.
- [63] L. TIBALDO *et al.*, *TARGET: toward a solution for the readout electronics of the Cherenkov Telescope Array*, *PoS, ICRC2015* (2016), p. 932. [34,932(2015)].
- [64] B. STAHL, *Trigger Studies of TARGET-7: A Proposed Front End Electronics Solution for the Cherenkov Telescope Array*. http://www.benjamin-stahl.com/stahl_report_final.pdf, accessed: 26.07.17, 15:00, Aug. 2014.
- [65] *Private communication with A. Zink, Erlangen Centre for Astroparticle Physics, 2016-2017.*
- [66] THURLBY THANDAR INSTRUMENTS LTD., *New PL & New PL-P Series*, 2013. <http://resources.aimtti.com/datasheets/psu-npl-series-8p.pdf>, accessed: 08.09.2017, 11:00.
- [67] H. ANDERHUB *et al.*, *Design and operation of FACT – the first g-APD cherenkov telescope*, *Journal of Instrumentation*, 8 (2013), p. P06008.
- [68] R. WINSTON *et al.*, *Nonimaging Optics*, Elsevier Academic Press, 2005. ISBN 978-0-12-759751-5.
- [69] AUTODESK INC., *Autodesk Inventor*. <https://www.autodesk.com/products/inventor/overview>, accessed: 08.09.2017, 12:50.
- [70] B. HUBER *et al.*, *Solid light concentrators for small-sized photosensors used in Cherenkov telescopes*, in *32nd International Cosmic Ray Conference (ICRC2011)*, 2011.
- [71] ZEMAX LLC, *Zemax OpticStudio*. <http://www.zemax.com/os/opticstudio>, accessed: 08.09.2017, 12:45.
- [72] W. DEMTRÖDER, *Experimentalphysik 2*, Springer Berlin Heidelberg, 2013.
- [73] M. N. POLYANSKIY, *Refractive index database*. <https://refractiveindex.info/?shelf=main&book=A1&page=Rakic>, accessed: 24.09.2017, 12:00.

- [74] HAMAMATSU PHOTONICS, *S13360 series MPPCs for precision measurement*, Aug. 2016.
- [75] EVONIK INDUSTRIES AG, *PLEXIGLAS[®] GS/XT Rohre und Stäbe*, 2012. <https://www.plexiglas-shop.com/pdfs/de/211-12-PLEXIGLAS-Rohre-Stäbe-de.pdf>, accessed: 15.09.2017, 22:15.
- [76] J. AUDEHM, *Simulation und Test von Winston Cones für das abbildende Luft-Tscherenkow-Teleskop IceACT*, Bachelor's Thesis, III. Phys. Inst. B, RWTH Aachen University, Aug. 2016.
- [77] THORLABS INC., *Compact Laser Diode Module CPS532 22442-S01, Rev B*, 2015.
- [78] —, *SM1D12 Lever-Actuated Iris Diaphragm*. <https://www.thorlabs.com/thorproduct.cfm?partnumber=SM1D12>, accessed: 08.09.2017, 16:35.
- [79] —, *25 mm Mounted Absorptive ND Filters, AR-Coated: 350 - 700 nm*. https://www.thorlabs.com/newgrouppage9.cfm?objectgroup_id=6272, accessed: 08.09.2017, 16:40.
- [80] —, *Mounted 25 mm Absorptive Neutral Density Filters*. https://www.thorlabs.com/NewGroupPage9.cfm?ObjectGroup_ID=266, accessed: 08.09.2017, 16:35.
- [81] ADAFRUIT INDUSTRIES LLC, *Datasheet stepper motor NEMA-17*. <https://cdn-shop.adafruit.com/product-files/324/C140-A+datasheet.jpg>, accessed: 08.09.2017, 16:30.
- [82] —, *Adafruit Motor Shield V2 for Arduino*, 2017. <https://cdn-learn.adafruit.com/downloads/pdf/adafruit-motor-shield-v2-for-arduino.pdf>, accessed: 08.09.2017, 16:30.
- [83] ARDUINO LLC, *Arduino Uno Rev3*. <https://store.arduino.cc/arduino-uno-rev3>, accessed: 08.09.2017, 13:00.
- [84] HAMAMATSU PHOTONICS, *Power supply for MPPC C11204-02 Operatoin Manual Rev. B*, 2016.
- [85] —, *Power supply for MPPC C11204-02*, 2017.
- [86] —, *Power supply module for MPPC C11204-02 Command Reference Rev. C*, 2016.
- [87] DENTAL DIREKT GMBH, *Product catalog CAD/CAM Materials*. <http://www.dentaldirekt.com/index.php/service/download-center/finish/13-catalogs/874-materials-catalog-2017.html>, accessed: 15.09.2017, 22:15.
- [88] HENRY SCHEIN INC., *Zirlux[®]*. <https://www.plexiglas-shop.com/pdfs/en/211-1-PLEXIGLAS-GS-XT-en.pdf>, accessed: 15.09.2017, 22:15.

-
- [89] EVONIK INDUSTRIES AG, *PLEXIGLAS[®] GS/XT*, 2011. <https://www.plexiglas-shop.com/pdfs/en/211-1-PLEXIGLAS-GS-XT-en.pdf>, accessed: 15.09.2017, 22:15.
- [90] HAMAMATSU PHOTONICS, *Si photodiodes S2281 series*, 2015.
- [91] ARDUINO LLC, *Arduino Nano*. <https://store.arduino.cc/arduino-nano>, accessed: 08.09.2017, 16:00.
- [92] D. TOSI AND C. WENDT, *Calibrating the photon detection efficiency in IceCube*, ArXiv e-prints, (2015).
- [93] R. HEILMANN, *Charakterisierung der Linearität und Stabilität eines Photodiodensystems zur Kalibrierung von IceCube-Gen2 Photosensoren*, Bachelor's Thesis, III. Phys. Inst. B, RWTH Aachen University, Jul. 2016.
- [94] ETG INC., *ETG-5UV405-30 Data sheet*.
- [95] ROITHNER LASERTECHNIK GMBH, *LED365-06Z rev. 1.0*, 2016. http://www.roithner-laser.com/datasheets/led_div/uv/led365-06z.pdf, accessed: 08.09.2017, 11:50.
- [96] EPOXY TECHNOLOGY INC., *Produce Information Sheet EPO-TEK[®] 310M-2*. http://www.epotek.com/site/administrator/components/com_products/assets/files/Style_Uploads/310M-2.pdf, accessed: 18.09.2017, 10:00.

8. Acknowledgements

Danksagungen

Zuerst gebührt mein Dank Herrn Prof. Dr. Wiebusch, der es mir ermöglichte, meine Masterarbeit in seiner Arbeitsgruppe zu verfassen. Ebenso gilt mein Dank Herrn Prof. Dr. Bretz, der sich gerne dazu bereit erklärte, die Zweitkorrektur meiner Masterarbeit zu übernehmen. Beiden danke ich zudem für ihre Unterstützung sowie dafür, dass sie sich stets Zeit für die Beantwortung meiner Fragen nahmen und mir mit konstruktiver Kritik weiterhalfen.

Bedanken möchte ich mich auch bei den Aachener IceCube, IceAct und FAMOUS Arbeitsgruppen, die mich herzlich aufnahmen und deren zahlreiche Meetings meine wissenschaftliche Arbeitsweise bereicherten.

Herzlichst danke ich meinem Betreuer, Dr. Jan Auffenberg, der mir selbst außerhalb der üblichen Arbeitszeiten stets mit schnellen und kompetenten Antworten half. Zudem unterstützte er mich jederzeit mit Anregungen und seiner motivierenden Art. Für die Unterstützung meiner Messaufbauten sowie die Beantwortung zahlloser Fragen danke ich insbesondere Julian Kemp, Martin Rongen und Johannes Schumacher. Herrn Jahn danke ich stellvertretend für die Mechanik-Werkstatt des III. Physikalischen Instituts B, RWTH Aachen, für die konstruktive Beratung sowie die schnelle und präzise Fertigung von Bauteilen. Des Weiteren danke ich den Sekretärinnen Ruth Jansen und Claudia Cüster-Weiger für die gemeinsame humorvolle Erarbeitung bürokratischer Angelegenheiten. Für den Wissensaustausch, der am Anfang meiner Masterarbeitszeit sehr wichtig war, danke ich den ehemaligen IceAct und FAMOUS Bacheloranden Nina Höflich, Jan Audehm, Erik Ganster und Benjamin Pestka. Besonderer Dank gilt Lisa Schumacher, Dr. Jan Auffenberg und Martin Rongen für das Korrekturlesen meiner Arbeit.

Stellvertretend für die CTA Arbeitsgruppe des Erlangen Centre for Astroparticle Physics unter der Leitung von Prof. Dr. Stefan Funk danke ich Dr. Adrian Zink für die Zusammenarbeit im Bereich der TARGET 7 DAQ sowie für die Bereitstellung eines Prototypen des final Hex-to-Square Lichtkonzentrators.

Ich danke Fabian, Martin und Tim für 5 erfüllte Physikstudiumsjahre.

Elly, danke ich herzlichst dafür, dass wir gemeinsam durchs Leben reisen und sie mich stets motiviert noch einen Gang höher zu schalten.

Mit den letzten Worten dieser Arbeit danke ich meinen Eltern von ganzem Herzen für ihre tatkräftige Unterstützung, die ich schätze wie keine Zweite, und ihren unermüdlichen Zuspruch, der mich durch alle Herausforderungen leitet.

Erklärung

Hiermit versichere ich, dass ich diese Arbeit einschließlich beigefügter Zeichnungen, Darstellungen und Tabellen selbstständig angefertigt und keine anderen als die angegebenen Hilfsmittel und Quellen verwendet habe. Alle Stellen, die dem Wortlaut oder dem Sinn nach anderen Werken entnommen sind, habe ich in jedem einzelnen Fall unter genauer Angabe der Quelle deutlich als Entlehnung kenntlich gemacht.

Aachen, den 27. September 2017

Jan Paul Bernd Koschinsky